Ultrafast Chemical Dynamics of Catalysts and Photoswitches

by

Lindsay Brooke Michocki

A dissertation submitted in partial fulfillment
of the requirements for the degree of
Doctor of Philosophy
(Chemistry)
in the University of Michigan
2020

Doctoral Committee:

Professor Kevin Kubarych, Chair
Professor Eitan Geva
Professor Ayyalusamy Ramamoorthy
Professor Roseanne Sension

Lindsay B. Michocki
michocki@umich.edu
ORCID iD: 0000-0002-0154-9906

Dedication

To Mom, Dad, and Taylor

Acknowledgements

I'm going to start, true to form, by quoting a musical. The line "look at where you are, look at where you started" from the musical Hamilton was something that I came back to again and again throughout my time in graduate school, as a reminder to always be cognizant of how much I had grown and learned throughout this crazy, frustrating, and rewarding experience. I know without a doubt that I would not have gone from where I started to where I am now without the support of everyone mentioned here, and many others not mentioned.

First, I would like to thank my research advisor **Kevin Kubarych.** Since I joined the group, Kevin has been unbelievably supportive and helpful throughout every laser/electronic malfunction, LabView bug, career path crisis, attack of imposter syndrome, and experimental success. Kevin allowed and encouraged me to do such a wide variety of work throughout my Ph D, from jumping into spectroelectrochemistry to travelling the world doing data analysis for XFEL experiments. I would finally like to thank Kevin for being the only other person I knew in graduate school that cared as much about musical theatre as I did. I would like to thank **Eitan Geva** and **Ayyalusamy Ramamoorthy** for all of their helpful insight and guidance throughout the years. **Roseanne Sension** has been such an invaluable part of my Ph D – serving not only as a committee member but as a role model for what a driven and successful woman in spectroscopy can be. I would also especially like to thank Roseanne for including me on all of the X-ray projects (and the rest of team X-ray, including **Jim Penner-Hahn, Aniruddha Deb,** and **Nick Miller**), as these experiences were truly one of the highlights of my PhD, even when we were on hour 21 of our 24 hour SLAC shift. A huge thank you to all Kubarych lab members that I overlapped with (**Aaron White, Laura Kiefer, Peter Eckert, Kim Daley, Ved Roy, Joe Meadows, Rong**

Duan, Joseph Mastron, and **Vivian Crum**) for all of their support and sometimes much needed distractions over the years. Laura and Kim were amazing mentors, and I learned so much from both of them. Joe has been a great confidant throughout all of grad school, and I am happy I got to work with such a good friend for part of this journey (and also that he is officiating my wedding). I would like to thank Vivian for our daily Spelling Bee ritual, which kept me sane during my last year of graduate school. I would also like to thank the members of the **Oglivie**, **Sension**, and **Sanford** groups who have provided me assistance over the years.

Thank you to my very supportive friends in Ann Arbor, who consistently made grad school a more fun place to be (**Allison Roessler**, **Michael Roessler**, **Ellen Mulvihill**, and **Audrey Tolbert**). A special thank you to the other two points in the "P Chem Trifecta", Allison and Ellen. I'm so grateful that the other two women in this cluster (for our cohort) happened to be such amazing people that have been both excellent academic peers and my closest friends. Another thank you to Audrey Tolbert, for all of the advice both scientific and non-scientific, and for supporting both my Dunkin and trash Netflix movie addictions. I would like to thank my supportive friends outside of Ann Arbor (especially **Arlin Delgado**) for all of their encouragement, visits, and friendship throughout my Ph D. Thank you to my wonderful parents, for supporting me and encouraging me to pursue this degree. Thank you to my little sister **Taylor Michocki**, for all that she does to inspire and motivate me to keep going after my goals, and for being the best travel partner/T Swift concert date in the world. Lastly, I would like to thank my fiancé, **Mark Mantell**. I could have published a million first author papers in the highest impact and most prestigious journals and won every award and fellowship and none of it would have even come close to being the best thing to happen to me in my Ph D, because I met him.

Table of Contents

Dedication ii
Acknowledgements iii
Table of Contents v
List of Figures vii
List of Abbreviations xii
Abstract xiv
Chapter 1 Introduction 1
1.1 INTRODUCTION 1
1.2 APPLICATIONS OF $Re(bpy)(CO)_3Cl$ 2
1.2.1 $Re(N\text{-}N)(CO)_3Cl$ as a photo-trigger of electron transfer 2
1.2.2 $Re(bpy)(CO)_3Cl$ as an electrocatalyst 4
1.3 TWO-DIMENSIONAL INFRARED SPECTROSCOPY 5
1.3.1 Two-Dimensional Infrared Spectroscopy Methods 5
1.3.2 Spectral Diffusion 6
1.4 PHOTOCHEMICALLY ACTIVATED COBALAMINS 7
1.5 X-RAY ABSORPTION SPECTROSCOPY 9
1.6 THESIS OUTLINE 10
1.7 REFERENCES 12
Chapter 2 Synthesis and Vibrational Dynamics of a Small Molecule Model for a Rhenium Tricarbonyl Labelled Peptide System 19
2.1 INTRODUCTION 19
2.2 EXPERIMENTAL METHODS 23
2.2.1 Equilibrium 2DIR Spectroscopy 23
2.2.2 Sample Preparation 25
2.3 RESULTS 26
2.4 DISCUSSION 29
2.5 CONCLUSIONS 31

2.6 REFERENCES....31
Chapter 3 Ultrafast Two-Dimensional Infrared Spectroelectrochemical Measurements of Electrocatalyst Re(bpy)(CO)3Cl....35
3.1 INTRODUCTION....35
3.2 EXPERIMENTAL METHODS....39
3.2.1 Equilibrium 2DIR Spectroscopy....39
3.2.2 Sample Preparation....40
3.3 RESULTS....40
3.3.1 Linear FTIR Measurements....40
3.3.2 2DIR Measurements....43
3.4 CONCLUSIONS....46
3.5 REFERENCES....46
Chapter 4 X-ray Absorption Spectroscopy of Methylcobalamin....50
4.1 INTRODUCTION....50
4.2 EXPERIMENTAL METHODS....52
4.3 RESULTS AND DISCUSSION....53
4.3.1 Time-resolved Polarized XANES....53
4.3.2 Comparison with Computational Methods....61
4.4 CONCLUSIONS....67
4.5 REFERENCES....68
Chapter 5 Conclusions and Future Directions....71
5.1 FUTURE DIRECTIONS....72
5.2 REFERENCES....75

List of Figures

Figure 1.1 Structure of heptad LKWLEHK labelled with Re(bpy)(CO)3. 3
Figure 1.2. In 2DIR, three fields interact with the sample, followed by a signal emission. By controlling the second time delay, t2, the evolution and characteristic relaxation timescale of a molecule can be observed. 6
Figure 1.3 Schematic structure of MeCbl. In adenosyl cobalamin, the methyl upper axial group is replaced with a 5'-deoxyadenosyl group. 8
Figure 2.1 Cartoon representation of the mechanism for photoinduction of electron transfer via rhenium tricarbonyl label as proposed by Vlcek and Gray.[9] 20
Figure 2.2 Structures of parent $Re(bpy)(CO)_3Cl$ (ReCl) (left) and $[Re(bpy)(CO)_3(benzimidazole)]^+$ [ReBenzIm]+ (right). 23
Figure 2.3 A) FTIR Spectrum of [ReBenzIm]+ in THF, with peak assignment to vibrational modes for the metal carbonyl region of the spectrum. B) A'(1) mode of [ReBenzIm]+ in DMSO, THF, and CAN, showing the observed solvent-dependent peak shift. 26
Figure 2.4 Structure of heptad peptide with the sequence LKWLEHK labelled with $Re(bpy)(CO)_3$ through the histidine side chain. 27
Figure 2.5 FTIR Spectrum of heptad peptide labelled with Re(bpy)(CO)3 in D2O. 27
Figure 2.6 Absorptive 2DIR spectrum of the 2029 cm^{-1} peak of [ReBenzIm]+ in THF 28
Figure 2.7 Solvation dynamics of [ReBenzIm]+ probed in A) DMSO, B) THF, and C) acetonitrile. Spectral diffusion timescales are shown on the figure. 29
Figure 2.8 Comparison of the normalized FTIR spectra in THF for ReCl (black) and $[ReBenzIm]^+$. 30

Figure 3.1 Proposed mechanism of the ReCl electrocatalytic reduction cycle in THF, showing formation of the singly reduced rhenium species (2) and the Re-Re dimer (4). 41
Figure 3.2 Schematic of a top-down view of the OTTLE cell used in our measurements. 42
Figure 3.3 A) Full FTIR difference spectrum of ReCl in THF with 0.1 M TBAPF6 over a voltage range of -0.5 to -1.8 V. B) Zoomed in FTIR spectrum highlighting the high frequency modes of ReCl (2019 cm^{-1}), singly reduced ReCl (1996 cm^{-1}), and the Re-Re dimer (1986 cm^{-1}). 43
Figure 3.4 2DIR spectra of ReCl in THF and 0.1 M TBAPF6 taken without use of phase wobbler (left) and with the wobbler engaged (right) illustrating the reduction of scatter without major expense to the signal. 44
Figure 3.5 FFCF showing spectral diffusion timescale of ReCl with 0.1 M $TBAPF_6$ in THF. 44
Figure 3.6 Snapshot non-rephasing 2DIR spectra showing evolution of the singly reduced ReCl species (1996 cm^{-1}) and Re-Re dimer (1986 cm^{-1}) peaks, as the voltage was increased from 0 V (A) to -1.7 V (B). 45
Figure 4.1 Schematic structure of MeCbl indicating the directions assigned as x, y, and z. The numbering system for the ring nitrogens (inset) assumes that upper ligand is above the plane of the figure. The lower axial ligand is the nitrogen from dimethylbenzimidazole (N_{DMB}). The upper axial ligand is methyl. For AdoCbl, the methyl group is replaced by a 5'-deoxyadenosyl group, shown in the upper right. 52
Figure 4.2 (A) The XANES spectrum of AdoCbl obtained from the optical laser-off measurement is compared with the scaled difference spectra at 250 ps and 450 ps time delay following excitation at 540 nm. The cob(II)alamin XANES spectrum derived from the 450 ps difference spectrum is shown for comparison. (B) The XANES difference spectrum at 250 ps decomposed into contributions in the *x*, *y*, and *z* directions. 55

Figure 4.3 Left: Comparison of the isotropic XANES difference spectra obtained 250 ps after excitation of AdoCbl at 540 nm (blue) and 3 65 nm (yellow). The ground state XANES spectrum of AdoCbl is plotted in black for reference. Right: Decomposition of the XANES difference spectrum 450 ps after excitation of AdoCbl into x and y+z components. 56
Figure 4.4 (A) Isotropic difference spectrum (blue, ΔA) and absorption anisotropy (red, r) 40 ps after excitation of AdoCbl at 340 nm. This plot demonstrates that the transition dipole moments at 365 nm and 540 nm are approximately orthogonal to each other. (B) Time dependent anisotropy changes at four wavelengths following excitation at 340 nm. The change in anisotropy over the first 200 ps reflect changes in the excited state followed by formation of cob(II)alamin. The anisotropy is approximately constant from 200 ps to 450 ps demonstrating that diffusive reorientation of the cobalamin molecule is small on this time scale. This means that the 250 ps and the 450 ps XANES transient reflect the initial anisotropic distribution of excited states. 57
Figure 4.5 Comparison of the ground state XANES spectra of AdoCbl and MeCbl in a room temperature liquid jet using fs x-ray pulses. The MeCbl has been scaled to match the counts for AdoCbl as different detector arrangements were used for these two runs. Note that, in the absence of radiation damage, these two spectra are similar with only a slight blue-shift of the edge for MeCbl compared with AdoCbl. 58
Figure 4.6 Top: The total isotropic difference spectrum 100 ps after excitation of MeCbl and the decomposition into *x* and *y*+*z* contributions. The difference spectrum for formation of cob(II)alamin is also plotted, calculated as the difference between cob(II)alamin determined from the photolysis of AdoCbl and the ground state MeCbl spectrum. Bottom: Comparison of the laser off XANES spectrum for the ground state of MeCbl with the cob(II)alamin XANES and the

inferred excited state spectrum of MeCbl at 100 ps. The regions marked A, B, and C are discussed in the text. 59
Figure 4.7 Comparison of the XANES difference spectra for the formation of the excited state (ES, gray) and cob(II)alamin (Cob(II)) from the ground state (GS) of MeCbl (blue). The difference spectrum for the formation of cob(II)alamin is the same as the spectrum reported by Subramanian et al. for microsecond delay. The estimated spectrum for 25% cob(II)alamin and 75% excited state (orange) is also shown for comparison. 60
Figure 4.8 Left: Comparison of ground and excited state simulated spectra for MeCbl with the measured spectra. S_1 is the excited state structure identified in TD-DFT calculations. The axial bond lengths in S_0 are (Co-C, Co-N_{IM}) = (1.986 Å, 2.175 Å), in S_1 they are (2.006 Å, 2.055 Å). The Co-$N_{2(3)}$ bonds are expanded about 2% while the Co-$N_{1(4)}$ bonds are essentially unchanged. The decomposition of the simulated ground state spectrum into contributions polarized in the *x*, *y*, and *z* directions is also plotted. Top Right: Comparison of the measured (orange) and simulated (yellow) isotropic difference spectra and the *x*-polarized contributions (dark green experiment, light green simulation). Bottom Right: Comparison of the *y*+*z* component of the difference spectrum for simulation (pink) and experiment (red) along with the decomposition of the simulation into the *y* and *z*-polarized contributions. 62
Figure 4.9 Top Left: Comparison of the *x* and *y*+*z* measurements with simulations performed for a range of Co-C bond lengths. The solid lines are *y*+*z* simulations, the dashed lines are the *x* simulations. Bottom Left: Decomposition of the y+z simulation into the y (dashed lines) and z (solid lines) contributions. Top Right: Comparison of the *x* and *y*+*z* measurements with simulations performed for a range of Co-N_{IM} bond lengths. Bottom Right: Decomposition of the y+z simulation into the y (dashed lines) and z (solid lines) contributions.....63

Figure 4.10 . Expansion of the ring distances to Co in units of mÅ (i.e. in S_1 nitrogen N_3 is 0.042 Å further from the Co than it is in S_0). (A) Expansion from S_0 to S_1 using the simulated ground and excited states. (B) An additional expansion of the Co-N_{eq} distances as indicated. (C) Expansion of the entire ring midway between r hodibalamin and S_1 cobalamin 64
Figure 4.11 Comparison of experimental and simulated XANES difference spectra for an expanded corrin ring. The axial bond lengths are indicated as Co-C, Co-N_{IM}. (A) Co-N_{eq} bonds as in Figure 4.10 B midway between calculated MeCbl S_1 and the AdoRbl ring. The axial bonds are at the calculated S_1 distances. (B) Co-N_{eq} bonds as in Figure 4.10 B midway between calculated MeCbl S_1 and the AdoRbl ring. The axial bonds are at the calculated S_0 distances. (C) Co-N_{eq} bonds as in Figure 4.10 B midway between calculated MeCbl S_1 and the AdoRbl ring. The Co-C bond is at the calculated S_1 distance and the Co-N_{IM} bond is contracted to 2.125 Å from the ground state value of 2.175 Å. (D) Full corrin ring expansion as in Figure 4.10 C. The axial bonds are the same as in Figure 4.12 C. 65
Figure 4.12 Comparison of the influence of the corrin ring (labeled S1 ring, Rbl ring) and the N_{IM}-Co-C bond angle (labeled S0 ring) on the simulated XANES difference spectrum. The axial bonds are at the ground state distances. 66

List of Abbreviations

2D: two-dimensional

2DIR: two-dimensional infrared (spectroscopy)

ACN: acetonitrile

AdoCbl: adenosyl cobalamin

AgGaS: Silver Gallium Sulfide

BBO: beta-barium borate

CCD: charged coupled device

cm^{-1}: wavenumber

DFG: difference frequency generation

DFT: density functional theory

ET: electron transfer

EXAFS: extended X-ray absorption fine structure

FDMNES: finite difference method near-edge structure

FFCF: frequency-fluctuation correlation function

FT: Fourier transform

FTIR: Fourier Transform Infrared (Spectroscopy)

FWHM: full width half max

IR: infrared radiation

IVR: intramolecular vibrational redistribution

LCLS: linac coherent light source

LO: local oscillator

MD: molecular dynamics

MeCbl: methyl cobalamin

MLCT: metal to ligand charge transfer

nm: nanometer

OPA: optical parametric amplification

OTTLE: optically transparent thin-layer electrochemical (cell)

ReCl: $Re(bpy)(CO)_3Cl$

SEC: spectroelectrochemistry

SFG: sum-frequency generation

SLAC: Stanford Linear Accelerator Center

THF: tetrahydrofuran

Ti:sapph: Titanium:sapphire

UV-Vis: ultraviolet-visible

ω1: excitation axis

ω3: detection axis

XANES: X-ray absorption near-edge structure

XAS: X-ray absorption spectroscopy

XFEL: X-ray free electron laser

ZnSe: zinc selenide

Abstract

Catalytic or biological mechanisms can be impacted by a change to the catalytic system or its surroundings. To determine and optimize these mechanisms, these effects that occur on an ultrafast timescale must be identified. Experimental techniques that operate on a similar molecular timescale are necessary to capture the evolution of these species over time. We seek to understand how changes in the electronic structure of catalysts and photoswitches impact solvation and structural dynamics. Using ultrafast two-dimensional infrared (2D-IR) spectroscopy, we analyze how changes in the electron density of the Lehn CO_2 reduction catalyst $Re(bpy)(CO)_3Cl$ (ReCl) affect its vibrational dynamics by modifying the lower axial ligand from the chloride to a more electron-withdrawing benzimidazole ligand. We observe a significant blue shift in the carbonyl stretching frequencies, with the A'(1) stretching mode significantly more blue shifted than the A" stretching mode, behavior previously observed in the ^{3}MLCT excited state. We find little to no impact on the solvation dynamics, but a consistent trend in solvent dependence both of the spectral diffusion timescales and the frequencies of the stretching modes. This trend was previously observed for ReCl and its derivatives, and attributed to the donicity, a measure of nucleophilicity, of the solvent. This result further supports our finding that the carbonyl groups on this molecule are local probes of their solvation environment, with the solvation dynamics not depending on the electrostatics of the whole molecule.

Implementation of a novel 2D-IR spectroelectrochemical (2DIR-SEC) experimental design allows us to study the intermediates generated in the electrocatalytic reduction of $Re(bpy)(CO)_3Cl$ *in situ*, allowing us to record the impact of reduction of this molecule on the solvation dynamics. Here, we perform

for the first time an ultrafast 2D-IR SEC experiment using a spectroelectrochemical cell designed to be used in transmission mode. Using an optically transparent thin-layer electrochemical (OTTLE) cell, with apertures cut into the Pt mesh electrodes to allow our beams to pass through, we are able to measure spectroelectrochemical 2D-IR data on ReCl in THF, seeing clear signatures from two key species that result from the one-electron reduction of this molecule – a singly reduced anion and a Re-Re dimer. Further analysis to extract dynamical information from the 2DIR-SEC spectra is ongoing, however the success of this experimental geometry opens a plethora of possibilities for *in situ* monitoring of an electrochemically-driven process or reaction using 2D-IR.

Ultrafast transient polarized X-ray absorption measurements performed on methylcobalamin give a window into structural changes that occur following photoexcitation. We use 520 nm visible excitation to visibly excite methylcobalamin to its long-lived excited state. Complementing our experimental results with finite difference method near-edge structure (FDMNES) calculations leads us to find small spectral changes in the equatorial and axial directions, which we interpret as arising from small changes in the axial and corrin ring bond lengths. This confirms expectations drawn from prior UV-visible transient absorption measurements and theoretical simulations. Our results highlight the capability of polarized transient X-ray absorption for isolating structural dynamics in systems undergoing atomic displacements that are strongly correlated to the exciting optical polarization.

Our studies span a variety of ultrafast spectroscopic techniques to gain insight into key intermediate species in electrocatalytic or biological mechanisms. The work presented here, and the future work detailed at the end of the dissertation, demonstrates the ability of these techniques to reveal new windows into the ultrafast dynamic processes that govern these molecules and their mechanisms.

Chapter 1 Introduction

1.1 INTRODUCTION

Catalytic and biological systems drive the natural world, and exploration of these systems will allow us to optimize them to open up possibilities for scientific and technological advancements. A key component of understanding how these molecules function is the determination and analysis of intermediates that occur during the mechanisms that power important reactions throughout chemistry and biochemistry. However, these intermediates are often short-lived and difficult to identify, limiting our ability to resolve their roles in the overall mechanism.

The reactions and processes that generate these intermediates can occur on an ultrafast timescale, necessitating experimental techniques that operate on a similarly short timescale in order to gain insight into behavior of these molecules and their environment. Phenomena such as molecular reorientation or relaxation can take place on timescales as short as femtoseconds and capturing these fluctuations in the molecule and environment on the timescale that they occur is key to understanding how the system evolves over time. One common technique used to study these ultrafast processes is pump-probe spectroscopy, in which a very short pump laser pulse excites a molecule, followed by a probe laser pulse that reports on changes in the molecule following the excitation after a controlled amount of time. Varying the time delay between the pump and probe pulse gives a window into how the system is evolving after the initial photoexcitation as a function of time. Pump-probe spectroscopy has been implemented using a variety of spectroscopic methods, including UV-Vis, infrared, Raman, and x-ray spectroscopies, and has provided key insights into reaction timescales, identification of intermediates, and excited state structures.

The pumping process can be driven by two pump pulses that can be interferometrically scanned, yielding a two-dimensional frequency or wavelength correlation spectrum. This expansion of pump-probe spectroscopy to a second dimension is thus called two-dimensional spectroscopy and gives information on how the correlation between excitation and detection frequencies changes over time as a result of fluctuations of the molecule itself or its environment. Similarly to pump-probe, this technique can be implemented for multiple spectroscopic methods, including infrared, UV-Vis, and NMR spectroscopies. In this dissertation, I will focus on two different ultrafast spectroscopy techniques applied to two different chemical systems. First, I will discuss ultrafast two-dimensional infrared spectroscopy measurements on the photo- and electrocatalyst Re(bpy)$(CO)_3$Cl (ReCl), and next I will discuss ultrafast transient X-ray absorption measurements on methylcobalamin.

1.2 APPLICATIONS OF Re(bpy)$(CO)_3$Cl

Complexes in the *fac*-Re(I)(L)$(CO)_3$(N-N) family have a wide variety of applications throughout chemistry. They are highly modifiable synthetically, with both the diimine ligand and the axial L ligand able to be significantly varied. They possess unique spectroscopic, photophysical, and photo- and electrochemical properties, all of which have shown to be dependent on the nature of their lowest excited states, and thus by the structure of the molecule.[1–18] Modifications of these complexes allows them to be applied to a range of chemical systems, including photo- and electrocatalysis, protein labelling, biomolecular and cell imaging, and biological sensors.[12,13,16,19–32] Here, we will focus on two applications of this robust system of molecules – as photo-triggers of electron transfer in proteins and as electrocatalysts for CO_2 reduction.

1.2.1 Re(N-N)$(CO)_3$Cl as a photo-trigger of electron transfer

When attached to azurins via a histidine side chain, rhenium tricarbonyl diimine complexes can trigger electron transfer reactions in the protein upon electronic excitation to the first excited state.[16,33–39] The electron transfer proceeds through a “hopping” mechanism, aided by a charge separated state formed on a

neighboring tryptophan residue, eventually resulting in the oxidation of the copper metal center of the protein.[33–36,38,40] Utilization of the same method for attaching the rhenium motif but on a *de novo* designed metalloenzyme would allow for complete control over key degrees of freedom in this electron transfer mechanism, such as distances between the rhenium and the hopping-assistant tryptophan residue and differences in solvation environments. The Pecoraro group at the University of Michigan has developed a *de novo* coiled-coil metalloenzyme peptide system that contains a hydrophobic interior mimicking what would be seen in a full-sized protein, while remaining small enough for ease of labelling.[41–43] This peptide is comprised of a heptadic repeat LKALEEK, which can be easily edited to incorporate the necessary histidine and tryptophan residues for attachment of the rhenium and the electron transfer hopping mechanism, respectively. The structure of the heptad sequence modified to be labelled with the rhenium tricarbonyl moiety and contain the necessary tryptophan residue is given in **Figure 1.1**.

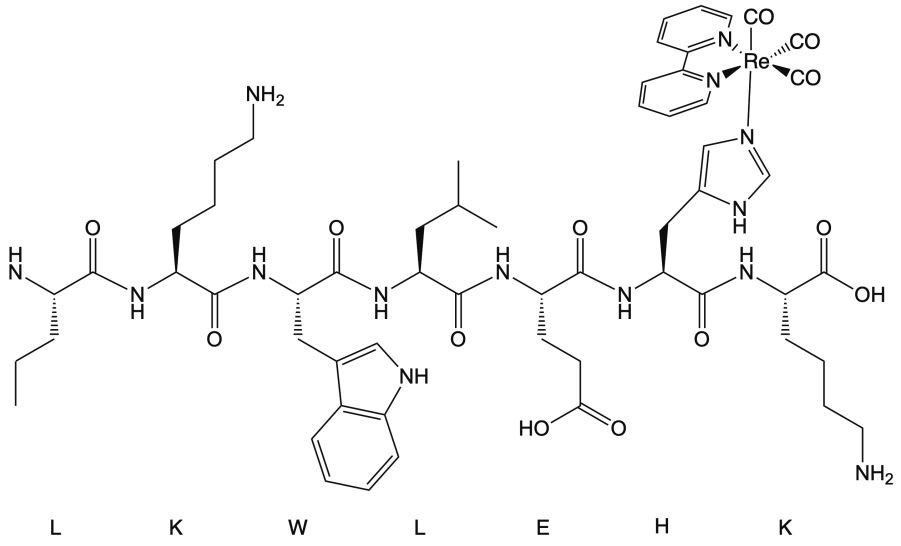

Figure 1.1 Structure of heptad LKWLEHK labelled with Re(bpy)(CO)3.

The previously described picture of this electron transfer mechanism has been obtained mostly from transient IR absorption studies of the phototrigger.[16,38,39,44] However, this system seems to be an ideal fit for two-dimensional infrared spectroscopy, as it contains multiple vibrational probes that will be sensitive to

changes in hydration or electronic structure of the system, including the rhenium moiety and the carbonyls in the peptide backbone. Introduction of isotope labels in the backbone carbonyls will allow for even greater site-specificity.[45–50] We have previously characterized the solvation dynamics of $Re(bpy)(CO)_3Cl$ in a range of solvents, as well across a series of complexes with modifications to the bipyridine ligand in order to test the effects of changes on electron density on the vibrational dynamics of this molecule. We found little to no effect of the equatorial ligand. However in the case of the peptide label the modification will be to the axial ligand, replacing a chloride ligand with the more electron-withdrawing histidine.[51] Thus, we determined the first step towards the goal of studying the labelled peptide system with 2DIR to be generation of small molecule models of the system that mimic the electron-withdrawing character of the axial histidine, to allow for future separation of changes in the vibrational dynamics that stem from the change in electron density from changes induced by the peptide system.

1.2.2 $Re(bpy)(CO)_3Cl$ as an electrocatalyst

Molecules of the type $Re(L)(N\text{-}N)(CO)_3$ are robust electrocatalysts for the reduction of CO_2 to CO.[52–54] In addition to traditional electrochemical experimental methods, this complex has been studied by a wide range of spectroelectrochemical techniques, which monitor the evolution of new species spectroscopically following the controlled application of a potential to induce oxidation or reduction. Spectroelectrochemical (SEC) measurements on this system have included UV-Vis-SEC, FTIR-SEC, and Raman-SEC measurements, with the goal of determining the intermediate species that occur during the electrocatalytic cycle and gaining greater insight into how changes to the structure of the electrocatalyst and conditions of the environment, such as solvent and availability of a proton source, affect both the pathway and efficiency of the electrocatalysis.[13,28,52,55–71] Ultrafast two-dimensional infrared spectroscopy, with its ability to separate out congested spectra that may be generated due to the presence of multiple intermediates and as well as its known sensitivity to the vibrational and solvation dynamics of $Re(bpy)(CO)_3Cl$ can be combined with electrochemical techniques in a manner similar to established

FTIR-SEC methods to provide an unprecedented window into the behavior of this electrocatalyst.[51,72,73]

1.3 TWO-DIMENSIONAL INFRARED SPECTROSCOPY

Metal carbonyl vibrations are located in an otherwise bare region of the vibrational spectrum, allowing for clear analysis and identification of bands without worry of congestion of the spectrum from other species present or different functional groups. As a result, metal carbonyl molecules are excellent vibrational probes. The most common implementation of vibrational spectroscopy is linear Fourier transform IR measurements (FTIR). FTIR measurements are useful for identification of functional groups, but lack utility for determining dynamical information unambiguously from an infrared spectrum. Two-dimensional infrared spectroscopy (2DIR) overcomes this limitation by incorporating correlated excitation and detection frequencies, revealing ultrafast time-dependent changes in a vibrational spectrum that can be attributed to dynamical processes such as chemical exchange and vibrational energy transfer.

1.3.1 Two-Dimensional Infrared Spectroscopy Methods

Our 2DIR experimental setup uses a regeneratively amplified titanium:sapphire laser to produce 100 fs pulses at a center wavelength of 800 nm with 1-5 mJ of energy per pulse at a 1 kHz repetition rate. The output is then split, with one output being used to generate a white light continuum from a YAG crystal, which then is mixed with the remaining 800 nm light on two independent β-barium borate (BBO) crystals to generate near IR pulses. The use of two separate BBO crystals allows us to independently tune the frequencies of our excitation and detection pulses. The output from each BBO is then used to generate two mid-IR pulses with a center frequency of ~2000 cm^{-1} with a 125 cm^{-1} FWHM bandwidth through difference frequency generation in two AgGaS crystals. The resulting pulses are then split into four IR pulses – three to be used as our excitation and detection pulses, and the fourth used as local oscillator to serve as a reference.[74]

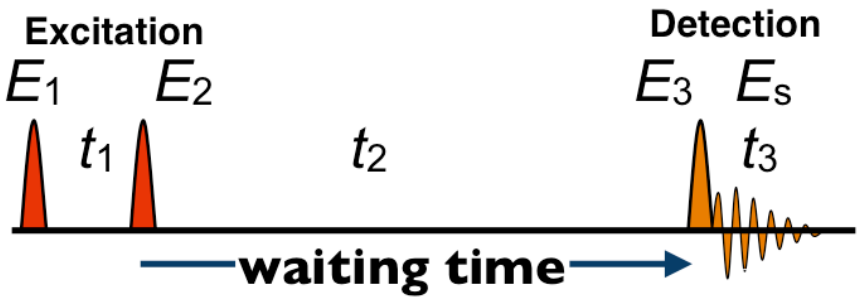

Figure 1.2. In 2DIR, three fields interact with the sample, followed by a signal emission. By controlling the second time delay, t2, the evolution and characteristic relaxation timescale of a molecule can be observed.

The three pulses are arranged in a background-free box-car geometry, and interact with our sample to give a third-order noncollinear signal. The three fields (E_1, E_2, and E_3) each has an associated wave vector denoted here as $\mathbf{k_1}$, $\mathbf{k_2}$, and $\mathbf{k_3}$. The fields are separated by two time delays, the coherence time (t_1) and the waiting time (t_2), which result in the signal emitted during t_3 (**Figure 1.2**). Our 2DIR experiment uses two different pulse sequences to obtain two phase-matched signals, both rephasing ($\mathbf{k_r} = -\mathbf{k_1} + \mathbf{k_2} + \mathbf{k_3}$) and non-rephasing ($\mathbf{k_n} = \mathbf{k_1} - \mathbf{k_2} + \mathbf{k_3}$). We measure the phase and amplitude of the signal field ($\mathbf{k_r}$ or $\mathbf{k_n}$) directly with a spectrometer through heterodyne detection by interfering with the local oscillator field.[75,76]

In each experiment, we vary the waiting time (t_2) over a range of picoseconds. For each waiting time, we continuously scan the time delay between the first two pulses. The resulting complex electric field is then Fourier transformed to give the excitation frequency axis (ω_1). Our detection axis (ω_3) is obtained directly by the spectrometer. Increasing the waiting time between our excitation and detection pulses yields changes in the 2D spectrum, which can be ascribed to dynamic processes such as solvation dynamics, intramolecular vibrational redistribution, and vibrational energy transfer.[77]

1.3.2 Spectral Diffusion

Vibrational transition frequencies can vary with different conformations of solvent molecules around the vibrational probe solute or variations in the solute molecule itself, such as conformational changes or changes in electronic state. These

changes can be described as different microenvironments that the solute samples over the timescale of a 2DIR experiment. The result of these variations is spectral inhomogeneity, which manifests itself in the 2DIR spectrum. At short waiting times, when the molecule is unlikely to have sampled a different microenvironment, we observe a strong correlation between the excitation and detection frequency, seen as an elongation of the 2D spectrum along the diagonal. As the waiting time increases, molecules have the opportunity to sample different microenvironments and we observe a broadening of the 2D spectrum across the anti-diagonal as correlation is lost between the excitation and detection frequencies. This loss of correlation is known as spectral diffusion, and the timescale on which it occurs gives insight into the chemical dynamics.[75]

We obtain spectral diffusion timescales by monitoring the frequency-fluctuation correlation function (FFCF), defined as $C(\tau)=\langle\delta\omega(\tau)\delta\omega(0)\rangle$.[78] In our measurements, we use the amplitudes of the rephasing and non-rephasing signals to calculate the inhomogeneity index, I(t), which is directly proportional to the FFCF. The inhomogeneity index is calculated as follows: $(A_r - A_n)/(A_r + A_n)$, where A_r and A_n are the rephasing and non-rephasing amplitudes, respectively.[79] The rephasing pathway produces a photon echo when there is inhomogeneous broadening, whereas the non-rephasing pathway does not yield the photon echo. Subtracting the two amplitudes thus allows us to emphasize the contribution of the echo, which is related to the degree of inhomogeneity in our signal.

1.4 PHOTOCHEMICALLY ACTIVATED COBALAMINS

Cobalamins are complex organometallic biological cofactors containing a central cobalt atom and a distinguishing upper axial ligand. Adenosyl cobalamin (coenzyme B_{12}) is used in radical-based catalysis, where the Co-C bond undergoes homolytic cleavage to yield a reactive radical species used to catalyze a host of radical rearrangement reactions.[80–86] Methylcobalamin also plays an important role in catalysis, as the active coenzyme in methyltransferases such as methionine synthase (see structure of methylcobalamin in **Figure 1.3**).[84,87–89]

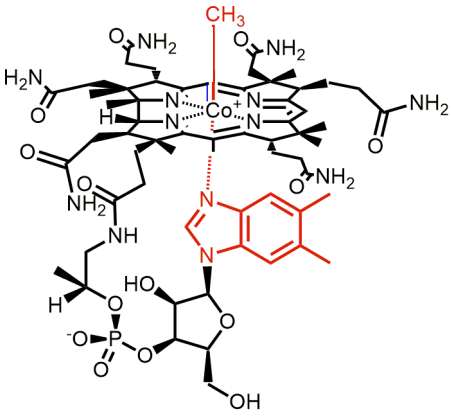

Figure 1.3 Schematic structure of MeCbl. In adenosyl cobalamin, the methyl upper axial group is replaced with a 5'-deoxyadenosyl group.

Photoactivation of these complexes also plays an increasingly important role in chemistry and biology, with the photolysis of adenosyl cobalamin recently found to play a crucial role in photoreceptor CarH.[90–94] Applications of photoactivated cobalamins include providing controlled spatiotemporal drug delivery and the availability of the key vitamin B_{12}.[95–98] The upper axial ligand is easily modified synthetically, opening up the possibility for a wide variety of ligands, further expanding the possibilities taking advantage of the photolability of these molecules, such as adaptation into a system for CO releasing metal carbonyls.[99] Characterization of the photoexcited state of these molecules is thus crucial to developing our understanding of both biological and applied uses of cobalamin photochemistry. Ultrafast time-resolved X-ray absorption spectroscopy performed using X-ray free electron lasers (XFELs) is capable of probing structural changes of short lived following initial photoexcitation.[100–107] Building off of our previous work characterizing the excited-state dynamics of cyanocobalamin using Co K-edge X-ray absorption near-edge structure (XANES) measurements, we now apply this powerful technique to expand our knowledge of this important class of photoactive compounds through probing structural changes in the excited state of methylcobalamin.

1.5 X-RAY ABSORPTION SPECTROSCOPY

While infrared spectroscopy is sensitive to structural changes in response to the environment, x-ray spectroscopy gives atomistic detail about structures and further probes electronic states. There are multiple ways X-ray excitation can be implemented to determine structural information. The most common is X-ray crystallography, where the diffraction pattern obtained through elastic scattering of X-rays off of a crystalline material is used to map the electron density in the crystal, and by extension determine mean atomic positions, bond lengths, and other structural information.[108,109] However, X-ray crystallography has its limitations. It cannot be used for molecules that may be difficult to crystallize or intermediates that cannot be easily isolated, such as excited state species. Removing a molecule such as a protein or virus from its physiological environment and crystallizing may also induce conformational changes, giving an incorrect or potentially irrelevant structure.[110] X-ray absorption spectroscopy provides an alternative to X-ray crystallography, as it can be used with a wide variety of sample conditions, including in solution.

In X-ray absorption spectroscopy (XAS), an edge in the absorption spectrum occurs when a core electron absorbs energy that is greater than or equal to its binding energy, removing the core electron and emitting a photoelectron with kinetic energy equal to the difference between the incident X-ray energy and the binding energy of the core electron. This photoelectron is then able to scatter off of neighboring atoms. The excitation energy for the edge is elementally unique, and the edges are denoted by the shell from which the core electron originated. The metal K-edge transitions (originating from a 1s electron) are sensitive to properties such as oxidation state of the metal and its coordination geometry, making K-edge transitions attractive for the study of transition metal complexes.[111,112] Absorptions lower in energy than the edge are defined as being in the pre-edge region and occur due to 1s → 3d transitions for the metal K-edge.

The features in an X-ray absorption spectrum are divided into two categories defined by their proximity to the edge, each yielding different structural insights. The edge and pre-edge regions yield the X-ray Absorption Near-Edge Structure (XANES) spectrum, spanning from the edge to 20-50 eV above the edge. X-ray absorption measurements performed tens to hundreds of eV higher than the absorption edge yields the extended X-ray absorption fine structure (EXAFS) spectrum, which is dominated by oscillatory features caused by scattering off of neighboring atoms. Further mathematical analysis and Fourier Transform of the features yields information on atomic distances within the molecule. The photoelectron scattering that gives the EXAFS region is dominated by single scattering pathways, where the photoelectron will interact with just one of its neighboring atoms, allowing for cleaner assignment of peaks, although there are contributions from multiple scattering pathways that increase the difficulty of simulating EXAFS spectra.[113] In contrast, scattering in the XANES region proceeds through multiple scattering pathways, where the photoelectron can scatter with multiple neighboring atoms, complicating the direct assignment of peaks to structural features.[114]

Time-resolved XANES spectroscopy allows for observation of how an excited state species evolves over time following excitation. Here, a visible pump pulse is incorporated to excite valence electrons. An X-ray pulse generated by an X-ray free electron laser (XFEL) then excites a core electron to the newly unoccupied valence state or to the continuum, providing information on local electronic and structural changes around the reporter atom following the optical excitation. Time resolved XANES experiments using XFELs are able to be performed on an ultrafast (femtosecond) time scale.[112,115]

1.6 THESIS OUTLINE

This dissertation is organized as follows: **Chapter 2** details the synthesis of both small molecule models of a rhenium tricarbonyl labelled peptide and the peptide itself. 2DIR experiments investigating the effects of changes in electron density in the small molecule models of the rhenium labelled peptide on the solvation

dynamics provide important groundwork for future analysis of solvation dynamics of the peptide. Previously, the Kubarych group explored the effect of changing the electron-withdrawing character of the equatorial diimine ligand of this catalyst and observed minimal effects on the solvation dynamics from this change.[51] Kiefer et al did observe solvent dependence of the spectral diffusion timescale, which they found to correlate with the donicity, or measure of nucleophilicity, of the solvent. Here, we modify the lower axial ligand from a chloride to the better electron-withdrawing benzimidazole, which resembles the histidine side chain that will be used as the attachment site for the rhenium on the labelled peptide. Despite the significant change in electron density induced by the benzimidazole, we observe no change in the solvation dynamics compared to the unmodified catalyst, however we do still find a correlation between spectral diffusion timescale and solvent donicity.

Chapter 3 describes spectroelectrochemical experiments combining 2DIR and traditional electrochemical methods. Using an optically transparent thin-layer electrochemical (OTTLE) cell, we were able to perform the first 2DIR-SEC measurements on two key intermediates in the electrocatalytic cycle for the $Re(bpy)(CO)_3Cl$ (ReCl) catalyst, $Re(bpy)(CO)_3^-$ as well as see a 2DIR signature from the second major intermediate formed in the reduction of the ReCl catalyst, a Re-Re dimer. Our novel 2DIR-OTTLE cell allows for combination 2DIR and electrochemical measurements to be performed in a transmission geometry for the first time, analogous to how they are performed in traditional spectroelectrochemical experiments.

Chapter 4 details time-resolved X-ray absorption near-edge structure (XANES) measurements performed on methylcobalamin. Here, we are able to probe the structure of the long-lived excited state of methylcobalamin, following a 520 nm visible excitation. Our measurements and accompanying simulations of the excited state XANES spectrum indicated that the excited state structure of

methylcobalamin can be characterized by small changes to the axial ligands and a larger expansion of the corrin ring.

Chapter 5 will summarize the work presented in this dissertation and will discuss future directions for this research.

1.7 REFERENCES

1. Stufkens, D. J. & Vlček, A. Ligand-dependent excited state behaviour of Re(I) and Ru(II) carbonyl-diimine complexes. *Coord. Chem. Rev.* (1998). doi:10.1016/s0010-8545(98)00132-5

2. Vlček, A. & Busby, M. Ultrafast ligand-to-ligand electron and energy transfer in the complexes fac-[ReI(L)(CO)3(bpy)]n+. *Coordination Chemistry Reviews* (2006). doi:10.1016/j.ccr.2006.02.002

3. Worl, L. A., Duesing, R., Chen, P., Ciana, L. Della & Meyer, T. J. Photophysical properties of polypyridyl carbonyl complexes of rhenium(I). *J. Chem. Soc. Dalt. Trans.* 849–858 (1991). doi:10.1039/DT9910000849

4. Cannizzo, A. *et al.* Femtosecond fluorescence and intersystem crossing in rhenium(I) carbonyl-bipyridine complexes. *J. Am. Chem. Soc.* **130**, 8967–8974 (2008).

5. Heydová, R. *et al.* Spin-orbit treatment of UV-vis absorption spectra and photophysics of rhenium(I) carbonyl-bipyridine complexes: MS-CASPT2 and TD-DFT analysis. *J. Phys. Chem. A* **116**, 11319–11329 (2012).

6. Takeda, H., Koike, K., Morimoto, T., Inumaru, H. & Ishitani, O. *Photochemistry and photocatalysis of rhenium(I) diimine complexes*. *Advances in Inorganic Chemistry* **63**, (Elsevier Inc., 2011).

7. Takeda, H., Koike, K., Inoue, H. & Ishitani, O. Development of an efficient photocatalytic system for CO2 reduction using rhenium(I) complexes based on mechanistic studies. *J. Am. Chem. Soc.* **130**, 2023–2031 (2008).

8. Kumar, A., Sun, S. S. & Lees, A. J. Photophysics and photochemistry of organometallic rhenium diimine complexes. *Top. Organomet. Chem.* (2010). doi:10.1007/3418_2009_2

9. El Nahhas, A. *et al.* Ultrafast excited-state dynamics of rhenium(I) photosensitizers [Re(Cl)(CO)3(N,N)] and [Re(imidazole)(CO)3(N,N)] +: Diimine effects. *Inorg. Chem.* (2011). doi:10.1021/ic102324p

10. Vaughan, J. G. *et al.* The photochemistry of rhenium(i) tricarbonyl N-heterocyclic carbene complexes. *Dalt. Trans.* (2013). doi:10.1039/c3dt51614h

11. Sato, S. *et al.* Photochemistry of fac-[Re(bpy)(CO)3Cl]. *Chem. - A Eur. J.* (2012). doi:10.1002/chem.201202734

12. Hori, H. *et al.* Photocatalytic reduction of carbon dioxide using [fac-Re(bpy)(CO)3(4-Xpy)]+ (Xpy = pyridine derivatives). *J. Photochem. Photobiol. A Chem.* (1999). doi:10.1016/S1010-6030(98)00430-4

13. Czerwieniec, R., Kapturkiewicz, A., Lipkowski, J. & Nowacki, J. Re(I)(tricarbonyl)+ complexes with the 2-(2-pyridyl)-N-methyl- benzimidazole, 2-(2-pyridyl)benzoxazole and 2-(2-pyridyl)benzothiazole ligands - Syntheses, structures, electrochemical and spectroscopic studies. *Inorganica Chim. Acta* (2005). doi:10.1016/j.ica.2005.03.013

14. Sato, S. *et al.* Photochemical ligand substitution reactions of fac-[Re(bpy)(CO) 3Cl] and derivatives. *Inorg. Chem.* **46**, 3531–3540 (2007).

15. Rodríguez, L. *et al.* Solvent effects on the absorption and emission of [Re(R2bpy)(CO)3X] complexes and their sensitivity to CO2 in solution. *J. Photochem. Photobiol. A Chem.* **204**, 174–182 (2009).

16. Blanco-Rodríguez, A. M. *et al.* Excited-state dynamics of structurally characterized [Re I(CO)3(phen)(HisX)]+ (X = 83, 109) Pseudomonas aeruginosa azurins in aqueous solution. *J. Am. Chem. Soc.* (2006). doi:10.1021/ja057451+

17. Vlček, A. Ultrafast excited-state processes in Re(I) carbonyl-diimine complexes: From excitation to photochemistry. *Top. Organomet. Chem.* (2010). doi:10.1007/3418_2009_4

18. Koike, K. *et al.* Key process of the photocatalytic reduction of CO2 using [Re(4,4′-X2-bipyridine)(CO)3PR3] + (X = CH3, H, CF3; PR3 = phosphorus ligands): Dark reaction of the one-electron-reduced complexes with CO2. *Organometallics* (1997). doi:10.1021/om970608p

19. Wenger, O. S., Henling, L. M., Day, M. W., Winkler, J. R. & Gray, H. B. Photoswitchable Luminescence of Rhenium(I) Tricarbonyl Diimines. *Inorg. Chem.* (2004). doi:10.1021/ic030324z

20. Lee, L. C. C., Leung, K. K. & Lo, K. K. W. Recent development of luminescent rhenium(i) tricarbonyl polypyridine complexes as cellular imaging reagents, anticancer drugs, and antibacterial agents. *Dalton Transactions* (2017). doi:10.1039/c7dt03465b

21. Takeda, H., Koike, K., Morimoto, T., Inumaru, H. & Ishitani, O. *Photochemistry and photocatalysis of rhenium(I) diimine complexes*. *Advances in Inorganic Chemistry* (2011). doi:10.1016/B978-0-12-385904-4.00007-X

22. Fernández-Moreira, V. *et al.* Uptake and localisation of rhenium fac-tricarbonyl polypyridyls in fluorescent cell imaging experiments. *Org. Biomol. Chem.* (2010). doi:10.1039/c004610h

23. Bertrand, H. C., Clède, S., Guillot, R., Lambert, F. & Policar, C. Luminescence modulations of rhenium tricarbonyl complexes induced by structural variations. *Inorg. Chem.* (2014). doi:10.1021/ic5007007

24. Amoroso, A. J. *et al.* Rhenium fac tricarbonyl bisimine complexes: Biologically useful fluorochromes for cell imaging applications. *Chem. Commun.* (2007). doi:10.1039/b706657k

25. Olmon, E. D. *et al.* Charge photoinjection in intercalated and covalently bound [Re(CO) 3(dppz)(py)] +-DNA constructs monitored by time-resolved visible and infrared spectroscopy. *J. Am. Chem. Soc.* (2011). doi:10.1021/ja205568r

26. Kayoko Itokazu, M., Sarto Polo, A. & Murakami Iha, N. Y. Luminescent rigidochromism of fac-[Re(CO)3(phen) (cis-bpe)]+ and its binuclear complex as photosensors. *J. Photochem. Photobiol. A Chem.* (2003). doi:10.1016/S1010-6030(03)00216-8

27. Clède, S. & Policar, C. Metal-carbonyl units for vibrational and luminescence imaging: Towards multimodality. *Chemistry - A European Journal* (2015). doi:10.1002/chem.201404600

28. Vollmer, M. V. *et al.* Synthesis, spectroscopy, and electrochemistry of (α-diimine)M(CO)3Br, M = Mn, Re, complexes: Ligands isoelectronic to bipyridyl show differences in CO2 reduction. *Organometallics* **34**, 3–12 (2015).

29. Rosenfeld, D. E., Gengeliczki, Z., Smith, B. J., Stack, T. D. P. & Fayer, M. D. Structural dynamics of a catalytic monolayer probed by ultrafast 2D IR vibrational echoes. *Science (80-.).* (2011). doi:10.1126/science.1211350

30. Sahara, G. & Ishitani, O. Efficient photocatalysts for CO2 reduction. *Inorg. Chem.* (2015). doi:10.1021/ic502675a

31. Hostachy, S., Policar, C. & Delsuc, N. Re(I) carbonyl complexes: Multimodal platforms for inorganic chemical biology. *Coordination Chemistry Reviews* (2017). doi:10.1016/j.ccr.2017.05.004

32. Hostachy, S. *et al.* Graftable SCoMPIs enable the labeling and X-ray fluorescence imaging of proteins. *Chem. Sci.* (2018). doi:10.1039/c8sc00886h

33. Gray, H. B. & Winkler, J. R. Long-range electron transfer. *Proceedings of the National Academy of Sciences of the United States of America* (2005). doi:10.1073/pnas.0408029102

34. Gray, H. B. & Winkler, J. R. Electron tunneling through proteins. *Quarterly Reviews of Biophysics* (2003). doi:10.1017/S0033583503003913

35. Shih, C. *et al.* Tryptophan-accelerated electron flow through proteins. *Science (80-.).* (2008). doi:10.1126/science.1158241

36. Blanco-Rodríguez, A. M. *et al.* Phototriggering electron flow through ReI-modified pseudomonas aeruginosa azurins. *Chem. - A Eur. J.* (2011). doi:10.1002/chem.201002162

37. Takematsu, K. *et al.* Tryptophan-accelerated electron flow across a protein-protein interface. *J. Am. Chem. Soc.* (2013). doi:10.1021/ja406830d

38. Takematsu, K. *et al.* Two Tryptophans Are Better Than One in Accelerating Electron Flow through a Protein. *ACS Cent. Sci.* (2019). doi:10.1021/acscentsci.8b00882

39. Vlček, A., Kvapilová, H., Towrie, M. & Záliš, S. Electron-Transfer Acceleration Investigated by Time Resolved Infrared Spectroscopy. *Acc. Chem. Res.* (2015). doi:10.1021/ar5004048

40. Winkler, J. R. & Gray, H. B. Electron Transfer in Ruthenium-Modified Proteins. *Chem. Rev.* (1992). doi:10.1021/cr00011a001

41. Yu, F. *et al.* Protein design: Toward functional metalloenzymes. *Chemical Reviews* (2014). doi:10.1021/cr400458x

42. Yu, F., Penner-Hahn, J. E. & Pecoraro, V. L. De novo-designed metallopeptides with type 2 copper centers: Modulation of reduction potentials and nitrite reductase activities. *J. Am. Chem. Soc.* (2013). doi:10.1021/ja406648n

43. Zastrow, M. L. & Pecoraro, V. L. Influence of active site location on catalytic activity in de novo - designed zinc metalloenzymes. *J. Am. Chem. Soc.* (2013). doi:10.1021/ja401537t

44. Blanco-Rodríguez, A. M., Towrie, M., Sýkora, J., Záliš, S. & Vlček, A. Photoinduced intramolecular tryptophan oxidation and excited-state behavior of [Re(L-AA)(CO)3(α-diimine)]+ (L = pyridine or imidazole, AA = tryptophan, tyrosine, phenylalanine). *Inorg. Chem.* (2011). doi:10.1021/ic200252z

45. Wang, L., Middleton, C. T., Zanni, M. T. & Skinner, J. L. Development and validation of transferable amide i vibrational frequency maps for peptides. *J. Phys. Chem. B* (2011). doi:10.1021/jp200745r

46. Lin, Y. S., Shorb, J. M., Mukherjee, P., Zanni, M. T. & Skinner, J. L. Empirical amide I vibrational frequency map: Application to 2D-IR line shapes for isotope-edited membrane peptide bundles. *J. Phys. Chem. B* (2009). doi:10.1021/jp807528q

47. Hamm, P., Lim, M. & Hochstrasser, R. M. Structure of the amide I band of peptides measured by femtosecond nonlinear-infrared spectroscopy. *J. Phys. Chem. B* (1998). doi:10.1021/jp9813286

48. Kim, Y. S. & Hochstrasser, R. M. Dynamics of amide-I modes of the alanine dipeptide in D 2O. *J. Phys. Chem. B* (2005). doi:10.1021/jp0449511

49. Rubtsov, I. V. & Hochstrasser, R. M. Vibrational dynamics, mode coupling, and structural constraints for acetylproline-NH2. *J. Phys. Chem. B* (2002). doi:10.1021/jp020837b

50. Rubtsov, I. V., Wang, J. & Hochstrasser, R. M. Vibrational coupling between amide-I and amide-A modes revealed by femtosecond two color infrared spectroscopy. *J. Phys. Chem. A* (2003). doi:10.1021/jp021922m

51. Kiefer, L. M. & Kubarych, K. J. Solvent-dependent dynamics of a series of rhenium photoactivated catalysts measured with Ultrafast 2DIR. *J. Phys. Chem. A* **119**, 959–965 (2015).

52. Hawecker, J., Lehn, J. -M & Ziessel, R. Photochemical and Electrochemical Reduction of Carbon Dioxide to Carbon Monoxide Mediated by (2,2′-Bipyridine)tricarbonylchlororhenium(I) and Related

Complexes as Homogeneous Catalysts. *Helv. Chim. Acta* (1986). doi:10.1002/hlca.19860690824

53. Yoon Suk Lee, L. & Wong, K. Y. Electrocatalytic Reduction of Carbon Dioxide. *Chem* **3**, 717–718 (2017).

54. Francke, R., Schille, B. & Roemelt, M. Homogeneously Catalyzed Electroreduction of Carbon Dioxide - Methods, Mechanisms, and Catalysts. *Chemical Reviews* (2018). doi:10.1021/acs.chemrev.7b00459

55. Stanton, C. J. *et al.* Re(I) NHC Complexes for Electrocatalytic Conversion of CO2. *Inorg. Chem.* (2016). doi:10.1021/acs.inorgchem.6b00079

56. Du, J. P. & Siewert, I. An Electrochemical and Spectroscopic Study on Re(CO)3(L)Cl in Dimethylformamide (L = 2,2'-Bipyridine). *Zeitschrift fur Anorg. und Allg. Chemie* **3**, 1–8 (2020).

57. Wong, K. Y., Chung, W. H. & Lau, C. P. The effect of weak Brönsted acids on the electrocatalytic reduction of carbon dioxide by a rhenium tricarbonyl bipyridyl complex. *J. Electroanal. Chem.* (1998). doi:10.1016/S0022-0728(98)00116-8

58. Johnson, F. P. A., George, M. W., Hartl, F. & Turner, J. J. Electrocatalytic reduction of CO2using the complexes [Re(bpy)(CO)3L]n(n = +1, L = P(OEt)3, CH3CN; n = 0, L = Cl-, Otf-; bpy = 2,2′-bipyridine; Otf-= CF3SO3) as catalyst precursors: Infrared spectroelectrochemical investigation. *Organometallics* **15**, 3374–3387 (1996).

59. Nakada, A. & Ishitani, O. Selective Electrocatalysis of a Water-Soluble Rhenium(I) Complex for CO2 Reduction Using Water As an Electron Donor. *ACS Catal.* (2018). doi:10.1021/acscatal.7b03275

60. Nganga, J. K. *et al.* Electrochemical Reduction of CO2 Catalyzed by Re(pyridine-oxazoline)(CO)3Cl Complexes. *Inorg. Chem.* (2017). doi:10.1021/acs.inorgchem.6b02384

61. Cao, S. H. *et al.* In Situ Monitoring Potential-Dependent Electrochemical Process by Liquid NMR Spectroelectrochemical Determination: A Proof-of-Concept Study. *Anal. Chem.* **89**, 3810–3813 (2017).

62. Zhou, X. *et al.* Graphene-Immobilized fac-Re(bipy)(CO)3Cl for Syngas Generation from Carbon Dioxide. *ACS Appl. Mater. Interfaces* (2016). doi:10.1021/acsami.5b11958

63. Smieja, J. M. & Kubiak, C. P. Re(bipy-tBu)(CO)3Cl-improved catalytic activity for reduction of carbon dioxide: IR-spectroelectrochemical and mechanistic studies. *Inorg. Chem.* **49**, 9283–9289 (2010).

64. Smieja, J. M. *et al.* Kinetic and structural studies, origins of selectivity, and interfacial charge transfer in the artificial photosynthesis of CO. *Proc. Natl. Acad. Sci. U. S. A.* **109**, 15646–15650 (2012).

65. Agarwal, J., Fujita, E., Schaefer, H. F. & Muckerman, J. T. Mechanisms for CO production from CO 2 using reduced rhenium tricarbonyl catalysts. *J. Am. Chem. Soc.* **134**, 5180–5186 (2012).

66. Wilting, A., Stolper, T., Mata, R. A. & Siewert, I. Dinuclear Rhenium Complex with a Proton Responsive Ligand as a Redox Catalyst for the Electrochemical CO2 Reduction. *Inorg. Chem.* (2017). doi:10.1021/acs.inorgchem.7b00178

67. Manbeck, G. F., Muckerman, J. T., Szalda, D. J., Himeda, Y. & Fujita, E. Push or Pull? Proton Responsive Ligand Effects in Rhenium Tricarbonyl CO2 Reduction Catalysts. *J. Phys. Chem. B* (2015). doi:10.1021/jp511131x

68. Riplinger, C., Sampson, M. D., Ritzmann, A. M., Kubiak, C. P. & Carter, E. A. Mechanistic contrasts between manganese and rhenium bipyridine electrocatalysts for the reduction of carbon dioxide. *J. Am. Chem. Soc.* **136**, 16285–16298 (2014).

69. Riplinger, C. & Carter, E. A. Influence of weak Bronsted acids on electrocatalytic CO2 reduction by manganese and rhenium bipyridine catalysts. *ACS Catal.* (2015). doi:10.1021/cs501687n

70. Paolucci, F. *et al.* Dynamics of the electrochemical behavior of diimine tricarbonyl rhenium(I) complexes in strictly aprotic media. *J. Phys. Chem. B* (1998). doi:10.1021/jp980659f

71. Hawecker, J., Lehn, J. M. & Ziessel, R. Electrocatalytic reduction of carbon dioxide mediated by Re(bipy)(CO) 3Cl (bipy = 2,2′-bipyridine). *J. Chem. Soc. Chem. Commun.* (1984). doi:10.1039/C39840000328

72. Kiefer, L. M., King, J. T. & Kubarych, K. J. Equilibrium excited state dynamics of a photoactivated catalyst measured with ultrafast transient 2DIR. *J. Phys. Chem. A* **118**, 9853–9860 (2014).

73. Kiefer, L. M. & Kubarych, K. J. Solvent exchange in preformed photocatalyst-donor precursor complexes determines efficiency. *Chem. Sci.* **9**, 1527–1533 (2018).

74. Nee, M. J., McCanne, R., Kubarych, K. J. & Joffre, M. Two-dimensional infrared spectroscopy detected by chirped pulse upconversion. *Opt. Lett.* (2007). doi:10.1364/ol.32.000713

75. Khalil, M., Demirdöven, N. & Tokmakoff, A. Coherent 2D IR spectroscopy: Molecular structure and dynamics in solution. *J. Phys. Chem. A* **107**, 5258–5279 (2003).

76. Zhang, W. M., Chernyak, V. & Mukamel, S. Multidimensional femtosecond correlation spectroscopies of electronic and vibrational excitons. *J. Chem. Phys.* (1999). doi:10.1063/1.478400

77. Kiefer, L. M. & Kubarych, K. J. Two-dimensional infrared spectroscopy of coordination complexes: From solvent dynamics to photocatalysis. *Coord. Chem. Rev.* **372**, 153–178 (2018).

78. Mukamel, S. *Principles of Nonlinear Optical Spectroscopy, Oxford University Press, New York*. *Principles of Nonlinear Optical Spectroscopy, Oxford University Press, New York* (1995).

79. Roberts, S. T., Loparo, J. J. & Tokmakoff, A. Characterization of spectral diffusion from two-dimensional line shapes. *J. Chem. Phys.* **125**, (2006).

80. Marsh, E. N. G. & Meléndez, G. D. R. Adenosylcobalamin enzymes: Theory and experiment begin to converge. *Biochimica et Biophysica Acta - Proteins and Proteomics* (2012). doi:10.1016/j.bbapap.2012.03.012

81. Marsh, E. N. G., Patterson, D. P. & Li, L. Adenosyl radical: Reagent and catalyst in enzyme reactions. *ChemBioChem* (2010). doi:10.1002/cbic.200900777

82. Bridwell-Rabb, J. & Drennan, C. L. Vitamin B12 in the spotlight again. *Current Opinion in Chemical Biology* (2017). doi:10.1016/j.cbpa.2017.01.013

83. Banerjee, R. & Ragsdale, S. W. The Many Faces of Vitamin B 12 : Catalysis by Cobalamin-Dependent Enzymes . *Annu. Rev. Biochem.* (2003). doi:10.1146/annurev.biochem.72.121801.161828

84. Giedyk, M., Goliszewska, K. & Gryko, D. Vitamin B12 catalysed reactions. *Chemical Society Reviews* (2015). doi:10.1039/c5cs00165j

85. Sauer, K. & Thauer, R. K. Chemistry and Biochemistry of B12. in *Chemistry and Biochemistry of B12* (1999).

86. Toraya, T. Radical catalysis of B12 enzymes: Structure, mechanism, inactivation, and reactivation of diol and glycerol dehydratases. *Cellular and Molecular Life Sciences* (2000). doi:10.1007/s000180050502

87. Gruber, K., Puffer, B. & Kräutler, B. Vitamin B12-derivatives - Enzyme cofactors and ligands of proteins and nucleic acids. *Chemical Society Reviews* (2011). doi:10.1039/c1cs15118e

88. Banerjee, R. V., Frasca, V., Ballou, D. P. & Matthews, R. G. Participation of Cob(I)alamin in the Reaction Catalyzed by Methionine Synthase from Escherichia coli: A Steady-State and Rapid Reaction Kinetic Analysis. *Biochemistry* (1990). doi:10.1021/bi00502a013

89. Drennan, C. L., Matthews, R. G. & Ludwig, M. L. Cobalamin-dependent methionine synthase: the structure of a methylcobalamin-binding fragment and implications for other B12-dependent enzymes. *Curr. Opin. Struct. Biol.* (1994). doi:10.1016/0959-440X(94)90275-5

90. Padmanabhan, S., Jost, M., Drennan, C. L. & Elías-Arnanz, M. A New Facet of Vitamin B 12 : Gene Regulation by Cobalamin-Based Photoreceptors . *Annu. Rev. Biochem.* **86**, 485–514 (2017).

91. Jost, M. *et al.* Structural basis for gene regulation by a B12-dependent photoreceptor. *Nature* **526**, 536–541 (2015).

92. Kutta, R. J. *et al.* The photochemical mechanism of a B 12-dependent photoreceptor protein. *Nat. Commun.* **6**, (2015).

93. Ortiz-Guerrero, J. M., Polanco, M. C., Murillo, F. J., Padmanabhan, S. & Elías-Arnanz, M. Light-dependent gene regulation by a coenzyme B12-based photoreceptor. *Proc. Natl. Acad. Sci. U. S. A.* (2011). doi:10.1073/pnas.1018972108

94. Pérez-Marín, M. C., Padmanabhan, S., Polanco, M. C., Murillo, F. J. & Elías-Arnanz, M. Vitamin B12 partners the CarH repressor to downregulate a photoinducible promoter in Myxococcus xanthus. *Mol. Microbiol.* (2008). doi:10.1111/j.1365-2958.2007.06086.x

95. Shell, T. A., Shell, J. R., Rodgers, Z. L. & Lawrence, D. S. Tunable Visible and Near IR Photoactivation of Light-Responsive Compounds. **53**, 875–878 (2015).

96. Shell, T. A. & Lawrence, D. S. Vitamin B12: A Tunable, Long Wavelength, Light-Responsive Platform for Launching Therapeutic Agents. *Acc. Chem. Res.* **48**, 2866–2874 (2015).

97. Miller, N. A. *et al.* Toward the Design of Photoresponsive Conditional Antivitamins B12: A Transient Absorption Study of an Arylcobalamin and an Alkynylcobalamin. *J. Am. Chem. Soc.* **138**, 14250–14256 (2016).

98. Kräutler, B. Antivitamins B12 - A Structure- and Reactivity-Based Concept. *Chem. - A Eur. J.* **21**, 11280–11287 (2015).

99. Santoro, G., Zlateva, T., Ruggi, A., Quaroni, L. & Zobi, F. Synthesis, characterization and cellular location of cytotoxic constitutional organometallic isomers of rhenium delivered on a cyanocobalmin scaffold. *Dalt. Trans.* (2015). doi:10.1039/c4dt03598d

100. Zerdane, S. *et al.* Probing Transient Photoinduced Charge Transfer in Prussian Blue Analogues with Time-Resolved XANES and Optical Spectroscopy. *Eur. J. Inorg. Chem.* **2018**, 272–277 (2018).

101. Miller, N. A. *et al.* Ultrafast X-ray Absorption Near Edge Structure Reveals Ballistic Excited State Structural Dynamics. *J. Phys. Chem. A* **122**, 4963–4971 (2018).

102. Miller, N. A. *et al.* Polarized XANES monitors femtosecond structural evolution of photoexcited Vitamin B12. *J. Am. Chem. Soc.* **139**, 1894–1899 (2017).

103. Shelby, M. L. *et al.* Ultrafast Excited State Relaxation of a Metalloporphyrin Revealed by Femtosecond X-ray Absorption Spectroscopy. *J. Am. Chem. Soc.* **138**, 8752–8764 (2016).

104. Chen, L. X. *et al.* Imaging ultrafast excited state pathways in transition metal complexes by X-ray transient absorption and scattering using X-ray free electron laser source. *Faraday Discuss.* **194**, 639–658 (2016).

105. Subramanian, G. *et al.* Direct Structural and Chemical Characterization of the Photolytic Intermediates of Methylcobalamin Using Time-Resolved X-ray Absorption Spectroscopy. *J. Phys. Chem. Lett.* **9**, 1542–1546 (2018).

106. Levantino, M. *et al.* Observing heme doming in myoglobin with femtosecond X-ray absorption spectroscopy. *Struct. Dyn.* **2**, (2015).

107. Lemke, H. T. *et al.* Coherent structural trapping through wave packet dispersion during photoinduced spin state switching. *Nat. Commun.* **8**, (2017).

108. Woolfson, M. M. An Introduction to X-Ray Crystallography. *Phys. Today* (1971). doi:10.1063/1.3022888

109. Smyth, M. S. & Martin, J. H. J. x Ray crystallography. *Journal of Clinical Pathology - Molecular Pathology* (2000). doi:10.1136/mp.53.1.8

110. Ryu, W. S. *Molecular Virology of Human Pathogenic Viruses*. *Molecular Virology of Human Pathogenic Viruses* (2016). doi:10.1016/c2013-0-15172-0

111. Chen, L. X., Zhang, X. & Shelby, M. L. Recent advances on ultrafast X-ray spectroscopy in the chemical sciences. *Chem. Sci.* **5**, 4136–4152 (2014).

112. Chergui, M. Time-resolved X-ray spectroscopies of chemical systems: New perspectives. *Struct. Dyn.* **3**, (2016).

113. Penner-Hahn, J. E. X-ray Absorption Spectroscopy. in *Encyclopedia of Life Sciences* (2005). doi:10.1038/npg.els.0002984

114. Bressler, C. & Chergui, M. Ultrafast x-ray absorption spectroscopy. *Chem. Rev.* **104**, 1781–1812 (2004).

115. Chollet, M. *et al.* The X-ray Pump-Probe instrument at the Linac Coherent Light Source. *J. Synchrotron Radiat.* **22**, 503–507 (2015).

Chapter 2 Synthesis and Vibrational Dynamics of a Small Molecule Model for a Rhenium Tricarbonyl Labelled Peptide System

2.1 INTRODUCTION

Electron transfer is an essential process in biology. The current model of electron transfer (ET) is given by Marcus theory, which defines the reaction coordinate as the polarization of charge from proceeding from the neutral to charge transfer state.[1] Under this definition, the electron transfer event occurs when the nuclear degrees of freedom fluctuate in such a way that the electron experiences no energetic cost in going from donor to acceptor. In the condensed phase, structural and solvent fluctuations modulate this energy barrier. Therefore, understanding the dynamics of the equilibrium fluctuations of the solvent and the molecule itself, both before and after the electron transfer, is key to understanding how electron transfer occurs in solution.

Two-dimensional infrared (2DIR) spectroscopy has proven to be a powerful tool for measuring equilibrium structural and solvent fluctuations.[2] In order to study electron transfer using optical spectroscopy, a phototriggerable modulator of the driving force is needed.[3–6] Transient 2DIR spectroscopy incorporates an actinic pulse before the equilibrium 2DIR pulse sequence described in detail elsewhere in this dissertation. This method allows for the photo-induction of the electron transfer as well as monitoring of the system before and after the transfer occurs. Harry Gray and Antonin Vlcek found that rhenium tricarbonyl diimine complexes are excellent photooxidants and can be used as phototriggers of ET in azurins, copper containing proteins.[5,7–10] The mechanism for the ET process is given in **Figure 2.1**, and can be briefly described as follows: Upon electronic excitation with 400 nm light, the rhenium tricarbonyl diimine photooxidant in the singlet

metal to ligand charge transfer (^{1}MLCT) state undergoes intersystem crossing in ~110 fs to the triplet metal to ligand charge transfer (^{3}CT) state. Within a few nanoseconds, the triplet state establishes an equilibrium with a charge separated state centered on a neighboring tryptophan residue. This charge separated state then either undergoes a tens of ns diimine ligand to tryptophan electron transfer recombination, or undergoes a competitively fast copper(I) to tryptophan electron transfer, resulting in the oxidation of the Cu(I) metal center in the azurin protein.[5,9–11]

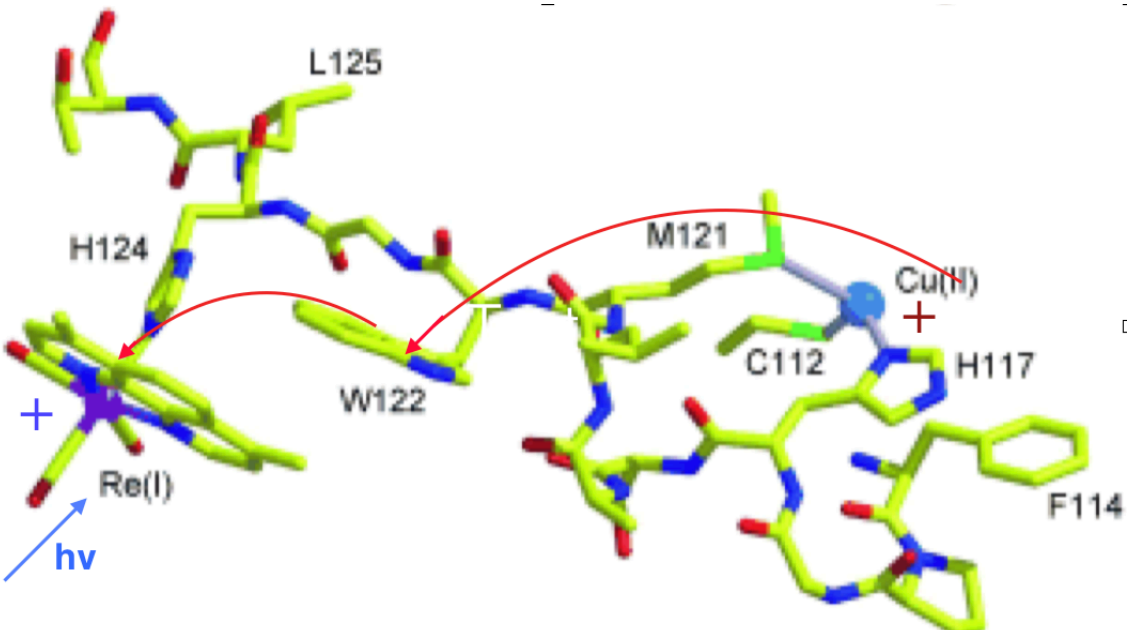

Figure 2.1 Cartoon representation of the mechanism for photoinduction of electron transfer via rhenium tricarbonyl label as proposed by Vlcek and Gray.[9]

The majority of the work previously performed on this system utilized transient IR absorption measurements of the phototrigger to monitor changes in the system as a result of the occurrence of the electron transfer event. This system seems to be an ideal candidate for two-dimensional infrared spectroscopy, as it contains multiple vibrational probes that will be sensitive to changes in hydration or electronic structure of the system, including the rhenium moiety and the carbonyls in the peptide backbone. Incorporation of this “hopping” electron transfer mechanism into a smaller and more editable system would allow for greater control over the degrees of freedom that are key to the occurrence and efficiency of this process, such as the distance between the rhenium, tryptophan,

and copper centers, and the environment around of each of these pieces of the mechanism. Previously, in conjunction with the Pecoraro group at the University of Michigan, we were able to characterize the active site and dynamics of a *de novo* Cu-containing homotrimer metalloenzyme.[12] This system, with its complete customizability, provides a convenient and easily modified platform to monitor electron transfer, while maintaining important similarities to natural proteins, such as a hydrophobic interior and functional metal active site, which could be oxidized by the rhenium through the same mechanism as the azurin copper. The basic sequence of this peptide is a heptadic repeat, LKALEEK.[13–15] Amino acid substitutions can be made provided they do not disrupt the overall pattern of the peptide, requiring locations 1 and 4 to be hydrophobic residues, and 5 and 7 to be salt-bridging residues. By substituting a histidine residue for one of the glutamate residues, the peptide can be labelled with a rhenium diimine tricarbonyl complex through the method used by Vlcek on the azurins.[5,7,9,10] A tryptophan residue can be substituted for the alanine in position three, providing the necessary stepping-stone for the electron transfer from the rhenium to the copper center.[8,11] The complete control over the sequence of the peptide also allows for easy incorporation of isotope labelling in the backbone carbonyls, giving greater site-specificity into changes in the peptide conformation before, after, and during the electron transfer event.[16–22]

The rhenium diimine tricarbonyl complex, in addition to providing a suitable vibrational probe label for peptides, is commonly studied as Re(diimine)(bpy)X, where X is often a halide ligand, due to its ability to both photo- and electro-catalytically reduce CO_2 to CO.[23] Many aspects of the design of these catalysts have been explored for their effect on the overall catalytic behavior, such as changes to the solvent, changes to the axial ligand (X), and modification of the diimine ligand, with the goal of better understanding the CO_2 reduction mechanism and improving catalytic efficiency.[24–37] The Kubarych group previously studied the long-lived ^{3}MLCT state generated as the initial product following photoactivation of the rhenium catalyst using 2DIR.[38] We observed that

the solvation dynamics of the excited state species undergo a three-fold slowdown relative to those of the ground state, which we attributed to multiple factors, including increased dielectric friction caused by changing the dipole moment in the excited state. This result then prompted an investigation into the effects of changing the dipole moment of the molecule on its solvation dynamics, where the diimine ligand was substituted with a series of ligands chosen to be either more or less electron-withdrawing than the traditional bipyridine.[39] While we only observed minimal to no changes to the dynamics across the series, there was a change in the carbonyl stretching frequencies based on the character of the ligand, indicating that the carbonyls are sensitive to these changes in the overall electronic structure of the molecule.

Having investigated the influence of changes to the diimine ligand on the solvation dynamics of the rhenium catalyst, we now focus on the effect of the electron-withdrawing character of the axial ligand. Given the sensitivity of the carbonyls to the overall electronic structure of the molecule, it is important to understand how the changes to the rhenium diimine tricarbonyl motif induced by replacing the axial ligand affect the solvation dynamics, so that contributions from the changes in electron density caused by the replacement of the axial halide ligand can be separated out from changes that may be induced from the peptide itself. Here, we replace the traditional halogen lower axial ligand with a more electron-withdrawing benzimidazole ligand, forming the positively charged $Re(bpy)(CO)_3(benzimidazole)^+$ ($[ReBenzIm]^+$), and compare the solvation dynamics of this molecule to both the ground and excited state of its parent ReCl molecule (**Figure 2.2**). Additionally, we provide a procedure in this chapter for successfully labelling a small 7-amino acid peptide with the rhenium diimine tricarbonyl moiety, and provide FTIR spectra of the labelled peptide.

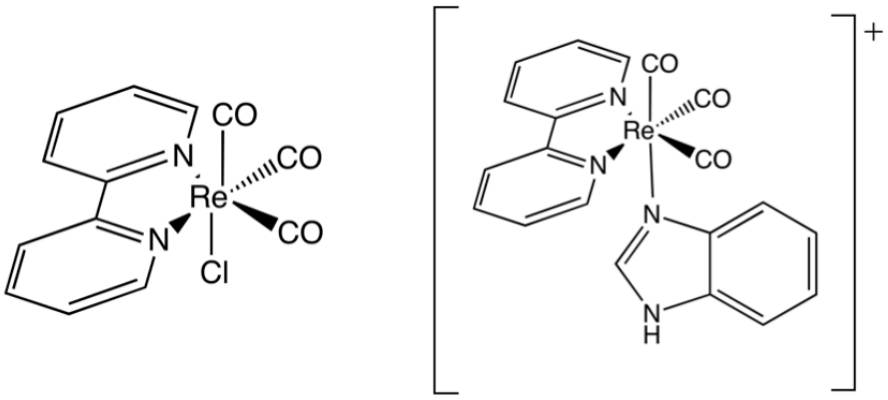

Figure 2.2 Structures of parent $Re(bpy)(CO)_3Cl$ (ReCl) (left) and $[Re(bpy)(CO)_3(benzimidazole)]^+$ [ReBenzIm]+ (right).

2.2 EXPERIMENTAL METHODS

2.2.1 Equilibrium 2DIR Spectroscopy

Our 2DIR methods have been thoroughly described elsewhere.[40] We use 800 nm pulses from a regenerative amplifier to pump two independent optical parametric amplifiers (OPAs). The resulting light generated in the OPAs goes on to drive two separate AgGaS difference-frequency-generating (DFG) crystals, giving ~2000 cm^{-1} (125 cm^{-1} fwhm) infrared light. This light is then split, yielding three femtosecond infrared pulses, E_1, E_2, and E_3 that interact with the sample to generate the third-order nonlinear signal, as well as a local oscillator field, which allows us to measure the signal using heterodyne detection.[41]

A 2DIR experiment has three time delays, each following its corresponding pulse of E_1, E_2, or E_3. The first time delay, t_1, is the coherence evolution period, followed by the waiting time delay (t_2), and the detection coherence period (t_3). The three pulses interact with the sample in a noncollinear box geometry, giving the emitted signal in a background-free direction. For each waiting time delay (t_2) between the pump pulses (E_1 and E_2) and the probe pulse (E_3), we perform both a rephasing and non-rephasing experiment. In the rephasing pathway the coherences formed during the t_1 coherence evolution period have conjugate phases to the coherences generated in the coherence detection period t_3

whereas in the non-rephasing pathway, the coherences evolve with the same phase during the evolution and detection periods.

For each experiment, the t_1 time delay between the two pump pulses is scanned using a pair of ZnSe wedges in the path of each pump pulse. The signal at each detection frequency (w_3) is Fourier transformed to give the w_1 excitation axis. The detection frequency axis is obtained directly by Fourier transformation performed by a spectrometer[42], with the mid-IR signal and local oscillator undergo chirped pulse upconversion to be measured in the visible with a CCD camera.[41]

By increasing the waiting time between the excitation and detection pulses, we are able to observe processes such as spectral diffusion, vibrational energy transfer, and vibrational energy relaxation.[43] We are able to attribute the changes these processes induce in our observed spectra over the series of time delays to solvation and structural dynamics.[43]

A 2D-IR spectrum correlates the excitation and detection frequencies, At early waiting times, the probe molecule has not had time to sample different microenvironments, and the excitation and detection frequencies are well correlated. This is represented in the 2D peak as a slant in the peak shape along the diagonal. As the waiting time t_2 increases and the probe molecule is able to sample new environments, the correlation between the excitation and detection frequencies is lost, through a process called spectral diffusion. As the molecule undergoes spectral diffusion, the peak shape becomes more symmetric. The timescale on which spectral diffusion is an observable that can be linked to the solvation environment of the probe molecule.[44] The asymmetry in the 2D peak shape can be measured in multiple ways and is related to the frequency fluctuation correlation function (FFCF). The FFCF is written as $C(t) = \langle \delta\omega(0)\delta\omega(t) \rangle$, where $\delta\omega(t)$ is the instantaneous fluctuation from the average frequency.[45] One such measurement of the asymmetry in the peak shape is the inhomogeneity index, *I(t)*, given by the following definition: $I(t) = (A_r - A_n)/(A_r +$

A_n), where A_r is the amplitude of the rephasing signal, and A_n is the amplitude of the non-rephasing signal.[46] The inhomogeneity index is directly proportional to the FFCF. For each sample, the inhomogeneity index was measured to compare the frequency-fluctuation correlation function between samples, and thus draw out the timescale for spectral diffusion.

2.2.2 Sample Preparation

Samples were prepared using literature procedures.[10] $Re(bpy)(CO)_3(BenzIm)^+$ (**Figure 2.2**) was synthesized by combining equimolar (0.5 mmol) amounts of $Re(bpy)(CO)_3Cl$[48] and AgOTf in THF and refluxing for 30 minutes before adding 5 mmol of benzimidazole and refluxing for another two hours. The resulting solution was cooled and evaporated. The crude product was dry packed onto a silica column and washed with a mixture of acetonitrile (80%) and water (20%). The resulting product was then dissolved in methanol and filtered to remove remaining excess unreacted benzimidazole. The filtrate was evaporated followed by the addition of boiling saturated KNO_3 solution to precipitate the final product.

A 7-aa peptide with the sequence LKWLEHK was purchased from and purified by Biomatik (purity >80%, MW = 953 g/mol) and used as received. Rhenium pentacarbonyl chloride and 2,2-bipyridine were refluxed for 3 hours in toluene to form $Re(bpy)(CO)_3Cl$. The product was dried, then dissolved in dichloromethane with triflic acid added dropwise to yield $Re(bpy)(CO)_3OTf$ and HCl. The light-yellow product can be precipitated out with <90% yield by slow addition of diethyl ether. $Re(bpy)(CO)_3OTf$ was then combined in a 2:1 ratio with the peptide in 10 mM HEPES buffer in D_2O and heated in the dark to 37°C for one week, inverting the vial once a day to agitate the solution. The resulting solution was then centrifuged to remove excess unreacted rhenium, and attachment was confirmed using mass spectroscopy. All other reagents were ordered from Sigma and used as received.

2.2.3 Computational Methods

DFT calculations of the vibrational spectrum of $[ReBenzIm]^+$ were performed using the B3LYP functional and 6-31(d,p) basis set, using the SDD pseudopotential for the Re.[49]

2.3 RESULTS

2.3.1 FTIR Measurements

We characterized $[ReBenzIm]^+$ in three polar aprotic solvents: dimethyl sulfoxide (DMSO), acetonitrile (ACN), and tetrahydrofuran (THF). The FTIR spectrum of the carbonyls in $[ReBenzIm]^+$ exhibits an overall blue shift of about 10 cm^{-1} relative to the spectrum of ReCl (**Figure 2.3 A**). We observe a solvent dependent carbonyl peak shift of the carbonyl stretches consistent with the trend seen by Kiefer et al. for the parent ReCl molecule (**Figure 2.3 B**)

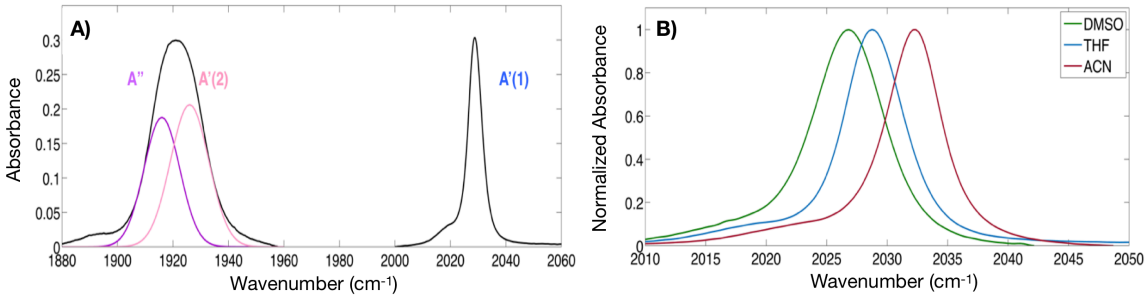

Figure 2.3 A) FTIR Spectrum of [ReBenzIm]+ in THF, with peak assignment to vibrational modes for the metal carbonyl region of the spectrum. B) A'(1) mode of [ReBenzIm]+ in DMSO, THF, and CAN, showing the observed solvent-dependent peak shift.

The structure of the labelled seven amino acid length peptide with the sequence LKWLEHK is given in **Figure 2.4**. The FTIR spectrum of the labelled peptide in D_2O is given in **Figure 2.5**, with peaks consistent with the azurin-bound rhenium tricarbonyl reported by Vlcek et al at ~2032 cm^{-1} and 1925 cm^{-1}.[10]

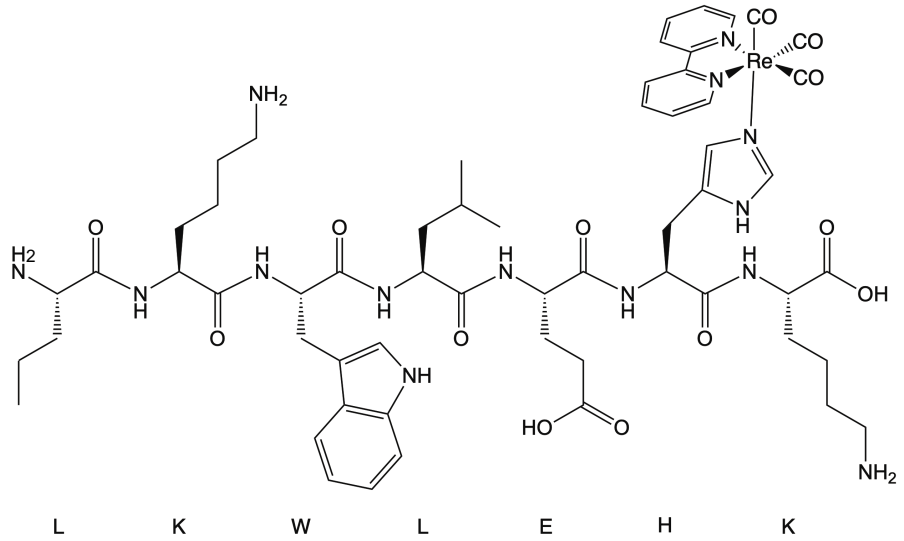

Figure 2.4 Structure of heptad peptide with the sequence LKWLEHK labelled with Re(bpy)(CO)$_3$ through the histidine side chain.

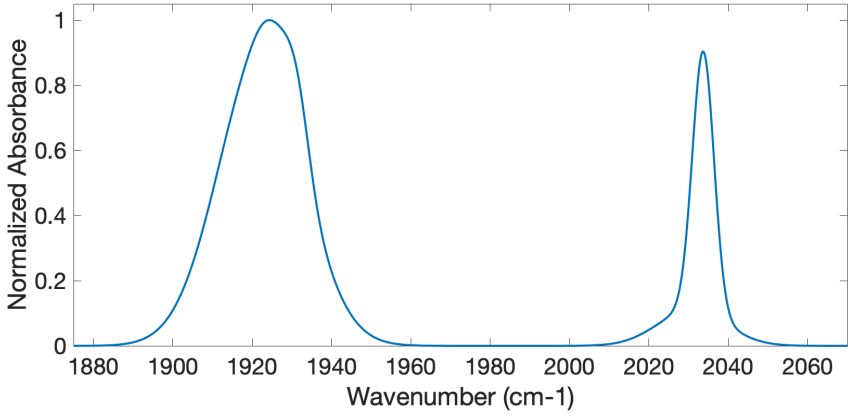

Figure 2.5 FTIR Spectrum of the metal carbonyl region of the heptad peptide labelled with Re(bpy)(CO)3 in D2O. The symmetric A'(1) stretching mode is at ~2030 cm^{-1}, and the two lower frequency modes appear as one peak at ~1925 cm^{-1}

2.3.2 Equilibrium 2DIR measurements

We performed equilibrium 2DIR experiments in ACN, DMSO, and THF to characterize the solvation dynamics of the [ReBenzIm]$^+$ molecule. These polar aprotic solvents were chosen to provide direct comparison to the previous work done for the series of modified bipyridine ReCl derivatives.[39] For these

measurements, we focused on the high frequency A'(1) stretching mode (2029 cm^{-1} in THF). An absorptive 2D-IR spectrum of this mode can be seen in **Figure 2.6**.

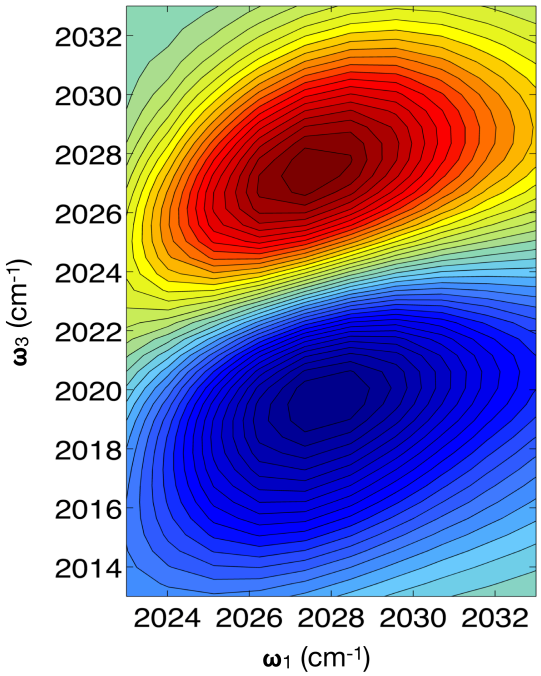

Figure 2.6 Absorptive 2DIR spectrum at 0.4 ps of the 2029 cm^{-1} peak of [ReBenzIm]+ in THF

We find $[ReBenzIm]^+$ to exhibit similar dynamics to ReCl in these solvents. The spectral diffusion time constants determined for $[ReBenzIm]^+$ are as follows: ACN: 2.4 ± 0.7 ps, DMSO: 3.6 ± 0.6 ps, and THF: 3.2 ± 0.5 ps. The FFCFs and fits giving the spectral diffusion timescales are plotted in **Figure 2.7**.

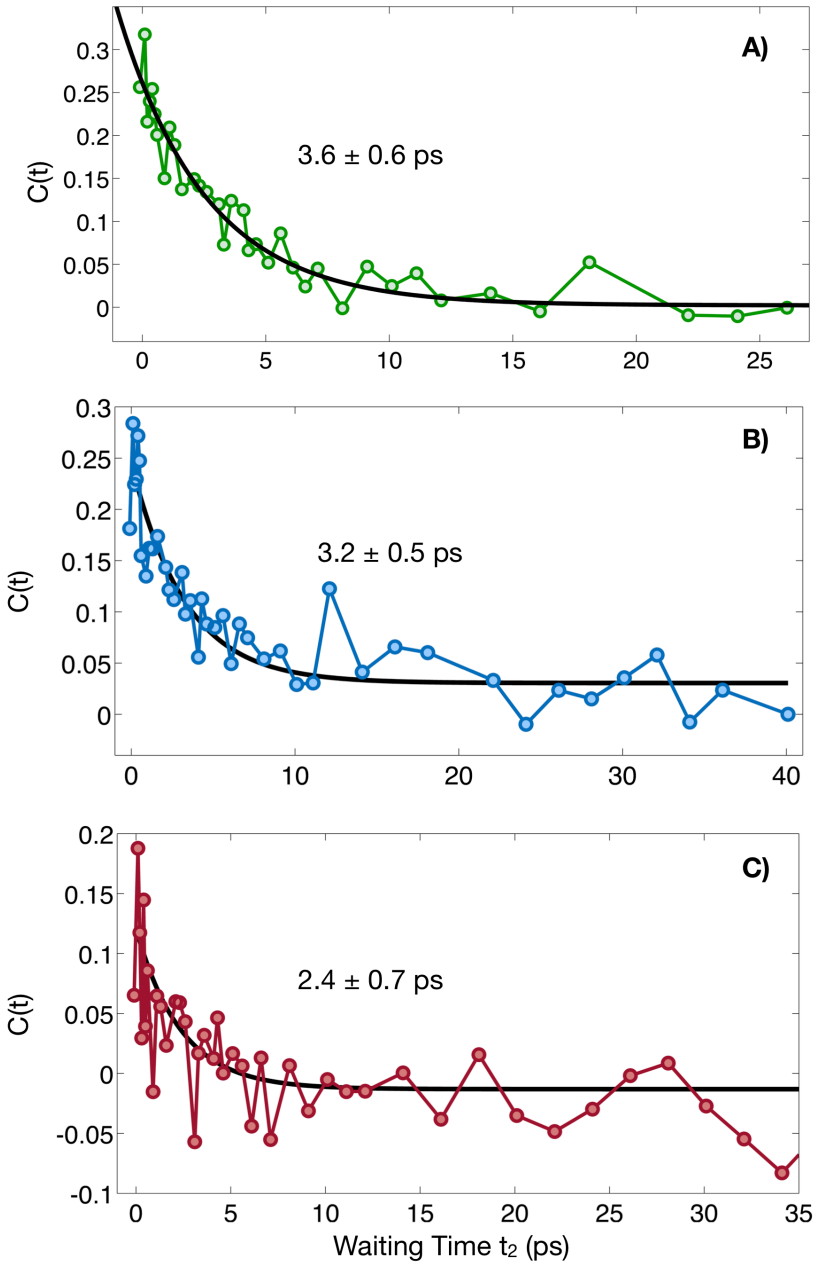

Figure 2.7 Solvation dynamics of [ReBenzIm]+ probed in A) DMSO, B) THF, and C) acetonitrile. Spectral diffusion timescales are shown on the figure.

2.4 DISCUSSION

Our FTIR measurements show an overall blue shift of the $[ReBenzIm]^+$ spectrum relative to that of the ReCl spectrum. In the ReCl FTIR spectrum (**Figure 2.8**), the peaks appear in the following order, in ascending frequency: A", A'(2), and A'(1). Analysis of the $[ReBenzIm]^+$ spectrum in combination with DFT calculated peak assignments reveals a "switching places" in frequency between the A'(2)

mode and the A" mode. The A'(2) mode experiences a stronger blue shift than the A" mode. This effect has previously been reported in the FTIR spectrum of the ^{3}MLCT state of ReCl, which is also blue shifted.[38,50] We thus attribute both the blue shift and the switching of the two lower frequencies to the decrease in electron density on the rhenium caused by the electron-withdrawing axial benzimidazole ligand. Previous work by Kiefer et al demonstrated the lack of this effect on the FTIR spectrum when diimine ligands of varying electron-withdrawing or donating character were substituted for the standard bipyridine ligand.[39] Our results from the $[ReBenzIm]^+$ indicate that the carbonyl frequencies are more sensitive to changes in the axial ligand than the equatorial.

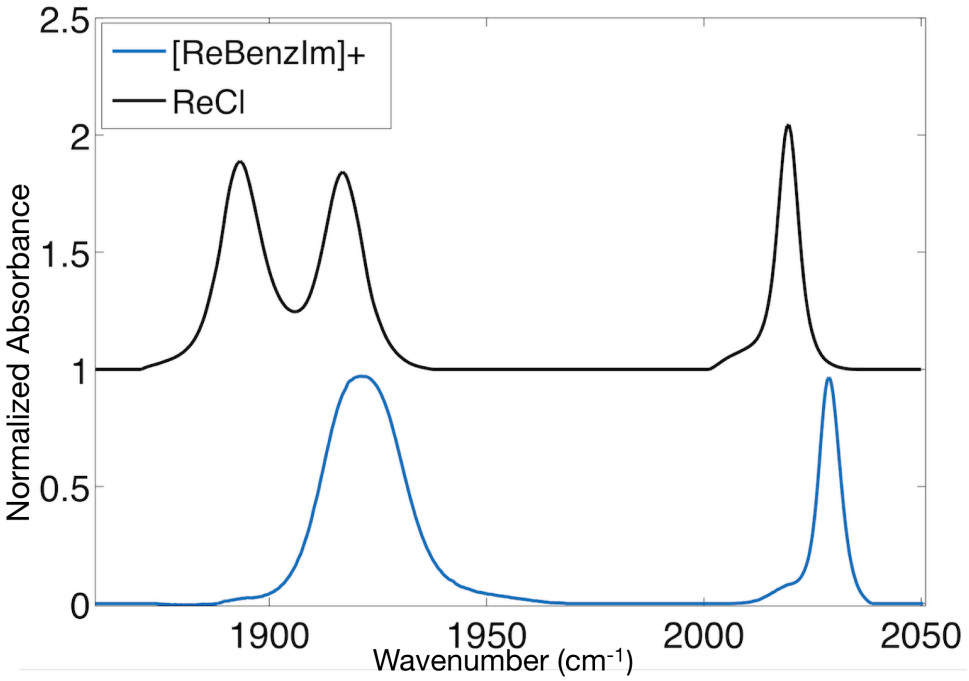

Figure 2.8 Comparison of the normalized FTIR spectra in THF for ReCl (black) and $[ReBenzIm]^+$.

The overall trend of increasing spectral diffusion timescale across the following series: ACN < THF < DMSO was previously observed by Kiefer et al in the parent ReCl. The trend was found to correlate with the donicity, or nucleophilic properties of the solvent.[39,51] Despite the significant shift between the FTIR spectra, the dynamics of $[ReBenzIm]^+$ are similar to that of ReCl, indicating that

although the change in electron density on the rhenium changes the frequencies of the vibrations, the dynamic behavior is unaffected by this axial ligand.

2.5 CONCLUSIONS

Changing the electron density within the photocatalyst $Re(bpy)(CO)_3Cl$ by replacing its lower axial Cl ligand with a more electron-withdrawing benzimidazole group had no measurable effect on the solvation dynamics of the molecule. We did observe a significant (10 cm^{-1}) blue shift in the FTIR spectrum of the benzimidazole molecule, as well as a "switching places" in frequency of the two lower frequency carbonyl stretching modes, reminiscent of the FTIR spectrum for the electronically excited ^{3}MLCT species generated in the photocycle of this catalyst, indicating that the carbonyl frequencies were indeed sensitive to the change in electron density. These results serve as groundwork for future 2DIR experiments to be performed on the labelled small peptide, and eventually larger *de novo* peptide systems, providing benchmark for comparisons of solvation dynamics on the bound rhenium to free rhenium in solution with similar distributions of electron density.

2.6 REFERENCES

1. Marcus, R. A. & Sutin, N. Electron transfers in chemistry and biology. *BBA Reviews On Bioenergetics* (1985). doi:10.1016/0304-4173(85)90014-X
2. Hamm, P. & Zanni, M. *Concepts and methods of 2D infrared spectroscopy*. *Concepts and Methods of 2D Infrared Spectroscopy* (2011). doi:10.1017/CBO9780511675935
3. Gray, H. B. & Winkler, J. R. Long-range electron transfer. *Proceedings of the National Academy of Sciences of the United States of America* (2005). doi:10.1073/pnas.0408029102
4. Gray, H. B. & Winkler, J. R. Electron tunneling through proteins. *Quarterly Reviews of Biophysics* (2003). doi:10.1017/S0033583503003913
5. Blanco-Rodríguez, A. M. *et al.* Phototriggering electron flow through ReI-modified pseudomonas aeruginosa azurins. *Chem. - A Eur. J.* (2011). doi:10.1002/chem.201002162
6. Winkler, J. R. & Gray, H. B. Electron Transfer in Ruthenium-Modified Proteins. *Chem. Rev.* (1992). doi:10.1021/cr00011a001
7. Vlček, A., Kvapilová, H., Towrie, M. & Záliš, S. Electron-Transfer Acceleration Investigated by Time Resolved Infrared Spectroscopy. *Acc. Chem. Res.* (2015). doi:10.1021/ar5004048
8. Takematsu, K. *et al.* Tryptophan-accelerated electron flow across a protein-protein interface. *J. Am. Chem. Soc.* (2013). doi:10.1021/ja406830d
9. Shih, C. *et al.* Tryptophan-accelerated electron flow through proteins. *Science (80-.).* (2008). doi:10.1126/science.1158241

10. Blanco-Rodríguez, A. M. *et al.* Excited-state dynamics of structurally characterized [Re I(CO)3(phen)(HisX)]+ (X = 83, 109) Pseudomonas aeruginosa azurins in aqueous solution. *J. Am. Chem. Soc.* (2006). doi:10.1021/ja057451+
11. Takematsu, K. *et al.* Two Tryptophans Are Better Than One in Accelerating Electron Flow through a Protein. *ACS Cent. Sci.* (2019). doi:10.1021/acscentsci.8b00882
12. Ross, M. R. *et al.* Histidine orientation modulates the structure and dynamics of a de novo metalloenzyme active site. *J. Am. Chem. Soc.* (2015). doi:10.1021/jacs.5b02840
13. Yu, F. *et al.* Protein design: Toward functional metalloenzymes. *Chemical Reviews* (2014). doi:10.1021/cr400458x
14. Yu, F., Penner-Hahn, J. E. & Pecoraro, V. L. De novo-designed metallopeptides with type 2 copper centers: Modulation of reduction potentials and nitrite reductase activities. *J. Am. Chem. Soc.* (2013). doi:10.1021/ja406648n
15. Zastrow, M. L. & Pecoraro, V. L. Influence of active site location on catalytic activity in de novo - designed zinc metalloenzymes. *J. Am. Chem. Soc.* (2013). doi:10.1021/ja401537t
16. Wang, L., Middleton, C. T., Zanni, M. T. & Skinner, J. L. Development and validation of transferable amide i vibrational frequency maps for peptides. *J. Phys. Chem. B* (2011). doi:10.1021/jp200745r
17. Lin, Y. S., Shorb, J. M., Mukherjee, P., Zanni, M. T. & Skinner, J. L. Empirical amide I vibrational frequency map: Application to 2D-IR line shapes for isotope-edited membrane peptide bundles. *J. Phys. Chem. B* (2009). doi:10.1021/jp807528q
18. Hamm, P., Lim, M. & Hochstrasser, R. M. Structure of the amide I band of peptides measured by femtosecond nonlinear-infrared spectroscopy. *J. Phys. Chem. B* (1998). doi:10.1021/jp9813286
19. Kim, Y. S. & Hochstrasser, R. M. Dynamics of amide-I modes of the alanine dipeptide in D 2O. *J. Phys. Chem. B* (2005). doi:10.1021/jp0449511
20. Rubtsov, I. V., Wang, J. & Hochstrasser, R. M. Vibrational coupling between amide-I and amide-A modes revealed by femtosecond two color infrared spectroscopy. *J. Phys. Chem. A* (2003). doi:10.1021/jp021922m
21. Baiz, C. R., Reppert, M. & Tokmakoff, A. An introduction to protein 2D IR spectroscopy. in *Ultrafast Infrared Vibrational Spectroscopy* (2013). doi:10.1201/b13972
22. Baiz, C. R. & Tokmakoff, A. Structural disorder of folded proteins: Isotope-edited 2D IR spectroscopy and markov state modeling. *Biophys. J.* (2015). doi:10.1016/j.bpj.2014.12.061
23. Hawecker, J., Lehn, J. M. & Ziessel, R. Electrocatalytic reduction of carbon dioxide mediated by Re(bipy)(CO) 3Cl (bipy = 2,2′-bipyridine). *J. Chem. Soc. Chem. Commun.* (1984). doi:10.1039/C39840000328
24. Cannizzo, A. *et al.* Femtosecond fluorescence and intersystem crossing in rhenium(I) carbonyl-bipyridine complexes. *J. Am. Chem. Soc.* **130**, 8967–8974 (2008).
25. Takeda, H., Koike, K., Inoue, H. & Ishitani, O. Development of an efficient photocatalytic system for CO2 reduction using rhenium(I) complexes based on mechanistic studies. *J. Am. Chem. Soc.* **130**, 2023–2031 (2008).
26. Machan, C. W., Sampson, M. D., Chabolla, S. A., Dang, T. & Kubiak, C. P. Developing a mechanistic understanding of molecular electrocatalysts for CO2 reduction using infrared spectroelectrochemistry. *Organometallics* **33**, 4550–4559 (2014).
27. Vollmer, M. V. *et al.* Synthesis, spectroscopy, and electrochemistry of (α-diimine)M(CO)3Br, M =

Mn, Re, complexes: Ligands isoelectronic to bipyridyl show differences in CO2 reduction. *Organometallics* **34**, 3–12 (2015).

28. Liard, D. J., Busby, M., Matousek, P., Towrie, M. & Vlček, A. Picosecond Relaxation of 3MLCT Excited States of [Re(Etpy)(Co)3(dmb)]+ and [Re(Cl)(Co)3(bpy)] as Revealed by Time-Resolved Resonance Raman, UV - vis, and IR Absorption Spectroscopy. *J. Phys. Chem. A* **108**, 2363–2369 (2004).
29. Johnson, F. P. A., George, M. W., Hartl, F. & Turner, J. J. Electrocatalytic reduction of CO2using the complexes [Re(bpy)(CO)3L]n(n = +1, L = P(OEt)3, CH3CN; n = 0, L = Cl-, Otf-; bpy = 2,2′-bipyridine; Otf-= CF3SO3) as catalyst precursors: Infrared spectroelectrochemical investigation. *Organometallics* **15**, 3374–3387 (1996).
30. Morris, A. J., Meyer, G. J. & Fujita, E. Molecular approaches to the photocatalytic reduction of carbon dioxide for solar fuels. *Acc. Chem. Res.* **42**, 1983–1994 (2009).
31. Smieja, J. M. & Kubiak, C. P. Re(bipy-tBu)(CO)3Cl-improved catalytic activity for reduction of carbon dioxide: IR-spectroelectrochemical and mechanistic studies. *Inorg. Chem.* **49**, 9283–9289 (2010).
32. Smieja, J. M. *et al.* Kinetic and structural studies, origins of selectivity, and interfacial charge transfer in the artificial photosynthesis of CO. *Proc. Natl. Acad. Sci. U. S. A.* **109**, 15646–15650 (2012).
33. Nahhas, A. El *et al.* Ultrafast excited-state dynamics of [Re(L)(CO)3(bpy)] n complexes: Involvement of the solvent. *J. Phys. Chem. A* **114**, 6361–6369 (2010).
34. Takeda, H., Koike, K., Morimoto, T., Inumaru, H. & Ishitani, O. *Photochemistry and photocatalysis of rhenium(I) diimine complexes*. *Advances in Inorganic Chemistry* **63**, (Elsevier Inc., 2011).
35. Sato, S. *et al.* Photochemistry of fac-[Re(bpy)(CO)3Cl]. *Chem. - A Eur. J.* **18**, 15722–15734 (2012).
36. Sato, S. *et al.* Photochemical ligand substitution reactions of fac-[Re(bpy)(CO) 3Cl] and derivatives. *Inorg. Chem.* **46**, 3531–3540 (2007).
37. Clark, M. L., Cheung, P. L., Lessio, M., Carter, E. A. & Kubiak, C. P. Kinetic and Mechanistic Effects of Bipyridine (bpy) Substituent, Labile Ligand, and Brønsted Acid on Electrocatalytic CO2 Reduction by Re(bpy) Complexes. *ACS Catal.* **8**, 2021–2029 (2018).
38. Kiefer, L. M., King, J. T. & Kubarych, K. J. Equilibrium excited state dynamics of a photoactivated catalyst measured with ultrafast transient 2DIR. *J. Phys. Chem. A* **118**, 9853–9860 (2014).
39. Kiefer, L. M. & Kubarych, K. J. Solvent-dependent dynamics of a series of rhenium photoactivated catalysts measured with Ultrafast 2DIR. *J. Phys. Chem. A* **119**, 959–965 (2015).
40. Nee, M. J., Baiz, C. R., Anna, J. M., McCanne, R. & Kubarych, K. J. Multilevel vibrational coherence transfer and wavepacket dynamics probed with multidimensional IR spectroscopy. *J. Chem. Phys.* **129**, (2008).
41. Hybl, J. D., Ferro, A. A. & Jonas, D. M. Two-dimensional Fourier transform electronic spectroscopy. *J. Chem. Phys.* **115**, 6606–6622 (2001).
42. Dlott, D. D. Vibrational energy redistribution in polyatomic liquids: 3D infrared-Raman spectroscopy. *Chem. Phys.* **266**, 149–166 (2001).
43. Anna, J. M., Baiz, C. R., Ross, M. R., Mccanne, R. & Kubarych, K. J. Ultrafast equilibrium and non-equilibrium chemical reaction dynamics probed with multidimensional infrared spectroscopy. *Int. Rev. Phys. Chem.* **31**, 367–419 (2012).
44. Hybl, J. D., Yu, A., Farrow, D. A. & Jonas, D. M. Polar solvation dynamics in the femtosecond evolution of two-dimensional Fourier transform spectra. *J. Phys. Chem. A* **106**, 7651–7654 (2002).

45. Osborne, D. G. & Kubarych, K. J. Rapid and accurate measurement of the frequency-frequency correlation function. *J. Phys. Chem. A* **117**, 5891–5898 (2013).
46. Roberts, S. T., Loparo, J. J. & Tokmakoff, A. Characterization of spectral diffusion from two-dimensional line shapes. *J. Chem. Phys.* **125**, (2006).
47. Eckert, P. A. & Kubarych, K. J. Oxidation-State-Dependent Vibrational Dynamics Probed with 2D-IR. *J. Phys. Chem. A* **121**, 2896–2902 (2017).
48. Worl, L. A., Duesing, R., Chen, P., Ciana, L. Della & Meyer, T. J. Photophysical properties of polypyridyl carbonyl complexes of rhenium(I). *J. Chem. Soc. Dalt. Trans.* 849–858 (1991). doi:10.1039/DT9910000849
49. Frisch, M. J. *et al.* Gaussian 09, Revision B.01. *Gaussian 09, Revision B.01, Gaussian, Inc., Wallingford CT* (2009).
50. Blanco-Rodríguez, A. M. *et al.* Photophysics of singlet and triplet intraligand excited states in [ReCl(CO)3(1-(2-pyridyl)-imidazo[1,5-α]pyridine)] complexes. *J. Am. Chem. Soc.* **136**, 5963–5973 (2014).
51. Maroncelli, M. Continuum estimates of rotational dielectric friction and polar solvation. *J. Chem. Phys.* **106**, 1545–1557 (1997).

Chapter 3 Ultrafast Two-Dimensional Infrared Spectroelectrochemical Measurements of Electrocatalyst Re(bpy)(CO)3Cl

3.1 INTRODUCTION

Spectroelectrochemistry combines electrochemical methods with spectroscopic techniques, allowing *in situ* spectroscopic monitoring of a system as it undergoes electrochemical processes. This technique has been successfully employed with a variety of spectroscopic methods, including NMR, Raman, UV-Vis, and infrared.[1–10] Combining the two methods gives greater insight into an electrocatalytic mechanism via identification and characterization of intermediates that occur during the oxidation or reduction. Recent work in this field has incorporated ultrafast spectroscopy into spectroelectrochemical experiments.[11–13] The appeal of ultrafast spectroscopy is the potential to observe electrochemical reactions in real time, leading to a more complete characterization of unstable intermediates and a window into how solvation dynamics are altered by changing the electronic structure of a molecule through electrochemical means, and the effect those alterations have on the mechanism.

Ultrafast vibrational spectroscopy is able to provide a window into vibrational dynamics of both the system of interest and its solvent or surroundings and its solvent or surroundings on a sub-picosecond timescale. Two-dimensional infrared spectroscopy (2DIR) in particular is a powerful tool for observing phenomena such as preferential solvation, structural dynamics, and vibrational energy transfer and relaxation. 2DIR offers a unique capacity to separate congested spectra, making it well-suited to resolve and identify intermediates generation during the electrochemical process – one of the driving goals behind spectroelectrochemical experiments. Additionally, given the large changes in

charge distribution invoked by changing the redox state of a molecule, the solvent molecules surrounding the redox system may interact differently with different oxidation states of the molecule, resulting in changes to vibrational lifetimes or spectral diffusion timescales that could be revealed using 2DIR.[14]

Previous work combining 2DIR and electrochemistry utilized geometries where the surface acts as both the electrode and as a reflective material.[12,13,15] Bredenbeck *et al* utilized a spectroelectrochemical cell designed to be used in a reflectance geometry, with both the gold working and counter electrode being deposited as a thin layer directly on the mirror used for the reflectance, reducing the problem of scattering. The reflectance geometry is ideal for redox systems such as proteins, where changes to the vibrational spectrum induced by the oxidation or reduction may be small, as the beams pass through the sample twice, doubling the signal size relative to a transmission geometry.[15] Using this cell design, they were able to compare the anharmonic coupling and vibrational energy transfer between the different vibrational modes in the oxidized and reduced state of the protein cofactor flavin mononucleotides.[13] Hamm *et al.* used 2DIR-SEC in an attenuated total reflectance geometry to measure CO adsorbed to a platinum or indium-tin oxide sputter-coated ATR prism, which again here serves as a crucial part of the ATR geometry and the working electrode. This allowed for measurements of the vibrational Stark-shift spectra of the adbsorbed CO group, as well as determination of spectral diffusion and vibrational relaxation timescales across different electrode potentials, which they found to have no dependence on the potential.[12] While they found no evidence of a relationship between applied potential and key 2DIR observables, Bredenbeck *et al* report seeing an indication of changes in spectral band shapes based on oxidation state in their flavin mononucleotide sample.[16]

While both of these methods creatively circumvent the problem of scattering, which has been a major roadblock to advances in combining coherent spectroscopy with electrochemistry, neither experimental design allows for use of

traditional transmission geometry in the way that is more analogous to the traditional linear IR spectroscopy method and both require the electrode to be included as part of the sample geometry. To perform similar *in situ* 2DIR spectroelectrochemical measurements in a transmission geometry, we implement an optically transparent thin-layer electrochemical cell (OTTLE cell)[17], where the working platinum mesh grid electrode has a few millimeter square aperture in the middle, allowing the IR beams to transmit through the region of the cell with the highest concentration of intermediates while avoiding interference from the electrode itself. This gives clean access to the electrochemical intermediates and provides a methodology for combining ultrafast spectroscopy with the geometry most commonly used in spectroelectrochemical experiments.

The Lehn catalyst, a rhenium containing CO_2 reduction catalyst, has been the subject of numerous studies across multiple disciplines of chemistry since its initial discovery. Major areas of focus of investigations of this catalytic system and its derivatives are optimization of the efficiency and determination of the possible mechanisms for the reduction of CO_2 to CO. Spectroelectrochemistry has played a major role in elucidating the electrocatalytic mechanism, revealing a solvent and ligand dependence for the reduction of the catalyst *fac*-Re(4,4'-R_2-bpy)$(CO)_3$X through FTIR and UV-Vis characterization of intermediate species.[18–36] Uniquely, the *fac*-Re(4,4'-R_2-bpy)$(CO)_3$X catalyst can act as both a photo- and electrocatalyst for CO_2 reduction. Previously, we took advantage of the long excited state lifetime of the ^{3}MLCT state formed in the initiation of the photocycle and performed transient 2D-IR experiments, where a UV or visible pump pulse precedes the standard 2D-IR sequence, on the equilibrium excited state of *fac*-Re(bpy)$(CO)_3$Cl (ReCl).[37] We observed differences in the dynamics of the ^{3}MLCT state relative to the ground state, which we attributed to multiple factors including solvent friction and the modified electronic structure of the catalyst. To further investigate this effect we conducted a series of 2D-IR experiments on modified versions of the ReCl catalyst, substituting electron-withdrawing or -donating

ligands onto the bipyridine moiety and conducting the experiments over a range of solvents.[38] The substitutions on the diimine ligand did not result in any appreciable change in the dynamics, however we did observe a dependence on the solvent donicity, a metric used to describe the nucleophilicity of the solvent.[39]

To further probe the relationship between electronic structure or oxidation state and dynamics, we studied a different transition metal complex where we could access two difference oxidation states through chemical means. This complex, [1,1'-bis(diphenylphosphino)ferrocene]tetracarbonyl chromium (DPPFCr), exhibited significant oxidation state impacts on intramolecular dynamical processes, such as vibrational relaxation and redistribution, however there was no observable effect of the change in oxidation state on the spectral diffusion, a primarily intermolecular process.[40] We speculated that the donicty of the solvent was masking the effect of the change in dipole moment on the dynamics, similar to the observation from the series of modified rhenium catalysts. Hamm et al saw similar behavior when varying the electrochemical potential and monitoring CO adhered to a metal surface, where they observed potential-dependent frequency shifts but no change in spectral diffusion.[12]

While all of these approaches give insight into the effects of changes in the electronic structure of a molecule, they each have their limitations. In the case of the ReCl catalyst, we were only able to compare a long-lived excited triplet neutral species to its ground state, and not while it is progressing through its catalytic cycle. While this certainly represents a change in the dipole moment of the ReCl, it does not give us a clear picture of how the reduced form of this catalyst may differ from its original state. In our DPPFCr experiments, were limited to studying species where we could synthesize the molecule in two different oxidation states, and to solvents with a low donor number, so that the donicity effect would not overshadow the effect from the change in oxidation state. In this work, we build upon both our knowledge of the dynamical behavior of both the ground and triplet excited state of ReCl as well as the previously

proposed spectroelectrochemically determined mechanisms to perform the first ultrafast 2DIR measurements on this molecule *in situ* during its electrocatalytic reduction.

3.2 EXPERIMENTAL METHODS

3.2.1 Equilibrium 2DIR Spectroscopy

We generate infrared light by using 800 nm pulses from a regenerative amplifier to pump to independent optical parametric amplifiers (OPAs). The light generated in the OPAs drives two separate AgGaS difference-frequency-generating (DFG) crystals, giving ~2000 cm^{-1} (125 cm^{-1} fwhm) infrared light. This light is split into multiple beams. Two field interactions excite the molecule into a vibrationally excited state, one is used to probe the sample, and another is used as a local oscillator to interfere with the emitted signal to allow for heterodyne detection using spectral interferometry. The beams are used in a noncollinear box geometry, giving the emitted signal in a background-free detection. For each waiting time delay (t_2) between the pump pulses and the probe pulse, we perform a rephasing and non-rephasing experiment. The phase matching conditions for the two signals are as follows: rephasing: $\boldsymbol{k_r = -k_1 + k_2 + k_3}$, and non-rephasing: $\boldsymbol{k_n = +k_1 - k_2 + k_3}$**.** We continuously scan the time delay (t_1) between the pump pulses using a pair of ZnSe wedges in each pump pulse path and record the signal on a shot-by-shot basis synchronized to the laser at 1 kHz. One pair of rephasing and non-rephasing spectra takes roughly 30 seconds, so that a full waiting time scan can be recorded in under an hour. We Fourier transform the signal with respect to t_1 in order to obtain the excitation axis. The detection frequency axis is obtained directly by the Fourier transformation performed by the spectrometer, and the mid-IR signal and local oscillator are measured in the visible using a CCD in combination with chirped pulse upconversion.[41]

3.2.2 Sample Preparation

$Re(bpy)(CO)_3Cl$ was synthesized according to published methods.[42] Anhydrous THF and tetrabutylammonium hexafluorophosphate ($TBAPF_6$) were obtained from Sigma Aldrich and used as received.

An IR optically transparent thin-layer electrode (OTTLE) cell[17] equipped with Pt-minigrid working and auxiliary electrodes and a Ag-wire pseudoreference electrode was employed for the spectroelectrochemical measurements. 2-mm thick CaF_2 windows were used for all spectroelectrochemical measurements. Cyclic voltammetry and controlled potential amperometry within the OTTLE cell were carried out using a PalmSens EmStat3 potentiostat and the corresponding software. FTIR-SEC spectra were measured using a JASCO 4100 spectrometer. For spectroelectrochemical experiments, the concentration of $Re(bpy)(CO)_3Cl$ was 10 mM, and the concentration of the electrolyte $TBAPF_6$ was 0.1M in THF. All spectroelectrochemical samples were prepared in a dry glovebox under an inert atmosphere.

3.3 RESULTS

3.3.1 Linear FTIR Measurements

The mechanism for the electrocatalytic reduction of $Re(bpy)(CO)_3Cl$ (ReCl) in THF as previously proposed can be seen in **Figure 3.1**.[19] Upon addition of the first electron, an anionic species forms (**2**) which then can lose the chloride ion, forming species **3**. The molecule then either forms a Re-Re dimer (**4**) or undergoes a second reduction to species **6**. The dimer species can also undergo reduction, resulting in the anionic dimer (**5**) followed by species **6**.

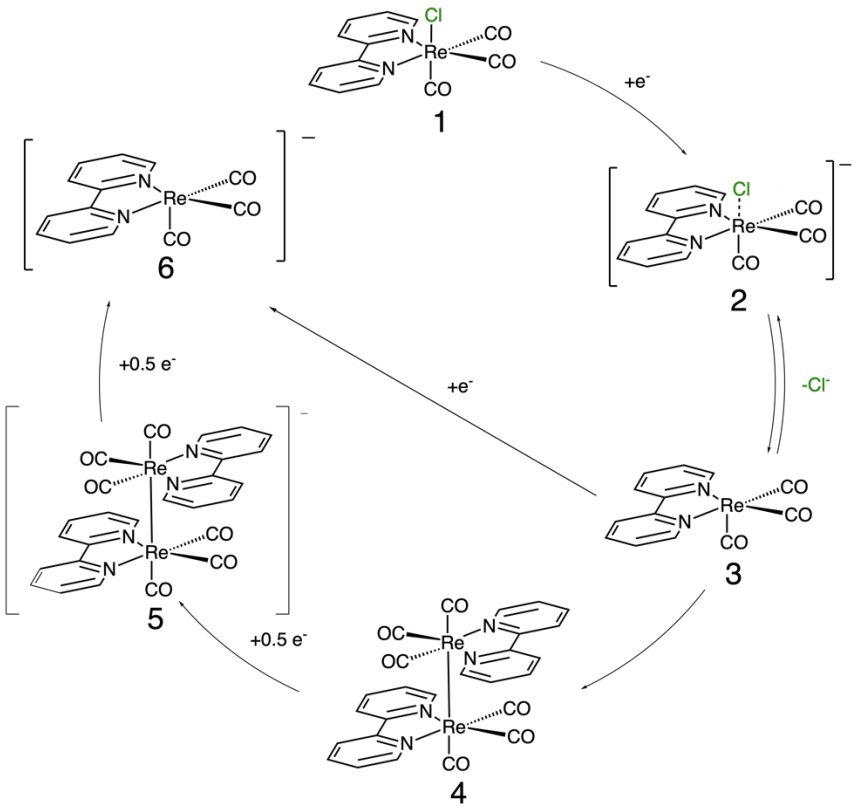

Figure 3.1 Proposed mechanism of the ReCl electrocatalytic reduction cycle in THF, showing formation of the singly reduced rhenium species (2) and the Re-Re dimer (4).

The conditions needed to perform both the spectroscopic and electrochemical halves of the experiment successfully necessitate specially designed electrochemical cells. One example of such a cell is the optically transparent thin layer electrochemical (OTTLE) cell, which has been employed successfully in many previously spectroelectrochemical experiments. The design of the OTTLE cell used for our 2DIR-SEC experiments is shown in **Figure 3.2**. Unlike previous OTTLE cell designs, the cell used for these experiments utilizes thin CaF_2 windows (2 mm). For all linear and 2DIR-SEC measurements reported here the signal beam was sent through the square aperture cut into the working Pt grid electrode.

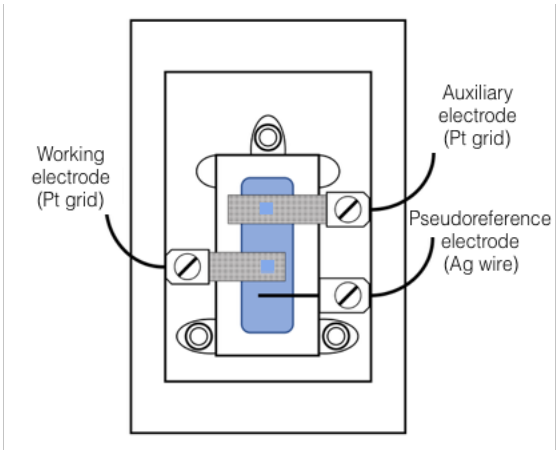

Figure 3.2 Schematic of a top-down view of the OTTLE cell used in our measurements.

Figure 3.3 illustrates the results of our linear FTIR-SEC measurements using the thin window OTTLE cell. The characteristic carbonyl peaks from the unreduced ReCl in THF are seen at 2019, 1917, and 1894 cm^{-1}, in accordance with the literature. As the voltage is stepped downward, peaks assigned to the singly reduced species (**2**) begin to grow in at 1996, 1883, and 1868 cm^{-1}. As the voltage is further decreased, signatures from the dimer species (**4**) distinctly appear at 1986 and 1950 cm^{-1}. There is evidence of the lower frequency modes of the dimer at 188 and 1857 cm^{-1}, however it becomes difficult to distinctly separate the peaks in that region given the overlap with the lower frequency modes of the singly and doubly reduced species. The doubly reduced species (**6**) shows up at 1947 cm^{-1} with a second broad absorption at 1843 cm^{-1}, clearly seen in the dark purple spectra of **Figure 3.3A**.

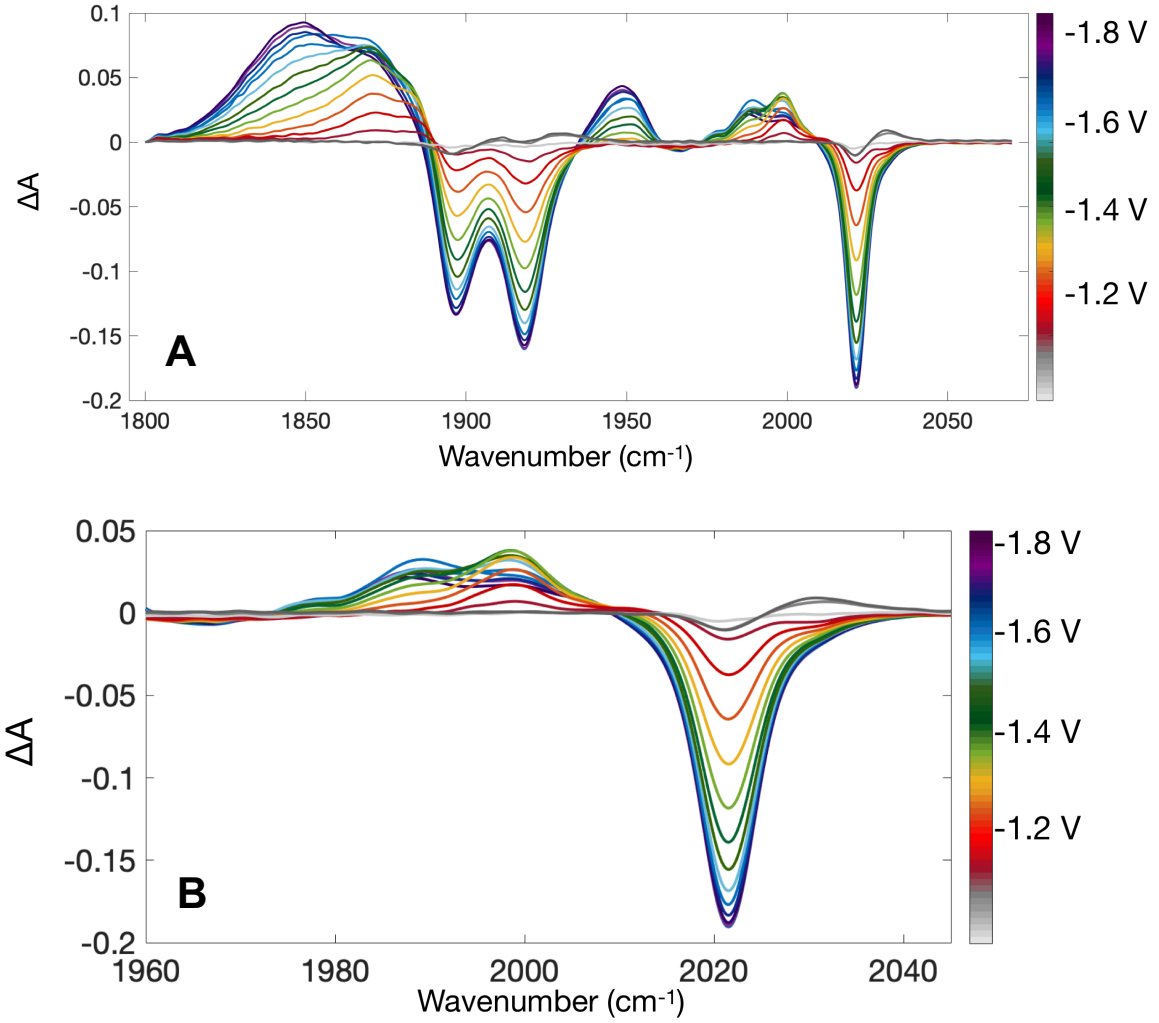

Figure 3.3 A) Full FTIR difference absorption spectrum of ReCl in THF with 0.1 M TBAPF6 over a voltage range of -0.5 to -1.8 V. Difference is between 0 V and voltage shown on the right Y axis. B) Zoomed in FTIR spectrum highlighting the high frequency modes of ReCl (2019 cm^{-1}), singly reduced ReCl (1996 cm^{-1}), and the Re-Re dimer (1986 cm^{-1}).

3.3.2 2DIR Measurements

To reduce scatter in the 2D-IR spectrum during spectroelectrochemical experiments, we instituted quasi-phase-cycling into our experiments.[43] A wobbling ZnSe Brewster window was placed into one of our pump beams to alter the optical path and introduce a sub-cycle pulse delay, which allows us to remove scattering while only minimally impacting our signal. Example non-rephasing spectra of ReCl in THF with 0.1 M $TBAPF_6$ showing the effect with and without the wobbler can be seen in **Figure 3.4**.

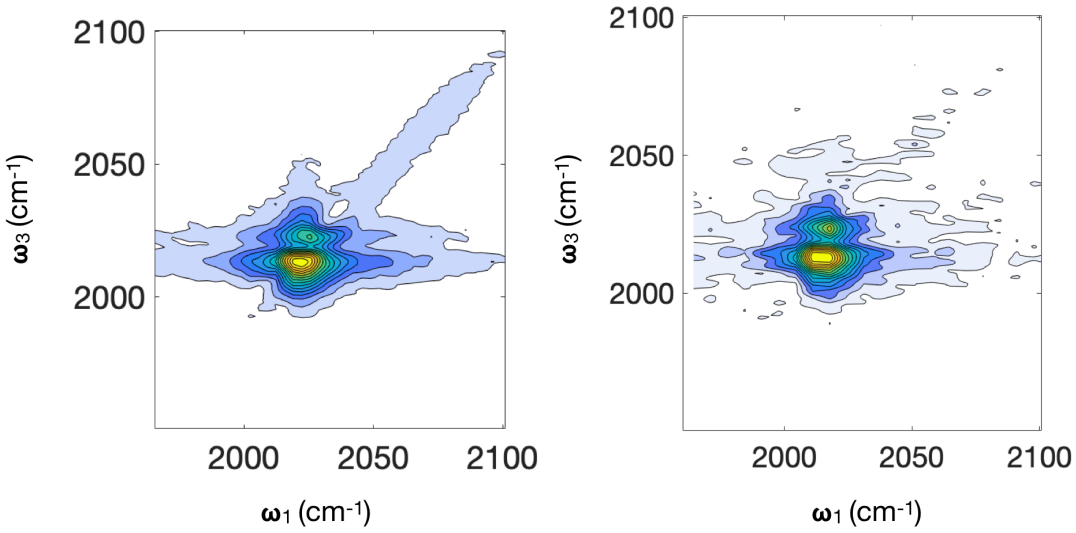

Figure 3.4 2DIR spectra of ReCl in THF and 0.1 M TBAPF6 taken without the use of phase wobbler (left) and with the wobbler engaged (right) illustrating the reduction of scatter without major expense to the signal.

For the 2DIR-SEC measurements, we focused on comparing the high frequency mode of the unreacted rhenium (2019 cm^{-1}) and the same mode in the singly reduced and dimeric species. We see a minor slowdown in the spectral diffusion timescale when comparing the ReCl molecule in pure THF to the molecule in THF with 0.1 M $TBAPF_6$. The presence of the electrolyte increases our observed spectral diffusion timescale from 1.5 ps in the pure solvent to 2.5 ps in the electrolyte solution.[38] The fits for the spectral diffusion can be seen in Figure 3.4.

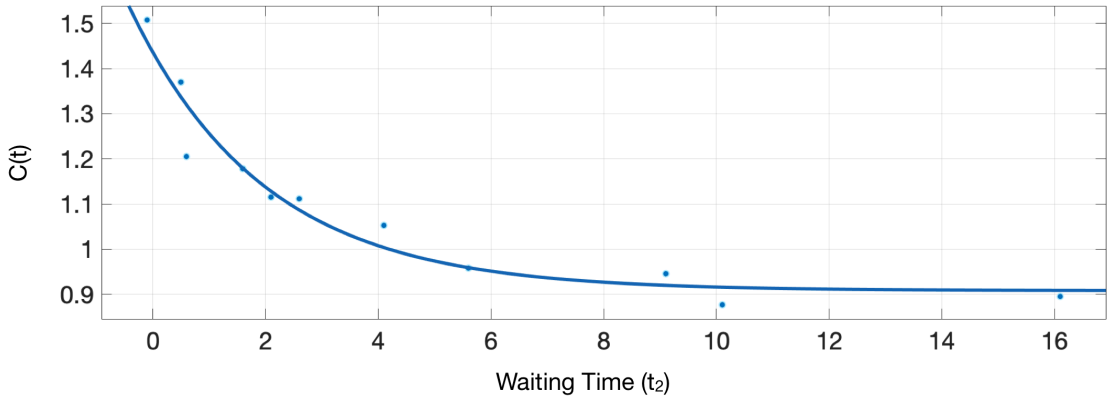

Figure 3.5 FFCF showing spectral diffusion timescale of ReCl with 0.1 M $TBAPF_6$ in THF.

The first reduction of the rhenium red shifts the frequency to 1996 cm^{-1}, as seen in **Figure 3.3**. We began by taking a series of "snapshots" of the system at

different waiting times ranging from 100 fs to 10 ps as the voltage was incrementally stepped down. “Snapshot” non-rephasing 2DIR spectra at 0 V and -1.7 V are seen in **Figure 3.6**. Here, you can see both the initial production of the reduced rhenium at ~1996 cm^{-1} and the eventual formation of the Re-Re dimer as evidenced by a peak at 1986 cm^{-1}. As proposed by Fujita et al, over time (~1h) the reduced rhenium couples into the dimer.[33]

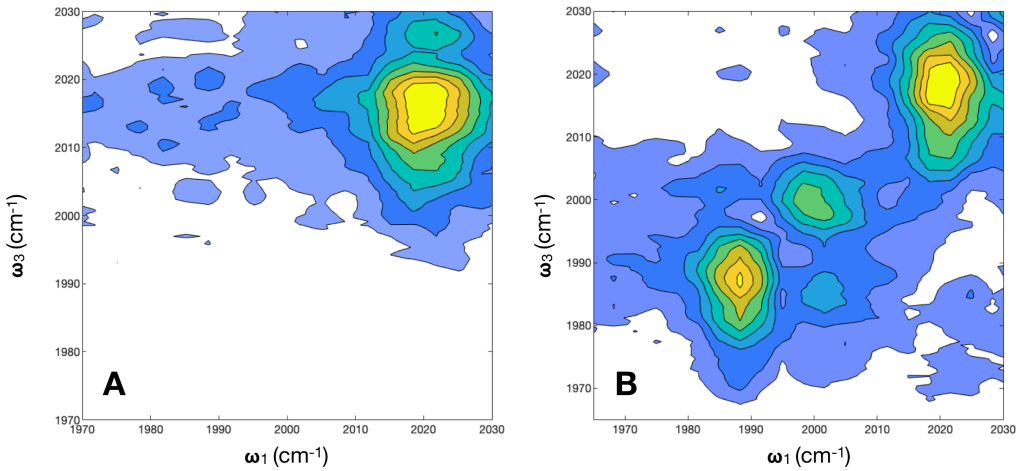

Figure 3.6 Snapshot at 0.5 ps non-rephasing 2DIR spectra showing evolution of the singly reduced ReCl species (1996 cm^{-1}) and Re-Re dimer (1986 cm^{-1}) peaks, as the voltage was increased from 0 V (A) to -1.7 V (B).

Performing DFT calculations, we found the dipole moment of the singly reduced species to be 7.9 D, a significant decrease from our calculated ground state permanent dipole moment of 14.1 D, but larger than our calculated dipole moment for the ^{3}MLCT state of ReCl of 5.8 D.[37] In that work, we found the solvation dynamics of the ^{3}MLCT state to exhibit a 3-fold slowdown relative to that of the ground state, which was attributed in part to the change in dielectric friction caused by coupling of the molecular dipole moment to the dielectric medium of the solvent.[37] We also observe a near order of magnitude decrease in the vibrational lifetime, decreasing from 25 ps in the ground state in THF to 3.2 ps in the excited state.[37] Preliminary measurements on the reduced species in THF yields a vibrational lifetime of ~18 ps, a slowdown relative to that in the ground state yet not nearly as sharp of a decrease as seen in the ^{3}MLCT state. Further analysis is needed to determine spectral diffusion and vibrational energy transfer timescales.

3.4 CONCLUSIONS

We present here the first *in situ* 2DIR-SEC measurements performed on the CO_2 reduction electrocatalyst $Re(bpy)(CO)_3Cl$. Utilizing an optically transparent thin layer electrochemical (OTTLE) cell with apertures cut into Pt mesh working and counter electrodes, we were able to reveal for the first time the 2D-IR signatures of the reduced ReCl and Re-Re dimer that have previously been proposed as key intermediates in the reduction of this electrocatalyst in THF.[18,19] Measurements were taken in a transmission geometry in a method analogous to common spectroelectrochemical cell designs, as opposed to previous 2DIR-SEC measurements, which utilized external reflectance or ATR geometries and required specially designed electrochemical cells. Preliminary results on the reduced species indicate a minor decrease in the vibrational lifetime of the high frequency A'(1) carbonyl stretching mode, however further analysis is needed to pull out additional information about the relationship between changes in the solvent dynamics and oxidation state.

3.5 REFERENCES

1. Scherson, D. A., Tolmachev, Y. V. & Stefan, I. C. *Ultraviolet/Visible Spectroelectrochemistry*. *Encyclopedia of Analytical Chemistry* (2006). doi:10.1002/9780470027318.a5316
2. Lozeman, J. J. A., Führer, P., Olthuis, W. & Odijk, M. Spectroelectrochemistry, the future of visualizing electrode processes by hyphenating electrochemistry with spectroscopic techniques. *Analyst* (2020). doi:10.1039/c9an02105a
3. Klod, S., Ziegs, F. & Dunsch, L. In situ NMR spectroelectrochemistry of higher sensitivity by large scale electrodes. *Anal. Chem.* (2009). doi:10.1021/ac901641m
4. Ibañez, D., Garoz-Ruiz, J., Heras, A. & Colina, A. Simultaneous UV-visible absorption and Raman spectroelectrochemistry. *Anal. Chem.* (2016). doi:10.1021/acs.analchem.6b02008
5. Jeanmaire, D. L. & Van Duyne, R. P. Surface raman spectroelectrochemistry. *J. Electroanal. Chem. Interfacial Electrochem.* (1977). doi:10.1016/s0022-0728(77)80224-6
6. Ashley, K. Solution infrared spectroelectrochemistry: A review. *Talanta* (1991). doi:10.1016/0039-9140(91)80094-G
7. Zhai, Y., Zhu, Z., Zhou, S., Zhu, C. & Dong, S. Recent advances in spectroelectrochemistry. *Nanoscale* (2018). doi:10.1039/c7nr07803j
8. Dunsch, L. Recent Advances in in situ multi-spectroelectrochemistry. *Journal of Solid State Electrochemistry* (2011). doi:10.1007/s10008-011-1453-1
9. Kaim, W. & Fiedler, J. Spectroelectrochemistry: The best of two worlds. *Chemical Society Reviews*

(2009). doi:10.1039/b504286k

10. Boisseau, R., Bussy, U., Giraudeau, P. & Boujtita, M. In situ ultrafast 2D NMR spectroelectrochemistry for real-time monitoring of redox reactions. *Anal. Chem.* **87**, 372–375 (2015).
11. Kraack, J. P. & Hamm, P. Surface-Sensitive and Surface-Specific Ultrafast Two-Dimensional Vibrational Spectroscopy. *Chem. Rev.* **117**, 10623–10664 (2017).
12. Lotti, D., Hamm, P. & Kraack, J. P. Surface-Sensitive Spectro-electrochemistry Using Ultrafast 2D ATR IR Spectroscopy. *J. Phys. Chem. C* **120**, 2883–2892 (2016).
13. El Khoury, Y., Van Wilderen, L. J. G. W. & Bredenbeck, J. Ultrafast 2D-IR spectroelectrochemistry of flavin mononucleotide. *J. Chem. Phys.* **142**, (2015).
14. Yu, P., Yang, F., Zhao, J. & Wang, J. Hydration dynamics of cyanoferrate anions examined by ultrafast infrared spectroscopy. *J. Phys. Chem. B* **118**, 3104–3114 (2014).
15. El Khoury, Y., van wilderen, L. J. G. W., Vogt, T., Winter, E. & Bredenbeck, J. A spectroelectrochemical cell for ultrafast two-dimensional infrared spectroscopy. *Rev. Sci. Instrum.* (2015). doi:10.1063/1.4927533
16. El Khoury, Y., Van Wilderen, L. J. G. W. & Bredenbeck, J. Ultrafast 2D-IR spectroelectrochemistry of flavin mononucleotide. *J. Chem. Phys.* (2015). doi:10.1063/1.4916916
17. Krejčik, M., Daněk, M. & Hartl, F. Simple construction of an infrared optically transparent thin-layer electrochemical cell. Applications to the redox reactions of ferrocene, Mn2(CO)10 and Mn(CO)3(3,5-di-t-butyl-catecholate)-. *J. Electroanal. Chem.* (1991). doi:10.1016/0022-0728(91)85012-E
18. Johnson, F. P. A., George, M. W., Hartl, F. & Turner, J. J. Electrocatalytic reduction of CO2using the complexes [Re(bpy)(CO)3L]n(n = +1, L = P(OEt)3, CH3CN; n = 0, L = Cl-, Otf-; bpy = 2,2′-bipyridine; Otf-= CF3SO3) as catalyst precursors: Infrared spectroelectrochemical investigation. *Organometallics* **15**, 3374–3387 (1996).
19. Stor, G. J., Hartl, F., Van Outersterp, J. W. M. & Stufkens, D. J. Spectroelectrochemical (IR, UV/Vis) Determination of the Reduction Pathways for a Series of [Re(CO)3(α-diimine)L']0/+ (L' = Halide, Otf-THF, MeCN, n-PrCN, PPh3, P(OMe)3) Complexes. *Organometallics* **14**, 1115–1131 (1995).
20. Czerwieniec, R., Kapturkiewicz, A., Lipkowski, J. & Nowacki, J. Re(I)(tricarbonyl)+ complexes with the 2-(2-pyridyl)-N-methyl- benzimidazole, 2-(2-pyridyl)benzoxazole and 2-(2-pyridyl)benzothiazole ligands - Syntheses, structures, electrochemical and spectroscopic studies. *Inorganica Chim. Acta* (2005). doi:10.1016/j.ica.2005.03.013
21. Andrade, G. A., Pistner, A. J., Yap, G. P. A., Lutterman, D. A. & Rosenthal, J. Photocatalytic conversion of CO2 to CO using rhenium bipyridine platforms containing ancillary phenyl or BODIPY moieties. *ACS Catal.* (2013). doi:10.1021/cs400332y
22. Paolucci, F. *et al.* Dynamics of the electrochemical behavior of diimine tricarbonyl rhenium(I) complexes in strictly aprotic media. *J. Phys. Chem. B* (1998). doi:10.1021/jp980659f
23. Portenkirchner, E. *et al.* Using the Alkynyl-Substituted Rhenium(I) Complex (4,4′-Bisphenyl-Ethynyl-2,2′-Bipyridyl)Re(CO)3Cl as Catalyst for CO2 Reduction—Synthesis, Characterization, and Application. *Electrocatalysis* (2015). doi:10.1007/s12678-014-0230-1
24. Clark, M. L., Cheung, P. L., Lessio, M., Carter, E. A. & Kubiak, C. P. Kinetic and Mechanistic Effects of Bipyridine (bpy) Substituent, Labile Ligand, and Brønsted Acid on Electrocatalytic CO2 Reduction by Re(bpy) Complexes. *ACS Catal.* **8**, 2021–2029 (2018).

25. Wong, K. Y., Chung, W. H. & Lau, C. P. The effect of weak Brönsted acids on the electrocatalytic reduction of carbon dioxide by a rhenium tricarbonyl bipyridyl complex. *J. Electroanal. Chem.* (1998). doi:10.1016/S0022-0728(98)00116-8
26. Machan, C. W., Yin, J., Chabolla, S. A., Gilson, M. K. & Kubiak, C. P. Improving the Efficiency and Activity of Electrocatalysts for the Reduction of CO2 through Supramolecular Assembly with Amino Acid-Modified Ligands. *J. Am. Chem. Soc.* (2016). doi:10.1021/jacs.6b03774
27. Wilting, A., Stolper, T., Mata, R. A. & Siewert, I. Dinuclear Rhenium Complex with a Proton Responsive Ligand as a Redox Catalyst for the Electrochemical CO2 Reduction. *Inorg. Chem.* (2017). doi:10.1021/acs.inorgchem.7b00178
28. Manbeck, G. F., Muckerman, J. T., Szalda, D. J., Himeda, Y. & Fujita, E. Push or Pull? Proton Responsive Ligand Effects in Rhenium Tricarbonyl CO2 Reduction Catalysts. *J. Phys. Chem. B* (2015). doi:10.1021/jp511131x
29. Smieja, J. M. & Kubiak, C. P. Re(bipy-tBu)(CO)3Cl-improved catalytic activity for reduction of carbon dioxide: IR-spectroelectrochemical and mechanistic studies. *Inorg. Chem.* **49**, 9283–9289 (2010).
30. Riplinger, C., Sampson, M. D., Ritzmann, A. M., Kubiak, C. P. & Carter, E. A. Mechanistic contrasts between manganese and rhenium bipyridine electrocatalysts for the reduction of carbon dioxide. *J. Am. Chem. Soc.* **136**, 16285–16298 (2014).
31. Machan, C. W., Sampson, M. D., Chabolla, S. A., Dang, T. & Kubiak, C. P. Developing a mechanistic understanding of molecular electrocatalysts for CO2 reduction using infrared spectroelectrochemistry. *Organometallics* **33**, 4550–4559 (2014).
32. Vollmer, M. V. *et al.* Synthesis, spectroscopy, and electrochemistry of (α-diimine)M(CO)3Br, M = Mn, Re, complexes: Ligands isoelectronic to bipyridyl show differences in CO2 reduction. *Organometallics* **34**, 3–12 (2015).
33. Fujita, E. & Muckerman, J. T. Why is Re-Re bond formation/cleavage in [Re(bpy)(CO)3] 2 different from that in [Re(CO)5]2? Experimental and theoretical studies on the dimers and fragments. *Inorg. Chem.* **43**, 7636–7647 (2004).
34. Hayashi, Y., Kita, S., Brunschwig, B. S. & Fujita, E. Involvement of a binuclear species with the Re-C(O)O-Re moiety in CO 2 reduction catalyzed by tricarbonyl rhenium(I) complexes with diimine ligands: Strikingly slow formation of the Re-Re and Re-C(O)O-re species from Re(dmb)(CO)3S (dmb = 4,4′-dimethyl-2,2′-bipyridine, S = solvent). *J. Am. Chem. Soc.* **125**, 11976–11987 (2003).
35. Du, J. P. & Siewert, I. An Electrochemical and Spectroscopic Study on Re(CO)3(L)Cl in Dimethylformamide (L = 2,2'-Bipyridine). *Zeitschrift fur Anorg. und Allg. Chemie* **3**, 1–8 (2020).
36. Teesdale, J. J. *et al.* Reduction of CO2 using a rhenium bipyridine complex containing ancillary BODIPY moieties. *Catal. Today* (2014). doi:10.1016/j.cattod.2013.10.091
37. Kiefer, L. M., King, J. T. & Kubarych, K. J. Equilibrium excited state dynamics of a photoactivated catalyst measured with ultrafast transient 2DIR. *J. Phys. Chem. A* **118**, 9853–9860 (2014).
38. Kiefer, L. M. & Kubarych, K. J. Solvent-dependent dynamics of a series of rhenium photoactivated catalysts measured with Ultrafast 2DIR. *J. Phys. Chem. A* **119**, 959–965 (2015).
39. Gutmann, V. Solvent effects on the reactivities of organometallic compounds. *Coord. Chem. Rev.* (1976). doi:10.1016/S0010-8545(00)82045-7
40. Eckert, P. A. & Kubarych, K. J. Oxidation-State-Dependent Vibrational Dynamics Probed with 2D-IR. *J. Phys. Chem. A* **121**, 2896–2902 (2017).

41. Nee, M. J., McCanne, R., Kubarych, K. J. & Joffre, M. Two-dimensional infrared spectroscopy detected by chirped pulse upconversion. *Opt. Lett.* (2007). doi:10.1364/ol.32.000713

42. Worl, L. A., Duesing, R., Chen, P., Ciana, L. Della & Meyer, T. J. Photophysical properties of polypyridyl carbonyl complexes of rhenium(I). *J. Chem. Soc. Dalt. Trans.* 849–858 (1991). doi:10.1039/DT9910000849

43. Bloem, R., Garrett-Roe, S., Strzalka, H., Hamm, P. & Donaldson, P. Enhancing signal detection and completely eliminating scattering using quasi-phase-cycling in 2D IR experiments. *Opt. Express* **18**, 27067 (2010).

Chapter 4 X-ray Absorption Spectroscopy of Methylcobalamin

The work in this chapter has been published in the following paper:
Michocki, Lindsay B.; Miller, N. A.; Alonso-Mori, R.; Britz, A.; Deb, A.; Glownia, J. M.; Kaneshiro, A.K.; Konar, a.; Meadows, J. H.; Sofferman, D. L.; Song, S.; Toda, M. J.; van Driel, T. B.; Kozlowski, P. M.; Kubarych, K. J.; Penner-Hahn, J. E.; Sension, R. J.; Probing the Excited State of Methylcobalamin Using Polarized Time-Resolved X-ray Absorption Spectroscopy. *The Journal of Physical Chemistry B* **2019,** *123*, 6042-6048.

4.1 INTRODUCTION

Photoactivated cobalamins (Cbls) provide the opportunity to exert spatial and temporal control over such varied outcomes as radical formation,[1] drug-delivery,[2,3] gene activation,[4–7] and B_{12} bioavailability.[8,9] Photo-induced bond cleavage is central to both the engineered and the natural biological exploitation of cobalamin photochemistry. Ultrafast time-resolved x-ray spectroscopy with x-ray free-electron lasers (XFELs) provides the opportunity to probe structural changes in short-lived states of molecular systems at room temperature and in complex environments without the radiation damage due to radical diffusion, characteristic of synchrotron source measurements. X-ray absorption near-edge structure (XANES) and the K-edge of 3d transition metals has proved a particularly sensitive method for identifying changes in bonding and oxidation state upon optical excitation.[10–17] Exploiting the relative polarization of optical and x-ray pulses permits the unique identification of structural changes along and perpendicular to the transition dipole excited by the optical pulse. We have previously applied this method to the study of excited state dynamics in vitamin B_{12} (cyanocobalamin CNCbl).[11,12]

A recent picosecond time-resolved XANES measurement of methylcobalamin (MeCbl, **Figure 4.1**) was reported using 400 nm excitation. Based on these data, Subramanian et al. suggest the Co-C bond undergoes substantial bond elongation in the excited state.[14] In contrast, recent theoretical simulations[18–20] and inferences based on the measured excited state absorption spectrum[21–23] suggest that the axial bond changes between the ground and excited state of MeCbl are small, with a contraction of the lower bond and a modest expansion of the upper bond. One of the challenges in interpreting spectra following 400 nm excitation is the fact, as shown in previous transient absorption measurements, that 400 nm excitation produces an excited state population that branches between two channels: a prompt dissociation channel with a quantum yield of ca. 0.25 and formation of a long-lived excited state with a quantum yield of ca. 0.75.[24] Thus, interpretation of the structural changes in the MeCbl excited state following 400 nm excitation requires separation of the contributions from the two different products that are present in the sample. Given the significant structural changes that photodissociation produces, it is possible that the MeCbl XANES difference spectrum following 400 nm excitation could be dominated by the formation of cob(II)alamin, potentially obscuring the identification of structural changes in the excited state.

Here we report a study of the excited state of MeCbl following excitation in the visible absorption band at 520 nm where the quantum yield for formation of the excited state approaches unity.[22,24] A complementary measurement on 5'-deoxyadenosylcobalamin (coenzyme B_{12}, AdoCbl) is used to characterize the cob(II)alamin product that forms in nearly quantum yield following photolysis of AdoCbl. Polarization is used to separate the *x* and *y*+*z* contributions to the XANES difference spectrum (**Figure 4.1**). In addition, both 540 nm and 365 nm excitation pulses are used to photolyze AdoCbl allowing separation of the *x, y,* and *z* contributions to the XANES difference spectrum for formation of cob(II)alamin.

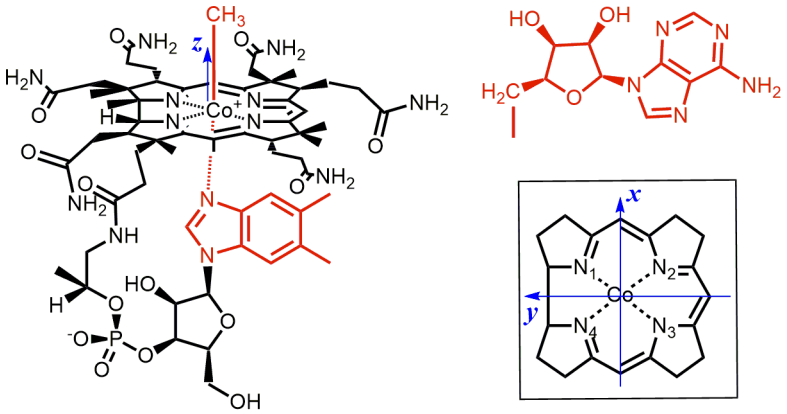

Figure 4.1 Schematic structure of MeCbl indicating the directions assigned as x, y, and z. The numbering system for the ring nitrogens (inset) assumes that upper ligand is above the plane of the figure. The lower axial ligand is the nitrogen from dimethylbenzimidazole (N_{DMB}). The upper axial ligand is methyl. For AdoCbl, the methyl group is replaced by a 5'-deoxyadenosyl group, shown in the upper right.

Quantitative comparison of the MeCbl excited state XANES spectrum with simulations and the decomposition of the difference spectrum into components polarized along or perpendicular to *x* as defined in **Figure 4.1** permit assignment of the structural changes in the excited state. Our measurements eliminate the ambiguity in assignment of features in the XANES spectrum to the MeCbl excited state or to cob(II)alamin. In agreement with the previous report, we find an expansion of the corrin ring in the excited state. However, we do not find evidence for significant elongation of the Co-C bond in the excited state. The difference between the ground and excited state structure is dominated by changes in the corrin ring. In contrast, the XANES difference spectrum following photodissociation of AdoCbl to form cob(II)alamin is dominated by the *z*-polarized component, reflecting loss of the upper axial ligand. Ultrafast XANES will prove a powerful tool for monitoring excited state structural dynamics of a wide range of important photoactive compounds.

4.2 EXPERIMENTAL METHODS

Time-resolved polarized XANES measurements were performed using the XPP instrument of the x-ray free electron laser LCLS at SLAC.[25] Samples of MeCbl and AdoCbl were dissolved in ultrapure deionized water to a concentration of ca. 5 mM and pumped through a glass nozzle to achieve a stable 50 μm diameter jet of solution. The x-ray beam and laser beam travel in a nearly collinear geometry

(~1° crossing angle) intersecting the sample stream several hundred μm below the nozzle. The polarization of the optical laser was rotation between horizontal (parallel to the x-ray polarization) and vertical (perpendicular to the x-ray polarization) using a remote-controlled half-wave plate. Finite-Difference Method Near Edge Structure (FDMNES) simulations of MeCbl were performed as described previously.[11,12]

4.3 RESULTS AND DISCUSSION

4.3.1 Time-resolved Polarized XANES

Time-resolved polarized XANES measurements were performed using the XPP instrument of the x-ray free electron laser LCLS at SLAC.[25] Measurements on MeCbl were performed using 520 nm optical excitation with the x-ray probe delayed by 100 ps. Measurements on AdoCbl were performed using 540 nm optical excitation with the x-ray probe delayed by 250 ps or 450 ps and 365 nm optical excitation with the x-ray probe delayed by 250 ps. The excited state lifetime of AdoCbl in water is ca. 100 ps. Using lifetimes determined previously from UV-visible transient absorption measurements, the difference spectrum of AdoCbl at 250 ps corresponds to 85% cob(II) and 15% excited state. At 450 ps, the populations are 97% cob(II) and 3% excited state.[26,27]

Decomposition of the x-ray transient difference signal is achieved using the formalism developed for optical absorption and presented previously for CNCbl.[1] The 1s → np K-edge x-ray transition can be decomposed into any set of orthogonal molecule-fixed Cartesian coordinates. The obvious choice is $\vec{a}$ parallel to the transition dipole initially pumped and $\vec{b}+\vec{c}$ perpendicular to the transition dipole direction. The signals obtained with the polarization of the optical pulse parallel and perpendicular to the polarization of the x-ray pulse are:

$$\left.\begin{aligned}\Delta S_{\parallel} &= 0.6\,\Delta S_a + 0.2\,\Delta S_b + 0.2\,\Delta S_c \\ \Delta S_{\perp} &= 0.2\,\Delta S_a + 0.4\,\Delta S_b + 0.4\,\Delta S_c\end{aligned}\right\} \Rightarrow \begin{aligned}\Delta S_a &= 2\Delta S_{\parallel} - \Delta S_{\perp} \\ \Delta S_{b+c} &= 3\Delta S_{\perp} - \Delta S_{\parallel}\end{aligned}$$

The transition dipole moments of AdoCbl excited by 365 nm and 540 nm pulses are approximately orhtogonal. The cob(II alamin photoproduct is identical for both excitation wavelenghts. Thus 365 nm and 540 nm exciation wavelengths for a time delay of 250 ps allows the unique identification of the *x*, *y*, and *z* contributions to the XANES difference spectrum for bond homolysis forming cob(II)alamin from AdoCbl. The use of one excitation wavelength, 540 nm for AdoCbl at 450 ps or 520 nm for MeCbl at 100 ps, only allows identification of *x*, parallel to the transition moment, and the sum *y*+*z* of the perpendicular directison.

The isotropic difference spectrum $\left(\Delta S_{iso} = \Delta S_{\parallel} + 2\Delta S_{\perp}\right)$ obtained for a delay of 450 ps following excitation of AdoCbl is plotted in **Figure 4.2**. This plot also illustrates the laser off XANES spectrum of AdoCbl and the XANES spectrum of cob(II)alamin calculated from the 450 ps difference spectrum as $S_{cob(II)} = (S_{Off} + \alpha\Delta S_{iso})/\alpha$ where α is the fraction of cob(II)alamin in the sample. In this measurement, the initial fraction excited by the optical pulse was ≈0.23 and α at 450 ps is ≈0.13 when geminate recombination of the radical pair is taken into account. The cob(II)alamin XANES spectrum is consistent with spectra reported in the literature for the reduced species.[28]

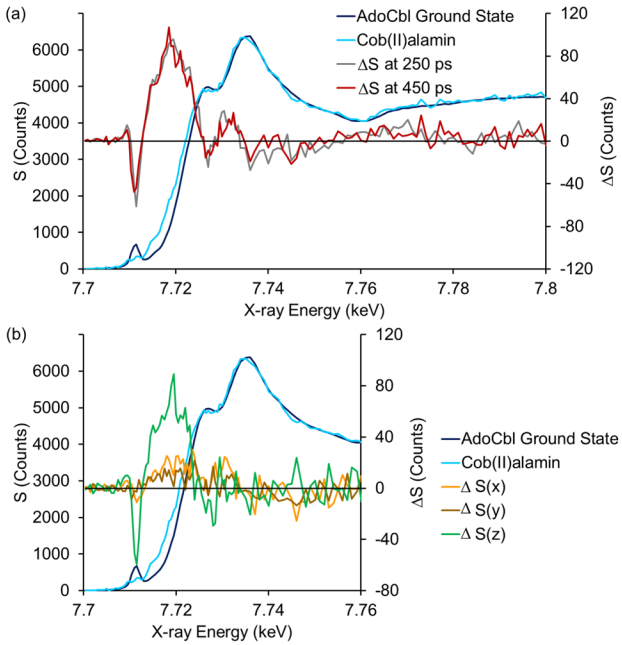

Figure 4.2 (A) The XANES spectrum of AdoCbl obtained from the optical laser-off measurement is compared with the scaled difference spectra at 250 ps and 450 ps time delay following excitation at 540 nm. The cob(II)alamin XANES spectrum derived from the 450 ps difference spectrum is shown for comparison. (B) The XANES difference spectrum at 250 ps decomposed into contributions in the *x*, *y*, and *z* directions.

As expected, the XANES difference spectrum measured at 250 ps is essentially the same as that measured at 450 ps, differing only by a small change in amplitude. Both difference spectra represent the changes that accompany formation of cob(II)alamin (**Figure 4.2 A**). This difference spectrum was measured using parallel and perpendicular polarization following excitation at both 540 nm and 365 nm. The isotropic difference spectrum 250 ps after excitation is independent of excitation wavelength as seen in **Figure 4.3**. This demonstrates that the same excited state is formed with both wavelengths.

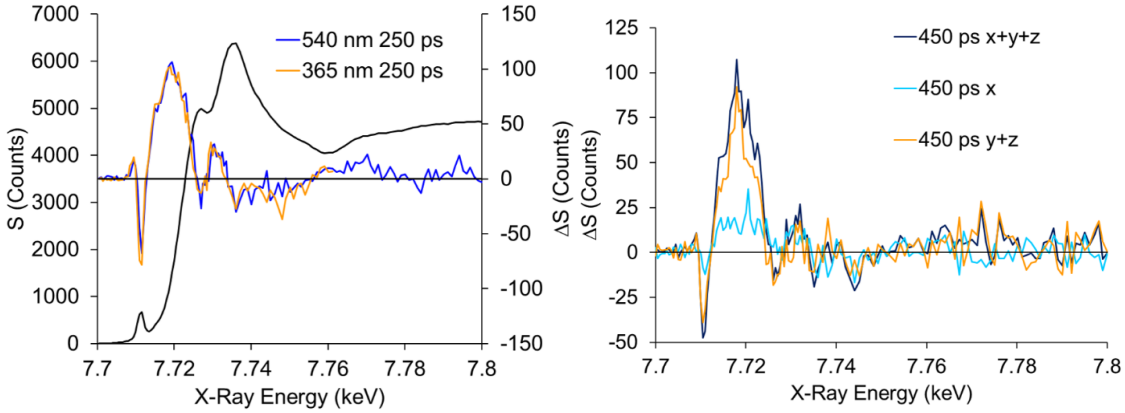

Figure 4.3 Left: Comparison of the isotropic XANES difference spectra obtained 250 ps after excitation of AdoCbl at 540 nm (blue) and 365 nm (yellow). The ground state XANES spectrum of AdoCbl is plotted in black for reference. Right: Decomposition of the XANES difference spectrum 450 ps after excitation of AdoCbl into x and y+z components.

The ππ* transition dipoles accessed at the two wavelengths are approximately orthogonal to each other in the corrin ring (**Figure 4.4 A**) and rotational diffusion of the cobalamin is minimal over the first 450 ps (**Figure 4.4 B**). Thus, the polarized difference spectra may be used to extract the contributions decomposed into the *x*, *y*, and *z* directions as described previously for CNCbl.[12] These difference spectra are plotted in **Figure 4.2 B**. Difference spectra in the *x* and *y*+*z* directions at 450 ps after excitation at 540 nm are plotted in **Figure 4.3**. The dominant contribution to the XANES difference spectrum corresponding to the formation of cob(II)alamin is an edge shift in the *z*-polarized component, consistent with the loss of the upper axial ligand and contraction of the Co-N_{DMB} bond. The equatorial contributions are quite small, consistent with the fact that there are only small changes is the Co-N_{eq} bonds observed in the cob(II)alamin crystal structure, averaging -0.3±0.1%.[29,30]

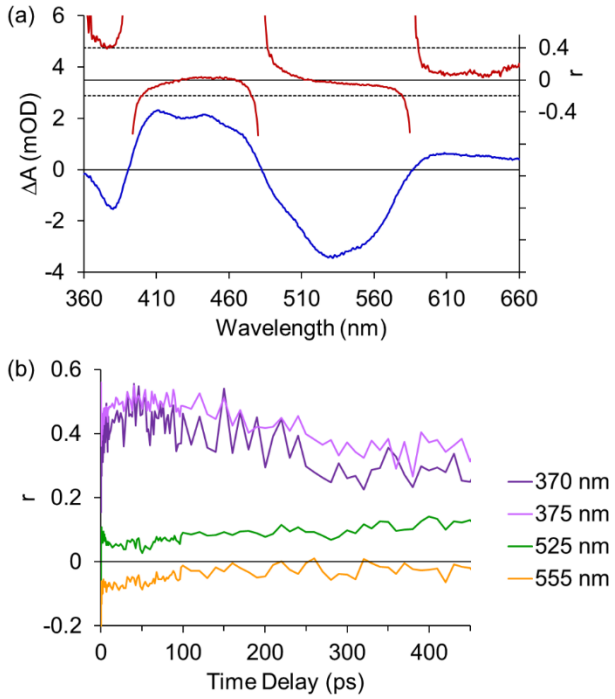

Figure 4.4 (A) Isotropic difference spectrum (blue, ΔA) and absorption anisotropy (red, r) 40 ps after excitation of AdoCbl at 340 nm. This plot demonstrates that the transition dipole moments at 365 nm and 540 nm are approximately orthogonal to each other. (B) Time dependent anisotropy changes at four wavelengths following excitation at 340 nm. The change in anisotropy over the first 200 ps reflect changes in the excited state followed by formation of cob(II)alamin. The anisotropy is approximately constant from 200 ps to 450 ps demonstrating that diffusive reorientation of the cobalamin molecule is small on this time scale. This means that the 250 ps and the 450 ps XANES transient reflect the initial anisotropic distribution of excited states.

In contrast to AdoCbl, excitation of MeCbl in the visible region of the spectrum results in formation of an excited state with a 1 ns lifetime in water at room temperature.[22,24] The XANES difference spectrum obtained 100 ps after excitation of MeCbl at 520 nm probes this excited state. The isotropic difference spectrum for formation of the excited state is plotted in the top panel of **Figure 4.6**. The ground state XANES spectrum of MeCbl, the spectrum of the cob(II)alamin that is formed following photolysis of AdoCbl, and the estimated spectrum of the excited state of MeCbl ($S_{ES} = (S_{Off} + \alpha\Delta S_{iso})/\alpha$, $\alpha \approx 0.25$) are plotted in the lower panel. The ground state XANES spectra of AdoCbl and MeCbl are similar (**Figure 4.5**), consistent with the fact that they have very similar corrin ring structures.

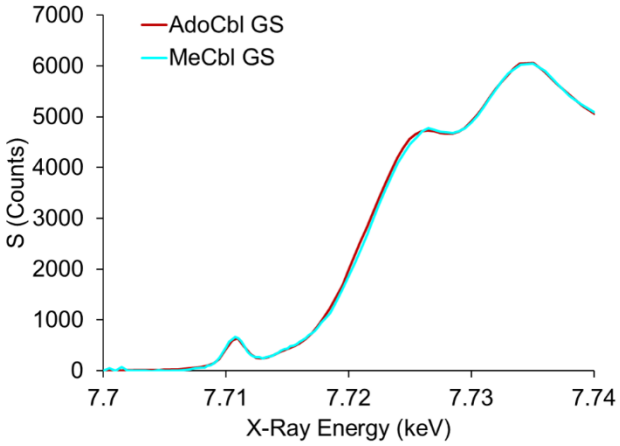

Figure 4.5 Comparison of the ground state XANES spectra of AdoCbl and MeCbl in a room temperature liquid jet using fs x-ray pulses. The MeCbl has been scaled to match the counts for AdoCbl as different detector arrangements were used for these two runs. Note that, in the absence of radiation damage, these two spectra are similar with only a slight blue-shift of the edge for MeCbl compared with AdoCbl.

From the MeCbl ground state spectrum and the AdoCbl photolysis difference spectrum, we can calculate the difference spectrum that should be observed following the photolysis of MeCbl to form cob(II)alamin (dashed line in **Figure 4.6**). The measured difference spectra for formation of the MeCbl excited state and for formation of cob(II)alamin are similar in magnitude. Thus, the assumption by Subramanian et al. that the 200 ps difference spectrum measured after excitation at 400 nm is dominated by the MeCbl excited state which accounts for 75% of the population is valid.

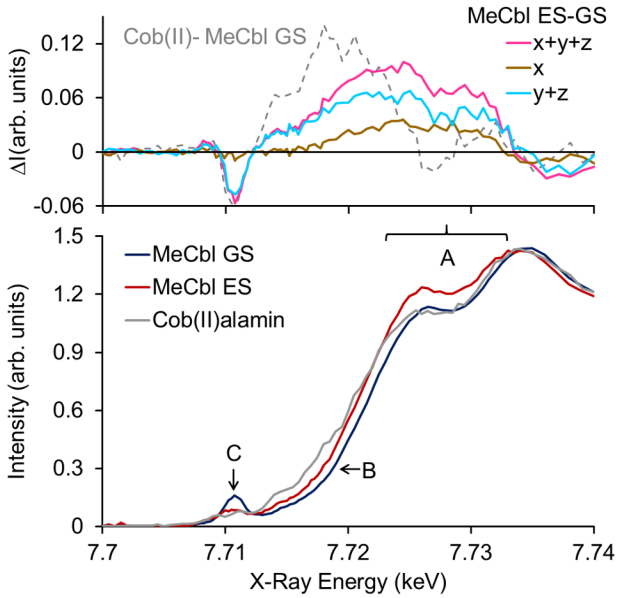

Figure 4.6 Top: The total isotropic difference spectrum 100 ps after excitation of MeCbl and the decomposition into *x* and *y+z* contributions. The difference spectrum for formation of cob(II)alamin is also plotted, calculated as the difference between cob(II)alamin determined from the photolysis of AdoCbl and the ground state MeCbl spectrum. Bottom: Comparison of the laser off XANES spectrum for the ground state of MeCbl with the cob(II)alamin XANES and the inferred excited state spectrum of MeCbl at 100 ps. The regions marked A, B, and C are discussed in the text.

The difference spectrum for the formation of cob(II)alamin is essentially identical to the microsecond difference spectrum following excitation at 400 nm reported by Subramanian et al (**Figure 4.7**).[14] Accordingly, we suggest that this photoproduct is not a novel microsecond-lifetime product corresponding to a recombination product with a lengthened Co-N_{DMB} bond (DMB = dimethylbenzimidazole), as suggested, but is instead the previously identified cob(II)alamin product that is known to form following 400 nm excitation (**Figure 4.7**). In this interpretation, the red-shift of the XANES edge arises from the loss of the upper axial ligand, but not the expansion of the Co-N_{DMB} bond. This is consistent with x-ray crystal structures and with theoretical simulations, both of which report *contraction* of the Co-N_{DMB} bond between AdoCbl or MeCbl and cob(II)alamin.[18,19,29–33]

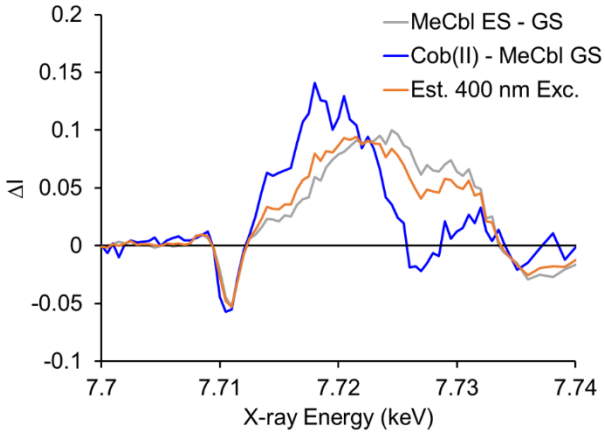

Figure 4.7 Comparison of the XANES difference spectra for the formation of the excited state (ES, gray) and cob(II)alamin (Cob(II)) from the ground state (GS) of MeCbl (blue). The difference spectrum for the formation of cob(II)alamin is the same as the spectrum reported by Subramanian et al. for microsecond delay. The estimated spectrum for 25% cob(II)alamin and 75% excited state (orange) is also shown for comparison.

The decomposition of the difference spectrum into contributions in the *x* and *y*+*z* directions are plotted with the isotropic difference spectrum in the top panel of **Figure 4.6**. The *x*-polarized component, along the optical transition dipole moment in the coring ring, makes a significant contribution to the XANES difference spectrum in the region between 7.72 and 7.733 keV reflected in the increase in x-ray absorption in the first peak of the XANES spectrum. The *x*-polarized contribution in region A in **Figure 4.6** is approximately half the intensity of the *y*+*z* contribution. The edge shift, indicated by arrow B in **Figure 4.6**, is dominated by changes in *y*+*z*, with a smaller *x*-polarized contribution. Finally, the bleach of the pre-edge transition, indicated by the arrow C, is polarized entirely in the *z* and/or *y* directions. Comparison with **Figure 4.2 B** and with the much weaker pre-edge bleach in cyanocobalamin[12] indicates that the bleach of the pre-edge transition is *z*-polarized, consistent with assignment to a cobalt centered $1s \rightarrow 3d_{z^2}/4p_z$ transition.

Qualitatively, these observations demonstrate that, in contrast with our findings for CNCbl, the structural changes that take place when the MeCbl excited state forms must be approximately uniformly distributed across *x*, *y*, and *z*. Indeed, if one makes the reasonable assumption that *x*- and *y*-polarized difference spectra

should be similar, it is apparent that the changes in *z* must be quite modest. The positive difference spectra reflect a small red-shift for each polarization suggesting a modest increase in the average bond-length along *x*, *y*, and *z*.

4.3.2 Comparison with Computational Methods

Recent TD-DFT calculations of the excited state structure in MeCbl provide a starting point for more detailed analysis of the XANES measurements. The FDMNES program was used to simulate the XANES spectrum for both the ground and excited states of the truncated structural model of the MeCbl molecule used in TD-DFT calculations.[34,35] We use the FDMNES method for simulations because it avoids the muffin tin approximation of FEFF and, in our hands, gives somewhat more accurate predictions of the cobalamin ground states, aside from a failure to reproduce the pre-edge, "1s-3d" region.[11,12] The ground state spectrum calculated for MeCbl is compared to the measured laser-off XANES spectrum in **Figure 4.8**. The simulated excited state spectrum exhibits an increase in intensity in region A, but no significant shift of the XANES edge. This result is not unexpected; the TD-DFT structure predicts a small *decrease* in the average axial (*z* direction) distances compared to the ground state with Co-C increasing by 0.02 Å from 1.986 Å to 2.006 Å, while Co-N_{DMB} decreases by 0.12 Å from 2.175 Å to 2.055 Å. A net decrease in the distance is expected to cause a blue shift to the *z*-polarized spectra, with a corresponding negative amplitude in the difference spectrum. The negative *z*-polarized signal (see **Figure 4.8**) partially cancels the positive amplitude predicted for *x* and *y*, giving a very small predicted differences XANES signal that is inconsistent with the experimental data. Thus, the XANES data suggest that the excited state that is formed following 520 nm excitation is not the optimized minimum energy structure identified in the TD-DFT simulations.

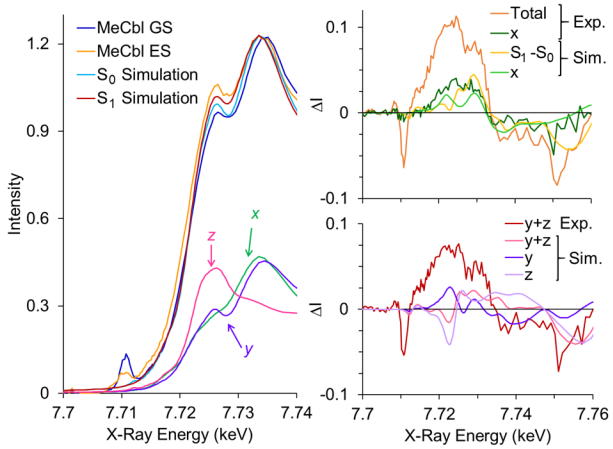

Figure 4.8 Left: Comparison of ground and excited state simulated spectra for MeCbl with the measured spectra. S_1 is the excited state structure identified in TD-DFT calculations. The axial bond lengths in S_0 are (Co-C, Co-N_{IM}) = (1.986 Å, 2.175 Å), in S_1 they are (2.006 Å, 2.055 Å). The Co-$N_{2(3)}$ bonds are expanded about 2% while the Co-$N_{1(4)}$ bonds are essentially unchanged. The decomposition of the simulated ground state spectrum into contributions polarized in the *x*, *y*, and *z* directions is also plotted. Top Right: Comparison of the measured (orange) and simulated (yellow) isotropic difference spectra and the *x*-polarized contributions (dark green experiment, light green simulation). Bottom Right: Comparison of the *y*+*z* component of the difference spectrum for simulation (pink) and experiment (red) along with the decomposition of the simulation into the *y* and *z*-polarized contributions.

The most obvious difference between the truncated model used in the excited state TD-DFT calculations and the MeCbl molecule is the presence of the full dimethylbenzimidazole base in the latter. Crystal structures comparing imidazole and dimethylbenzimidazole as the lower axial ligand demonstrate that the smaller imidazole ligand favors a shorter Co-N_{IM} bond (2.16 vs 2.09 Å).[36] The absence of the full DMB base, with its steric hindrance, may cause the TD-DFT calculations to overestimate the contraction of Co-N_{IM} bond that takes place in the excited state structure. To test this possibility, XANES simulations were performed for structures having longer Co-N_{IM} bonds, including the bond length of 2.175 Å that was calculated for the ground state. These simulations (**Figure 4.9**) capture the major features of the measured difference spectrum, however they underestimate the *y* contribution and appear to overestimate the *z* contribution to the difference spectrum, resulting in a cancellation of contributions in the predicted *y*+*z* component around 7.73 keV. In contrast, the experimental signal in *y*+*z* has a significant positive absorption change in this region (region A in **Figure 4.6**). Systematic changes in the upper axial bond length produce a similar discrepancy with the experimental date (**Figure 4.9**).

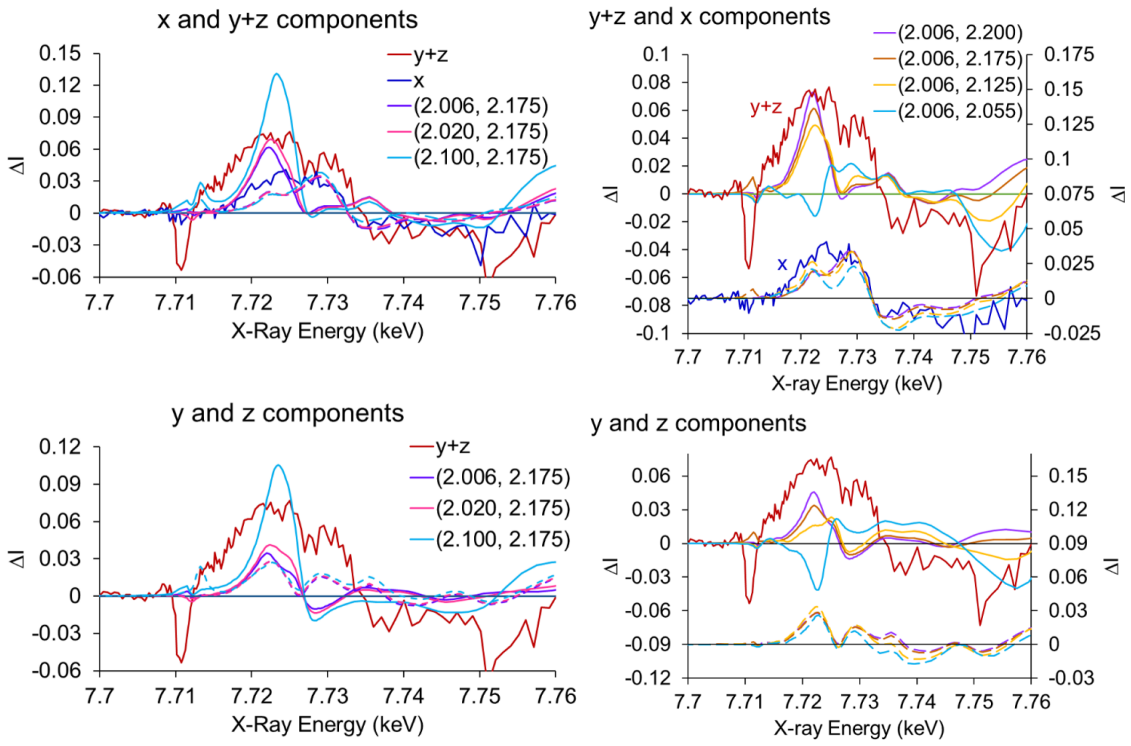

Figure 4.9 Top Left: Comparison of the *x* and *y+z* measurements with simulations performed for a range of Co-C bond lengths. The solid lines are *y+z* simulations, the dashed lines are the *x* simulations. Bottom Left: Decomposition of the y+z simulation into the y (dashed lines) and z (solid lines) contributions. Top Right: Comparison of the *x* and *y+z* measurements with simulations performed for a range of Co-N_{IM} bond lengths. Bottom Right: Decomposition of the y+z simulation into the y (dashed lines) and z (solid lines) contributions.

Although the FDMNES simulation using the TD-DFT calculated S_1 structure underestimates the total XANES difference spectrum, the simulation is qualitatively consistent with the *x*-polarized component of the spectrum. The TD-DFT calculations of the S_1 excited state predict an expansion of the ring consistent with π→π* excitation of the corrin ring (**Figure 4.10 A**). The measured difference spectra suggest that the changes to the corrin ring should be somewhat larger than calculated. To model to contribution of the *y+z* component around 7.73 keV we explored the influence of corrin ring expansion on the XANES difference spectrum.

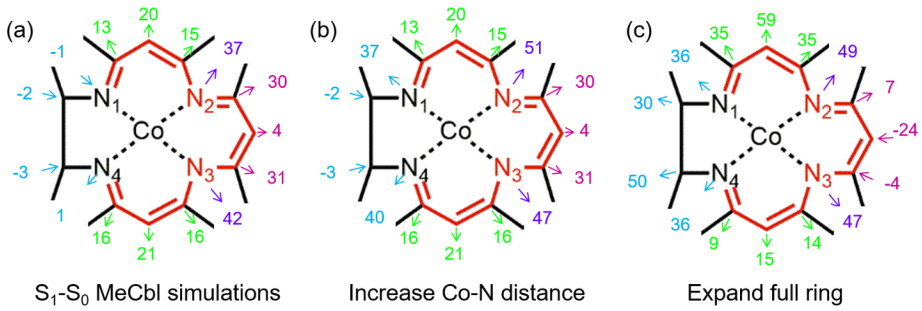

Figure 4.10 . Expansion of the ring distances to Co in units of mÅ (i.e. in S_1 nitrogen N_3 is 0.042 Å further from the Co than it is in S_0). (A) Expansion from S_0 to S_1 using the simulated ground and excited states. (B) An additional expansion of the Co-N_{eq} distances as indicated. (C) Expansion of the entire ring midway between rhodibalamin and S_1 cobalamin

One of the challenges in simulation *x*- and *y*-polarized XANES for corrins is that the corrin ring is quite flexible so that changes in Co-N_{eq} distances cause changes in the Co-C positions due to "ruffling" of the corrin ring. In addition to adjusting the Co-N_{eq} distances while leaving the remainder of the corrin fixed, we sought an experimentally validated model to use for predicting positions of all of the corrin atoms. Kräutler and colleagues have synthesized an adenosylrhodibalamin (AdoRbl) compound with the central Co replaced by the much larger Rh atom.[37] We took the crystal structure of this compound as an upper limit for physically reasonable expansion of the M-N_{eq} bonds in the excited electronic state and as a plausible prediction of the Co to C_{ring} distances. An expansion with the Co-N_{eq} bonds midway between the calculated cobalamin excited state and the rhodibalamin structure leaving the remainder of the ring in the calculated S_1 structure provides reasonable agreement with the measured difference spectra as illustrated in **Figure 4.11 A and B**. Better overall agreement between the measurements and simulation is found for expansion of the ring coupled with the Co-C bond at 2.006 Å as in the TD-DFT calculation accompanied by a somewhat longer Co-N_{IM} bond (**Figure 4.11 C**).

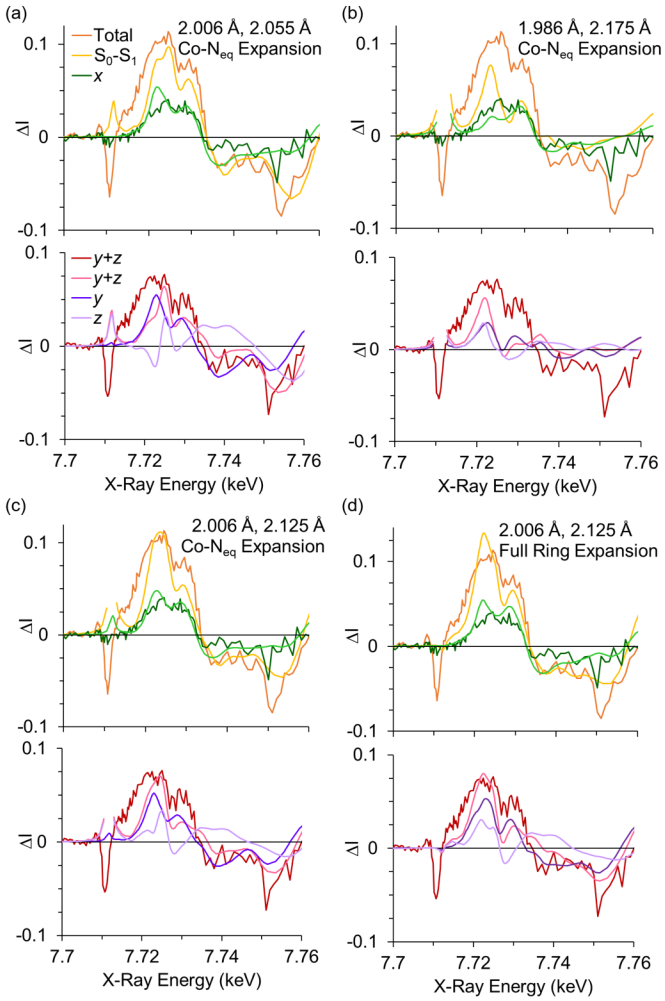

Figure 4.11 Comparison of experimental and simulated XANES difference spectra for an expanded corrin ring. The axial bond lengths are indicated as Co-C, Co-N_{IM}. (A) Co-N_{eq} bonds as in Figure 4.10 B midway between calculated MeCbl S_1 and the AdoRbl ring. The axial bonds are at the calculated S_1 distances. (B) Co-N_{eq} bonds as in Figure 4.10 B midway between calculated MeCbl S_1 and the AdoRbl ring. The axial bonds are at the calculated S_0 distances. (C) Co-N_{eq} bonds as in Figure 4.10 B midway between calculated MeCbl S_1 and the AdoRbl ring. The Co-C bond is at the calculated S_1 distance and the Co-N_{IM} bond is contracted to 2.125 Å from the ground state value of 2.175 Å. (D) Full corrin ring expansion as in Figure 4.10 C. The axial bonds are the same as in Figure 4.12 C.

Expansion of the entire corrin ring midway between the calculated cobalamin excited state and the rhodibalamin structure gives the simulated spectrum in **Figure 4.6 D**. The positive feature around 7.73 keV in the XANES difference spectrum arises from the expansion of the ring in the excited state. The absence of a significant difference spectrum between MeCbl or AdoCbl and cob(II)alamin in the region above 7.725 keV (see **Figure 4.2** and **Figure 4.6**) is consistent with a similarity of the corrin ring in these compounds. Simulations for other ring distortions are summarized in **Figure 4.12**.

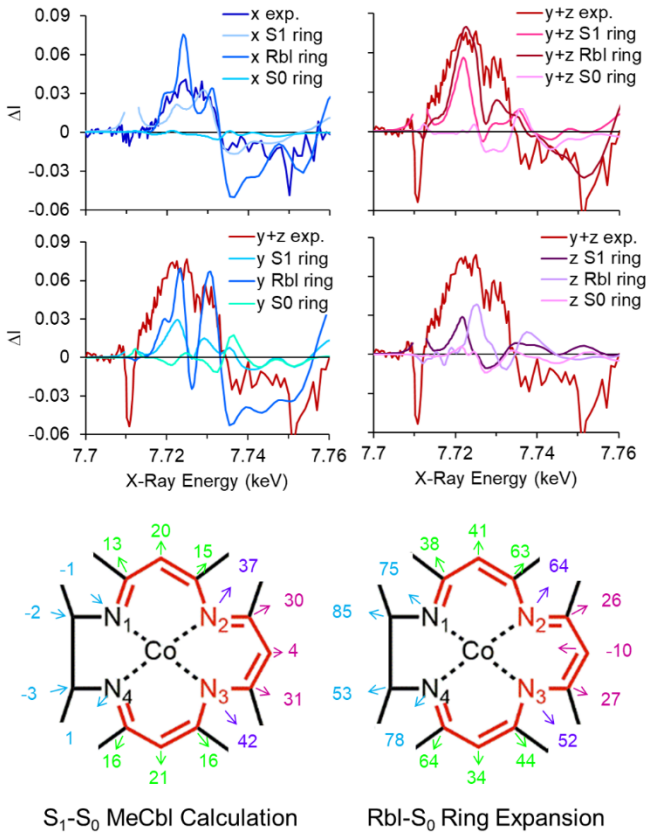

Figure 4.12 Comparison of the influence of the corrin ring (labeled S1 ring, RbI ring) and the N_{IM}-Co-C bond angle (labeled S0 ring) on the simulated XANES difference spectrum. The axial bonds are at the ground state distances.

Subramanian et al. reported a series of simulations of the XANES spectrum of MeCbl as a function of structural changes using the FEFF8.4 code.[14] These simulations highlight the separate influence of modification in the Co-N_{eq}, Co-N_{IM}, and Co-C bonds and allow a qualitative discussion of the structural changes. Our simulations performed using FDMNES are in qualitative agreement with their FEFF simulations. However, the quantitative comparison of the magnitude of the difference spectrum, the separation of *x* and *y+z* contributions, and the elimination of contributions arising from the formation of cob(II)alamin, permit a more precise analysis of the structural changes between the ground and excited state of MeCbl.

4.4 CONCLUSIONS

Excitation of AdoCbl at 540 nm or 365 nm results in the formation of cob(II)alamin. The XANES difference spectra are characterized by a large red-shift in the *z*-polarized component, consistent with loss of the upper axial ligand, but only small changes in the corrin ring. In contrast, the electronic excited state that is populated following 400 nm or 520 nm excitation of MeCbl results in a small elongation of the axial Co-C bond (ca. 1%) consistent with the TD-DFT calculations and with inferences from the excited state UV-visible spectrum. This axial change is accompanied by changes in the corrin ring larger than those predicted in the TD-DFT calculation of the excited state structure. The TD-DFT calculation suggests expansion of -0.1, 1.9, 2.2, and 0.1% for Co-N_{1-4} respectively. Somewhat larger expansions of 2, 2.4, 2.6, and 2.1%, midway between the bond lengths predicted for the excited state and measured for AdoRbl, provide better agreement with the measured XANES data. Finally, the TD-DFT calculations overestimate the contraction of the Co-N_{DMB} bond length in the excited state. The XANES measurements are inconsistent with the predicted 5.5% contraction of this bond. A contraction of around 2.3% is more consistent with the observed spectra. This discrepancy may be due to the influence of the full dimethylbenzimidazole group and the constraint of the linkage to the ring on the excited state structure.

The XANES measurements on the MeCbl excited state are consistent with our prior interpretation of the UV-visible spectrum as indicating small axial changes in the excited state structure. This is in contrast to the large axial expansion observed for CNCbl and the elongation of the lower axial bond predicted from the transient absorption spectra of AdoCbl[22,23] and two B_{12} antivitamins.[8,38,39] The simulations of XANES spectra presented here are not exhaustive and further refinement of the upper and lower axial bonds, as well as the expansion of the ring, may provide better agreement with the experimental data. However, the general trends are clear. A more detailed analysis of the excited state structure will require systematic simulations for a wide range of potential coordinates as

well as comparison with other cobalamin compounds. Such work is underway for a series of cobalamins including both MeCbl and AdoCbl. Time-resolved EXAFS measurements also provide the potential for quantitative analysis of the bond length changes around the central cobalt atom. These measurements will become feasible with the next generation of XFEL sources with higher repetition rates and easier tunability over the broad energy range required.

4.5 AUTHOR CONTRIBUTION

The author of this dissertation contributed the following to this work: wrote data analysis code for and performed analysis of all XFEL data presented in this chapter and performed and analyzed all FDMNES simulations presented in this chapter.

4.6 REFERENCES

1. Shell, T. A. & Lawrence, D. S. A new trick (hydroxyl radical generation) for an old vitamin (B 12). *J. Am. Chem. Soc.* **133**, 2148–2150 (2011).
2. Shell, T. A. & Lawrence, D. S. Vitamin B12: A Tunable, Long Wavelength, Light-Responsive Platform for Launching Therapeutic Agents. *Acc. Chem. Res.* **48**, 2866–2874 (2015).
3. Shell, T. A., Shell, J. R., Rodgers, Z. L. & Lawrence, D. S. Tunable Visible and Near IR Photoactivation of Light-Responsive Compounds. **53**, 875–878 (2015).
4. Chemaly, S. M. New light on Vitamin B12: The adenosylcobalamin-dependent photoreceptor protein CarH. *S. Afr. J. Sci.* **112**, 1–9 (2016).
5. Padmanabhan, S., Jost, M., Drennan, C. L. & Elías-Arnanz, M. A New Facet of Vitamin B 12 : Gene Regulation by Cobalamin-Based Photoreceptors . *Annu. Rev. Biochem.* **86**, 485–514 (2017).
6. Kutta, R. J. *et al.* The photochemical mechanism of a B 12-dependent photoreceptor protein. *Nat. Commun.* **6**, (2015).
7. Jost, M. *et al.* Structural basis for gene regulation by a B12-dependent photoreceptor. *Nature* **526**, 536–541 (2015).
8. Miller, N. A. *et al.* Toward the Design of Photoresponsive Conditional Antivitamins B12: A Transient Absorption Study of an Arylcobalamin and an Alkynylcobalamin. *J. Am. Chem. Soc.* **138**, 14250–14256 (2016).
9. Kräutler, B. Antivitamins B12 - A Structure- and Reactivity-Based Concept. *Chem. - A Eur. J.* **21**, 11280–11287 (2015).
10. Zerdane, S. *et al.* Probing Transient Photoinduced Charge Transfer in Prussian Blue Analogues with Time-Resolved XANES and Optical Spectroscopy. *Eur. J. Inorg. Chem.* **2018**, 272–277 (2018).
11. Miller, N. A. *et al.* Polarized XANES monitors femtosecond structural evolution of photoexcited Vitamin B12. *J. Am. Chem. Soc.* **139**, 1894–1899 (2017).
12. Miller, N. A. *et al.* Ultrafast X-ray Absorption Near Edge Structure Reveals Ballistic Excited State

Structural Dynamics. *J. Phys. Chem. A* **122**, 4963–4971 (2018).

13. Shelby, M. L. *et al.* Ultrafast Excited State Relaxation of a Metalloporphyrin Revealed by Femtosecond X-ray Absorption Spectroscopy. *J. Am. Chem. Soc.* **138**, 8752–8764 (2016).
14. Subramanian, G. *et al.* Direct Structural and Chemical Characterization of the Photolytic Intermediates of Methylcobalamin Using Time-Resolved X-ray Absorption Spectroscopy. *J. Phys. Chem. Lett.* **9**, 1542–1546 (2018).
15. Chen, L. X. *et al.* Imaging ultrafast excited state pathways in transition metal complexes by X-ray transient absorption and scattering using X-ray free electron laser source. *Faraday Discuss.* **194**, 639–658 (2016).
16. Levantino, M. *et al.* Observing heme doming in myoglobin with femtosecond X-ray absorption spectroscopy. *Struct. Dyn.* **2**, (2015).
17. Lemke, H. T. *et al.* Coherent structural trapping through wave packet dispersion during photoinduced spin state switching. *Nat. Commun.* **8**, (2017).
18. Kozlowski, P. M., Garabato, B. D., Lodowski, P. & Jaworska, M. Photolytic properties of cobalamins: A theoretical perspective. *Dalt. Trans.* **45**, 4457–4470 (2016).
19. Toda, M. J., Lodowski, P., Mamun, A. Al, Jaworska, M. & Kozlowski, P. M. Photolytic properties of the biologically active forms of vitamin B12. *Coord. Chem. Rev.* **385**, 20–43 (2019).
20. Lodowski, P., Jaworska, M., Andruniów, T., Garabato, B. D. & Kozlowski, P. M. Mechanism of Co-C bond photolysis in the base-on form of methylcobalamin. *J. Phys. Chem. A* **118**, 11718–11734 (2014).
21. Shiang, J. J. *et al.* Ultrafast Excited-State Dynamics in Vitamin B 12 and Related Cob (III) alamins. **1**, 801–808 (2006).
22. Shiang, J. J., Walker, L. A., Anderson, N. A., Cole, A. G. & Sension, R. J. Time-resolved spectroscopic studies of B12 coenzymes: The photolysis of methylcobalamin is wavelength dependent. *J. Phys. Chem. B* **103**, 10532–10539 (1999).
23. Harris, D. A., Stickrath, A. B., Carroll, E. C. & Sension, R. J. Influence of environment on the electronic structure of cob(III)alamins: Time-resolved absorption studies of the S1 state spectrum and dynamics. *J. Am. Chem. Soc.* **129**, 7578–7585 (2007).
24. Walker, L. A. *et al.* Time-resolved spectroscopic studies of B12 coenzymes: The identification of a metastable Cob(III)alamin photoproduct in the photolysis of methylcobalamin. *J. Am. Chem. Soc.* **120**, 3597–3603 (1998).
25. Chollet, M. *et al.* The X-ray Pump-Probe instrument at the Linac Coherent Light Source. *J. Synchrotron Radiat.* **22**, 503–507 (2015).
26. Stickrath, A. B. *et al.* Solvent-dependent cage dynamics of small nonpolar radicals: Lessons from the photodissociation and geminate recombination of alkylcobalamins. *J. Phys. Chem. A* **113**, 8513–8522 (2009).
27. Yoder, L. M., Cole, A. G., Walker, L. A. & Sension, R. J. Time-resolved spectroscopic studies of B12 coenzymes: Influence of solvent on the photolysis of adenosylcobalamin. *J. Phys. Chem. B* **105**, 12180–12188 (2001).
28. Champloy, F., Gruber, K., Jogl, G. & Kratky, C. XAS spectroscopy reveals X-ray-induced photoreduction of free and protein-bound B12 cofactors. *J. Synchrotron Radiat.* **7**, 267–273 (2000).
29. Kräutler, B., Keller, W. & Kratky, C. Coenzyme B12 Chemistry: The Crystal and Molecular Structure

of Cob(II)alamin. *J. Am. Chem. Soc.* **111**, 8936–8938 (1989).

30. Mebs, S., Henn, J., Dittrich, B., Paulmann, C. & Luger, P. Electron densities of three B12 vitamins. *J. Phys. Chem. A* **113**, 8366–8378 (2009).
31. Randaccio, L., Geremia, S., Nardin, G. & Wuerges, J. X-ray structural chemistry of cobalamins. *Coord. Chem. Rev.* **250**, 1332–1350 (2006).
32. Demissie, T. B., Repisky, M., Liu, H., Ruud, K. & Kozlowski, P. M. Cob(II)alamin: Relativistic DFT analysis of the EPR parameters. *J. Chem. Theory Comput.* **10**, 2125–2136 (2014).
33. Garabato, B. D., Lodowski, P., Jaworska, M. & Kozlowski, P. M. Mechanism of Co-C photodissociation in adenosylcobalamin. *Phys. Chem. Chem. Phys.* **18**, 19070–19082 (2016).
34. Bunău, O. & Joly, Y. Self-consistent aspects of x-ray absorption calculations. *J. Phys. Condens. Matter* **21**, (2009).
35. Joly, Y. X-ray absorption near-edge structure calculations beyond the muffin-tin approximation. *Phys. Rev. B - Condens. Matter Mater. Phys.* **63**, 1–10 (2001).
36. Fasching, M. *et al.* Coα-(1H-Imidazolyl)-Coβ-methylcob(III)amide: Model for protein-bound corrinoid cofactors. *Helv. Chim. Acta* (2000). doi:10.1002/1522-2675(20000906)83:9<2295::AID-HLCA2295>3.0.CO;2-T
37. Widner, F. J. *et al.* Total Synthesis, Structure, and Biological Activity of Adenosylrhodibalamin, the Non-Natural Rhodium Homologue of Coenzyme B12. *Angew. Chemie - Int. Ed.* **55**, 11281–11286 (2016).
38. Lodowski, P., Toda, M. J., Ciura, K., Jaworska, M. & Kozlowski, P. M. Photolytic Properties of Antivitamins B12. *Inorg. Chem.* **57**, 7838–7850 (2018).
39. Lodowski, P., Ciura, K., Toda, M. J., Jaworska, M. & Kozlowski, P. M. Photodissociation of ethylphenylcobalamin antivitamin B12. *Phys. Chem. Chem. Phys.* **19**, 30310–30315 (2017).

Chapter 5 Conclusions and Future Directions

5.1 KEY RESULTS

The work in this dissertation detailed how ultrafast spectroscopy can be used as a tool for deepening our understanding of the mechanisms that drive important chemical systems in chemistry and biochemistry. We were able to investigate how changes in the electronic structure of a molecule affect the dynamics, both through photo- or electrochemical induction of an excited state or reduced species and through synthesis of molecules chosen to exaggerate the effects of a change in charge distribution.

We find 2D-IR to be a powerful technique for examining how changes in the electronic structure of the CO_2 reduction catalyst $Re(bpy)(CO)_3Cl$ affect its solvation dynamics. Changes to the electron density of the molecule induced by the replacement of the chloride axial ligand with the more electron-withdrawing benzimidazole ligand showed no effective change to the spectral diffusion timescale across a series of aprotic polar solvents, in line with previously reported results that similarly found no change when changing electron-withdrawing or -donating nature of the equatorial diimine ligand.[1] In our 2D-SEC experiments, we see changes in the vibrational lifetime of the high frequency carbonyl mode of the singly reduced rhenium species, $Re(bpy)(CO)_3Cl^{\cdot}$. Ongoing work will compare the spectral diffusion timescale of the singly reduced species to both the ground state of the electrocatalyst and to its long-lived equilibrium excited state, giving us a window into the solvation dynamics of key intermediates in both the electrocatalytic and photocatalytic cycles of this versatile CO_2 reduction catalyst.[2]

Our ultrafast x-ray absorption spectroscopy measurements on methylcobalamin and the cob(II)alamin photoproduct that is formed following photoexcitation of coenzyme B_{12} demonstrated the capability of polarized ultrafast x-ray pump probe spectroscopy to give a window into the structural changes that occur following photoexcitation. Coupling these measurements with robust simulations of excited state structures using near-edge structure calculation software such as FDMNES or FEFF and transient absorption measurements further enriches the information that can be gathered from analysis of the polarized x-ray difference spectra, linking changes in the electronic configuration to structural dynamics.[3,4] Additional work performed in part by the author of this dissertation on cyanocobalamin, adenosylcobalamin, and antivitamin Coβ-2-(2,4-difluorophenyl)-ethynylcobalamin (F_2PhEtyCbl) further reveals the ability of this powerful technique to yield information on excited-state dynamics of compounds in this class, particularly when combined with transient absorption UV-Vis measurements.[5–7] The ultrafast x-ray measurements on the F_2PhEtyCbl used a drop-on-demand sample delivery system synchronized to the LCLS XFEL, exposing only 45 µL of sample. This sample delivery method opens up the possibility for X-ray absorption measurements on precious photoactive samples, which would not have been easily or inexpensively integrated into more traditional sample delivery methods.

5.1 FUTURE DIRECTIONS

The 2DIR compatible OTTLE cell opens up many possibilities for analysis of electrocatalytic or electrochemical systems using 2DIR spectroscopy, expanding well beyond just the Lehn Re(bpy)$(CO)_3$Cl catalyst studied in this dissertation to any electrochemical system with a suitable vibrational probe. One of the main goals going forward is discerning the best method to extract dynamical information from the 2DIR set-up. A major challenge of performing spectroelectrochemical experiments on an ultrafast timescale is determining a way to either hold the system at equilibrium or to monitor the relative concentrations of different species throughout the course of an experiment, to isolate changes in rephasing/non-rephasing amplitudes due to dynamic

processes from the longer timescale build-up disappearance of species occurring as a result of the electrolysis. This is of particular concern in the case of the ReCl, where the singly reduced anionic species will couple to form the dimer after just a few minutes, complicating its analysis. Current and future work in the lab involves implementing a set-up where an absorption spectrum is recorded ahead of each 2DIR spectrum, so changes in concentration of each present species throughout the course of the experiment could be monitored and corrected for. Successful adoption of this method into the experimental design will allow for easier extraction of dynamical information such as spectral diffusion timescales, something that has yet to be determined from 2DIR-SEC experiments involving multiple species.

There is still a great deal of opportunity for future work on the ReCl system using this method. With successful addition of CO_2 to the solution, the rhenium catalyst could be monitored using 2DIR-SEC while the actual CO_2 to CO catalysis is occurring, giving unprecedented detail into this mechanism. The IR OTTLE cell described in this dissertation is easily adapted into a flowing system, which would be necessary for such an experiment. This would allow for clear identification of intermediate species that form throughout this electrocatalytic cycle. The mechanism of this electrocatalysis of CO_2 to CO by the $Re(bpy)(CO)_3Cl$ catalyst is reported to change based on solvent and presence of co-solvents or proton sources.[8–12] 2DIR-SEC experiments could further reveal the role that these species play in the mechanism, particularly the solvent or co-solvent, given the sensitivity of the CO probes on the ReCl species to solvation environment and phenomena such as preferential solvation.[1,2,13]

The 2DIR-SEC experimental design presented in this dissertation utilizes an OTTLE cell design that allows these experiments to be performed in a transmission geometry, while still avoiding issues of scatter due to the presence of the electrodes. This adds a new option for 2DIR-SEC experimental cell design that more closely resembles established spectroelectrochemical designs. The

development of this method, along with the other two cell designs by Hamm and Bredenbeck, opens up an exciting new field combining 2DIR and spectroelectrochemistry. Here, we focus on the rhenium system, however this technique could be used to study a host of interesting electrochemical systems with suitable vibrational probes. Many transition metal carbonyl complexes and clusters have been studied for their abilities to catalyze important reactions through electrochemical methods, and would make excellent candidates for electrocatalytic systems that could be further explored using this technique.[14,15,24,16–23] One such example is manganese carbonyl complexes that reduce CO_2 to CO through a mechanism similar to that of the ReCl molecule studied in this dissertation. Future work could focus on determining how the role of solvents and co-solvents differs between the mechanisms for the two molecules.

The successful implementation of the phase wobbler into our current 2DIR set-up not only aids with the spectroelectrochemical methods, but also opens up the possibility of studying samples that were previously inaccessible with 2DIR due to a propensity to scatter. Samples with low solubility or a tendency to aggregate could now feasibly be studied using our 2DIR set-up. One such example of this includes the labelled peptide system discussed in this dissertation, which has a low solubility and tendency to scatter. Experiments going forward on the small seven amino-acid peptide introduced in this dissertation and the full labelled trimer system will undoubtedly use this phase wobble set-up to eliminate scattering effects from the sample. To further incorporate this technique into our 2DIR experimental set-up, a second phase wobbler identical to the first could be placed in the path of the second pump beam, allowing for this elimination of scatter in both our rephasing and non-rephasing spectra.

Future work on the cobalamin systems could include soft X-ray absorption to probe the cobalt L-edge. L-edge absorption measurements offer better resolution, giving further insight into the Co electronic structure, and gives access

to transitions that are inaccessible with K-edge measurements. These measurements can provide greater detail on the covalency of the cobalt after photoexcitation, complementing the electronic structure information discovered using the Co K-edge absorption measurements.[25,26] Additionally, transient L-edge XAS measurements could be performed on the Re(bpy)(CO)3X catalyst, giving further insight into the structural evolution of this molecule following photoexcitation.

5.2 REFERENCES

1. Kiefer, L. M. & Kubarych, K. J. Solvent-dependent dynamics of a series of rhenium photoactivated catalysts measured with Ultrafast 2DIR. *J. Phys. Chem. A* **119**, 959–965 (2015).
2. Kiefer, L. M., King, J. T. & Kubarych, K. J. Equilibrium excited state dynamics of a photoactivated catalyst measured with ultrafast transient 2DIR. *J. Phys. Chem. A* **118**, 9853–9860 (2014).
3. Joly, Y. X-ray absorption near-edge structure calculations beyond the muffin-tin approximation. *Phys. Rev. B - Condens. Matter Mater. Phys.* **63**, 1–10 (2001).
4. Ankudinov, A. & Ravel, B. Real-space multiple-scattering calculation and interpretation of x-ray-absorption near-edge structure. *Phys. Rev. B - Condens. Matter Mater. Phys.* (1998). doi:10.1103/PhysRevB.58.7565
5. Miller, N. A. *et al.* Ultrafast XANES Monitors Femtosecond Sequential Structural Evolution in Photoexcited Coenzyme B12. *J. Phys. Chem. B* (2019). doi:10.1021/acs.jpcb.9b09286
6. Miller, N. A. *et al.* Ultrafast X-ray Absorption Near Edge Structure Reveals Ballistic Excited State Structural Dynamics. *J. Phys. Chem. A* **122**, 4963–4971 (2018).
7. Miller, N. A. *et al.* Antivitamins B12 in a Microdrop: The Excited-State Structure of a Precious Sample Using Transient Polarized X-ray Absorption Near-Edge Structure. *J. Phys. Chem. Lett.* (2019). doi:10.1021/acs.jpclett.9b02202
8. Stor, G. J., Hartl, F., Van Outersterp, J. W. M. & Stufkens, D. J. Spectroelectrochemical (IR, UV/Vis) Determination of the Reduction Pathways for a Series of [Re(CO)3(α-diimine)L']0/+ (L' = Halide, Otf-THF, MeCN, n-PrCN, PPh3, P(OMe)3) Complexes. *Organometallics* **14**, 1115–1131 (1995).
9. Johnson, F. P. A., George, M. W., Hartl, F. & Turner, J. J. Electrocatalytic reduction of CO2using the complexes [Re(bpy)(CO)3L]n(n = +1, L = P(OEt)3, CH3CN; n = 0, L = Cl-, Otf-; bpy = 2,2′-bipyridine; Otf-= CF3SO3) as catalyst precursors: Infrared spectroelectrochemical investigation. *Organometallics* **15**, 3374–3387 (1996).
10. Smieja, J. M. & Kubiak, C. P. Re(bipy-tBu)(CO)3Cl-improved catalytic activity for reduction of carbon dioxide: IR-spectroelectrochemical and mechanistic studies. *Inorg. Chem.* **49**, 9283–9289 (2010).
11. Riplinger, C., Sampson, M. D., Ritzmann, A. M., Kubiak, C. P. & Carter, E. A. Mechanistic contrasts between manganese and rhenium bipyridine electrocatalysts for the reduction of carbon dioxide. *J. Am. Chem. Soc.* **136**, 16285–16298 (2014).
12. Machan, C. W., Sampson, M. D., Chabolla, S. A., Dang, T. & Kubiak, C. P. Developing a mechanistic understanding of molecular electrocatalysts for CO2 reduction using infrared

spectroelectrochemistry. *Organometallics* **33**, 4550–4559 (2014).

13. Kiefer, L. M. & Kubarych, K. J. Solvent exchange in preformed photocatalyst-donor precursor complexes determines efficiency. *Chem. Sci.* **9**, 1527–1533 (2018).
14. Bertini, F. *et al.* Carbon Dioxide Reduction to Methanol Catalyzed by Mn(I) PNP Pincer Complexes under Mild Reaction Conditions. *ACS Catal.* (2019). doi:10.1021/acscatal.8b04106
15. MacHan, C. W. & Kubiak, C. P. Electrocatalytic reduction of carbon dioxide with Mn(terpyridine) carbonyl complexes. *Dalt. Trans.* (2016). doi:10.1039/c6dt03243e
16. Riplinger, C. & Carter, E. A. Influence of weak Bronsted acids on electrocatalytic CO2 reduction by manganese and rhenium bipyridine catalysts. *ACS Catal.* (2015). doi:10.1021/cs501687n
17. Riplinger, C., Sampson, M. D., Ritzmann, A. M., Kubiak, C. P. & Carter, E. A. Mechanistic contrasts between manganese and rhenium bipyridine electrocatalysts for the reduction of carbon dioxide. *J. Am. Chem. Soc.* (2014). doi:10.1021/ja508192y
18. McKinnon, M. *et al.* An Investigation of Electrocatalytic CO2 Reduction Using a Manganese Tricarbonyl Biquinoline Complex. *Front. Chem.* (2019). doi:10.3389/fchem.2019.00628
19. Grice, K. A. & Kubiak, C. P. Recent Studies of Rhenium and Manganese Bipyridine Carbonyl Catalysts for the Electrochemical Reduction of CO2. in *Advances in Inorganic Chemistry* (2014). doi:10.1016/B978-0-12-420221-4.00005-6
20. Stanbury, M., Compain, J. D. & Chardon-Noblat, S. Electro and photoreduction of CO2 driven by manganese-carbonyl molecular catalysts. *Coordination Chemistry Reviews* (2018). doi:10.1016/j.ccr.2018.01.014
21. Taheri, A., Thompson, E. J., Fettinger, J. C. & Berben, L. A. An Iron Electrocatalyst for Selective Reduction of CO2 to Formate in Water: Including Thermochemical Insights. *ACS Catal.* (2015). doi:10.1021/acscatal.5b01708
22. Loewen, N. D., Neelakantan, T. V. & Berben, L. A. Renewable Formate from C-H Bond Formation with CO2: Using Iron Carbonyl Clusters as Electrocatalysts. *Acc. Chem. Res.* (2017). doi:10.1021/acs.accounts.7b00302
23. Serra, D., Correia, M. C. & McElwee-White, L. Iron and ruthenium heterobimetallic carbonyl complexes as electrocatalysts for alcohol oxidation: Electrochemical and mechanistic studies. *Organometallics* (2011). doi:10.1021/om101070z
24. Taheri, A. & Berben, L. A. Tailoring Electrocatalysts for Selective CO2 or H+ Reduction: Iron Carbonyl Clusters as a Case Study. *Inorganic Chemistry* (2016). doi:10.1021/acs.inorgchem.5b02293
25. Baker, M. L. *et al.* K- and L-edge X-ray absorption spectroscopy (XAS) and resonant inelastic X-ray scattering (RIXS) determination of differential orbital covalency (DOC) of transition metal sites. *Coordination Chemistry Reviews* (2017). doi:10.1016/j.ccr.2017.02.004
26. Wasinger, E. C., De Groot, F. M. F., Hedman, B., Hodgson, K. O. & Solomon, E. I. L-edge X-ray Absorption Spectroscopy of Non-Heme Iron Sites: Experimental Determination of Differential Orbital Covalency. *J. Am. Chem. Soc.* (2003). doi:10.1021/ja034634s